MAGNETIZATION DYNAMICS IN THIN FILM AND MULTILAYER STRUCTURES

A THESIS
SUBMITTED TO THE FACULTY OF THE GRADUATE SCHOOL
OF THE UNIVERSITY OF MINNESOTA
BY

William Kenneth Peria

IN PARTIAL FULFILLMENT OF THE REQUIREMENTS
FOR THE DEGREE OF
DOCTOR OF PHILOSOPHY

PAUL A. CROWELL

June, 2022

Acknowledgements

I am grateful to many different individuals who have supported me throughout my time in graduate school and I will do my best to acknowledge them here. When I joined the Crowell group in May of 2017, I was very lucky that there were several senior graduate students always willing to provide their wisdom and share their experiences: Tim Peterson, Gordon Stecklein, and Justin Watts. Tim and I worked closely during this time on building the ferromagnetic resonance setup that produced many of the results presented in this thesis. The things I learned in the lab that first summer provided a solid foundation for the rest of my graduate research career.

The first year of graduate school—filled with classes, teaching, and preparing for the written exam—can be especially hectic and difficult to navigate, and I am grateful for the camaraderie of my fellow classmates that allowed us to get through it together.

Along the way, I worked with many other students in the Crowell group: Aaron Breidenbach, Joe Dill, James Etheridge, Alex Hamill, Zhen Jiang, Tao Qu, Juan Tigre-Lazo, and Han Yu. I enjoyed getting to know them, working with them, and learning from them. I also spent a lot of time during my first two years working in Xiaojia Wang's group in the Mechanical Engineering department. I gained a lot of valuable knowledge about the experimental techniques used in their lab which helped me better understand my field as a whole. I would also like to acknowledge the great collaboration opportunities that resulted from being supported by the SMART Center, which exists thanks to the efforts of Jian-Ping Wang and the other SMART Center PI's and staff.

My advisor Paul Crowell worked tirelessly to provide me with everything I needed to succeed. The knowledge and wisdom I have gained from his unselfish mentoring are the most valuable things I took from graduate school and it will serve me for many years to come. It is especially noteworthy that he was, and still is, simultaneously responsible

as Head for steering the department through the nightmarish circumstances created by the COVID-19 pandemic.

My family was very supportive and instrumental to my success in graduate school. My parents always encouraged my decision to pursue this career path and provided all the support I needed. I could not have done this without them. I am also grateful to have benefited from the experiences shared by my grandfather and uncle—both career physicists—which helped to demystify the process of getting a Ph.D. in physics.

My personal and intellectual growth during graduate school was far greater than I could have hoped for, and I thank all of these people for being a part of it.

Abstract

Spintronics is a field of research that seeks to exploit the spin rather than the charge of the electron for information-technology applications, with the promise of computational devices that use less energy while being faster and more powerful. A major challenge in this field has been the understanding and control of how the energy contained in a system of electron spins is transferred, and ultimately lost, to the rest of the material. This thesis presents experimental measurements of magnetization damping using ferromagnetic resonance in a variety of different thin films and multilayer structures, along with unique ways of understanding the physical mechanisms that cause damping.

First, the effect of an extrinsic two-magnon scattering mechanism on the magnetization damping is demonstrated in a series of Heusler alloy thin films. A model of two-magnon scattering is developed to fit the data, and particular emphasis is placed on the mechanisms which cause the effect to be stronger in the Heusler films. It is then shown how two-magnon scattering can shift the resonance frequency, an effect that is almost always neglected, which is important due to the ubiquity of using ferromagnetic resonance measurements to extract magnetic anisotropy energies. The following portion of the thesis deals primarily with magnon-phonon coupling and its effect on damping. A mechanism of magnetization damping due to magnon-phonon coupling is shown to dominate the overall damping in a series of $Fe_{0.7}Ga_{0.3}$ alloy thin films. The mechanism causes a giant anisotropy of the damping, with the damping coefficient varying by as much as a factor of 10 depending on the orientation of the magnetization. This mechanism is extrinsic, and so it is important to account for when measuring the intrinsic damping of a material. Finally, a phonon pumping mechanism is demonstrated in a series of Co/Pd multilayers. Phonon pumping causes a resonant damping of the magnetization dynamics, at a frequency that is determined by the total thickness of the multilayer. The temperature dependence is much stronger than expected, which underscores the importance of magnetic boundary conditions in the problem. There is also a resonance frequency shift that accompanies the resonant damping, which can be predicted accurately using linear response theory.

Contents

List of Tables

List of Figures

Chapter 1

Introduction

This thesis will present experimental results of magnetization damping in a variety of magnetic thin film and multilayer structures. The physical mechanisms that give rise to the damping will be elucidated primarily through the frequency, temperature, and orientation dependence of the magnetic relaxation rate as measured using ferromagnetic resonance (FMR).

In this chapter we will discuss the foundations of magnetization dynamics as well as a particularly well-known intrinsic damping mechanism that is present in metals and arises from spin-orbit coupling. In Chapter 2, the effect of two-magnon scattering—a well-known *extrinsic* damping mechanism—is observed in a series of Heusler alloy thin films. The focus is on the interplay between the low intrinsic damping of these films and the extrinsic two-magnon scattering. Chapter 3 demonstrates how the two-magnon process can affect the frequency of the dynamics in a way that is complementary to the way it affects the damping. In Chapter 4 we will shift our focus to the effect of magnon-phonon coupling on the damping in a series of films with strong such coupling. Chapter 5 will discuss an alternative means by which magnon-phonon coupling can cause damping—"phonon pumping"—in a more complex multilayer structure.

1.1 Spintronics and the Role of Magnetization Damping

Spintronics is a field of research which has grown vastly in the past few decades. The term "spintronics" is commonly used to refer to any research that seeks to manipulate

electron spin and exploit it as a carrier of information. The giant magnetoresistance effect (GMR) [5], which refers to an electrical resistance determined by the relative alignment of the magnetizations of two magnetic layers separated by a nonmagnetic spacer, has been of enormous utility in the magnetic storage industry [6]. The spin Hall effect, predicted by D'yakonov and Perel' [7] and observed by Kato *et al.* [8], is the primary means through which spin currents are generated and (through the inverse spin Hall effect) detected. Although exploited endlessly in the laboratory setting, the (inverse) spin Hall effect has yet to play a major role in technological applications.

The implementation of certain spintronic applications (such as spin-torque magnetic random access memory [9] and devices that use spin waves to perform computations [10–12]) has been particularly hindered by the presence of magnetization damping. This is largely due to the fact that scalable applications, especially those which are based on the switching of magnetization by electrical current, are dependent on high efficiency [13]. In this sense, magnetization damping plays a role in spintronics which is similar to that played by electron mobility in CMOS technology.

1.2 Heusler Alloys: Promising Materials for Spintronics

Heusler alloys, a class of intermetallics named for their discoverer Friedrich Heusler, have attracted a substantial amount of attention from the spintronics community in recent years. While many of them exhibit fascinating physical properties such as superconductivity and Weyl semimetallicity [14], they have garnered interest in spintronics primarily for the reason that some of them are half metallic, or nearly half metalllic. Half metallicity, the property of having completely spin-polarized electronic states at the Fermi level, was first predicted to exist in Mn-based Heusler alloys by de Groot *et al.* [15] through first-principles calculations. This property allows one, for instance, to achieve high spin injection efficiency [16]. In the full Heusler compounds, the gap between spin bands is known to arise from hybridization of $3d$ orbitals between constituent transition metal atoms [17]. In terms of magnetization damping, this leads to the suppression of spin-flip scattering (see Sec. 1.3.5). For this reason, Heusler alloys are predicted to have very low damping [18]. Only Chapter 2 of this thesis is concerned with Heusler alloys, but the search for ultralow damping in Heuslers motivates much of

the work that follows: the identification of "alternative" damping mechanisms. In this chapter we will introduce perhaps the most common theory of magnetization damping and experimental measurements of low damping in Heusler alloys.

1.3 Theory of Ferromagnetic Resonance and Magnetization Damping

Larmor precession is a well-known phenomenon which describes the rate of spin precession for a free electron in the presence of a magnetic field H:

$$\omega_L = \gamma H \tag{1.1}$$

where ω_L is the Larmor frequency and γ is the gyromagnetic ratio of a free electron. The Larmor frequency ω_L can be understood as the frequency of precession that a magnetic dipole experiences when it is displaced from its equilibrium orientation (parallel to H). Ferromagnetic resonance (FMR) is a very similar phenomenon to this, with the primary difference being that it occurs in a ferromagnetic material, where "effective" magnetic fields such as the demagnetizing field and magnetocrystalline anisotropy fields need to be taken into account. FMR was first observed by Griffiths [19] and explained shortly thereafter by Kittel [20 21]. From here we proceed to calculate the FMR frequency, the analog of Eq. 1.1 for a ferromagnet [22].

1.3.1 Derivation of the FMR Frequency

We start by introducing the Landau-Lifshitz equation, the basis for most calculations of magnetization dynamics:

$$\frac{d\mathbf{M}}{dt} = \gamma \mathbf{M} \times \mathbf{H}_{eff} \ , \tag{1.2}$$

where we neglect (for the moment) any terms needed to describe magnetization damping. Formally, the effective field is defined as $\mathbf{H}_{eff} = -\nabla_{\mathbf{M}} F$, where F is the magnetic free energy per unit volume of the system. Here, we will consider the effective field $\mathbf{H}_{eff}$ to be the sum of an applied field, demagnetizing field, magnetocrystalline anisotropy field, and an oscillating field perpendicular to the applied field:

$$\mathbf{H}_{eff} = \mathbf{H}_0 - \mathbf{D} \cdot \mathbf{M} + \mathbf{H}_K + \mathbf{h}(t) \tag{1.3}$$

where $\mathbf{D}$ is the demagnetization tensor which is determined by the geometry of the system. We will confine our attention to a thin film with the applied field in the plane of the film ($\mathbf{H}_0 \,||\, \hat{\mathbf{x}}$) and the magnetization saturated along the direction of the applied field, so that the demagnetization tensor is given by $D_{xx} = D_{yy} = 0$ and $D_{zz} = 4\pi$ (along with all off-diagonal elements being zero). Note that we have defined our coordinate system such that $\hat{\mathbf{z}}$ is normal to the plane of the film. Eq. 1.2 then takes the form

$$\frac{d\mathbf{m}}{dt} = \gamma[\mathbf{M}_s \times (-4\pi m_z \hat{\mathbf{z}} + \mathbf{H}_K + \mathbf{h}) + \mathbf{m}(t) \times (\mathbf{H}_0 + \mathbf{H}_K)] \ , \tag{1.4}$$

where we have introduced the notation $\mathbf{M}(t) = \mathbf{M}_s + \mathbf{m}(t)$. We will also suppose that we have an in-plane uniaxial magnetocrystalline anisotropy energy of the form $K_u \sin^2 \phi$, which gives $\mathbf{H}_K = -2K_u m_y / M_s^2 \hat{\mathbf{y}}$. We then assume that we are in a regime of linear response so that $\mathbf{m}(t) \sim e^{i\omega t}$, where ω is the frequency of the oscillating field $\mathbf{h}(t)$. From this, keeping terms to first order in $\mathbf{m}$, we obtain the following system of equations

$$\begin{aligned} m_x &= 0 \ ; \\ \frac{i\omega}{\gamma} m_y &= -M_s h_z + m_z (H_0 + 4\pi M_s) \ ; \\ \frac{i\omega}{\gamma} m_z &= M_s h_y - m_y \left(H_0 + \frac{2K_u}{M_s} \right) \ , \end{aligned} \tag{1.5}$$

which has a nontrivial solution for $\mathbf{h} = 0$ when

$$\omega = \gamma \sqrt{\left(H_0 + \frac{2K_u}{M_s} \right) (H_0 + 4\pi M_s)} \ . \tag{1.6}$$

Eq. 1.6 is known as the Kittel formula. A similar calculation with the field applied out of plane gives

$$\omega = \gamma (H_0 - 4\pi M_s) \ . \tag{1.7}$$

Eq. 1.6 and Eq. 1.7 are valuable experimentally as they allow one to obtain both the saturation magnetization and the magnetocrystalline anisotropy of the film under test. In practice it is common to have a uniaxial anisotropy due to the broken symmetry at the interfaces of the magnetic film, so that the saturation field $4\pi M_s$ is replaced by $4\pi M_{eff} = 4\pi M_s - K_\perp / 2M_s$ where $K_\perp$ is the interface anisotropy constant. It is also worth mentioning that the resonance condition can be obtained using a Lagrangian formalism originally due to Smit and Beljers [23] and Suhl [24]. The result is given by

$$\omega = \frac{\gamma}{M_s \sin\theta} \sqrt{F_{\theta\theta} F_{\phi\phi} - (F_{\theta\phi})^2} \tag{1.8}$$

where ϕ and θ are the azimuthal and polar angles of the magnetization, respectively, and $F_{\theta\theta}$, $F_{\phi\phi}$, and $F_{\theta\phi}$ are the second angular derivatives of the magnetic free energy. This formalism is particularly useful for situations when the magnetization and/or magnetic field are not aligned with high-symmetry directions.

1.3.2 Magnetoelastic Coupling

A major portion of this thesis is dedicated to studying the effects of magnetoelastic coupling (we will use this term interchangeably with magnon-phonon coupling) on magnetization dynamics, particularly with respect to damping. Here we introduce the most basic concepts of magnetoelastic coupling.

First consider the leading-order magnetoelastic coupling terms in the magnetic free energy density (applicable to cubic symmetry):

$$F_{me} = B_1 m_i m_j u_{ij} \delta_{ij} + B_2 m_i m_j u_{ij} (1 - \delta_{ij}) \ , \tag{1.9}$$

where B_1 and B_2 represent the coupling of the magnetization to normal and shear strain, respectively, $m_i \equiv M_i/M_s$ is the reduced magnetization, $u_{ij} \equiv 1/2(\partial u_i/\partial x_j + \partial u_j/\partial x_i)$ is strain, u_i is the displacement from equilibrium along the x_i coordinate, and δ_{ij} is the Kronecker delta. It is straightforward to show that for a cubic system, there are only two magnetoelastic coupling coefficients B_1 and B_2 [25–27]. For the isotropic case there is only one coefficient. Note that the interaction must be quadratic in the magnetization to satisfy time-reversal symmetry. It can be shown that the magnetoelastic coupling leads to an equilibrium uniaxial strain ("magnetostriction") determined by the direction of the magnetization [27]. These strains are given by $u_{ii} = \lambda_{100} m_i^2$ and $u_{ij} = \lambda_{111} m_i m_j$. The two magnetostrictive coefficients λ_{100} and λ_{111} represent the strain of the material along the direction of the magnetization for magnetization oriented along $\langle 100 \rangle$ and $\langle 111 \rangle$, respectively. Thus, when the magnetization is oriented along a $\langle 100 \rangle$ axis ($m_1 = 1$), the coupling of the magnetization to longitudinal phonons is represented by λ_{100} and to transverse phonons by λ_{111}. As first pointed out by Kittel [25], the coupling to transverse phonons is much stronger than it is to longitudinal phonons because the transverse coupling terms can be effectively linear in the magnetization. To see why this is, consider the case of magnetization saturated along the [001] direction. When the magnetization undergoes small-angle precession, $m_3 \approx 1$ and $m_1 \approx m_2 \ll 1$. From

this we can write $u_{i3} \approx \lambda_{111} m_i$ ($i = 1$ or 2). The longitudinal strains are quadratic in m_1 and m_2 and are therefore much smaller. This fact will be revisited in Chapters 4 and 5 where its importance will be made evident.

1.3.3 Perpendicular Magnetic Anisotropy

When the value of $2K_u/M_s$ is greater than $4\pi M_s$ in a thin film, $4\pi M_{eff}$ is negative and the film is said to have perpendicular magnetic anisotropy (PMA). In this case it is energetically favorable for the magnetization to point perpendicular to the plane. Systems with PMA are, generally speaking, of more interest for spintronic applications. In this thesis, we will discuss three different PMA systems. Co/Pd multilayers (superlattices) are the subject of Chapter 5. In this case the PMA arises from the interfaces of the ultrathin ($\sim$0.8 nm) Co layers. Interfacial PMA is the most common. Appendix D contains results on Bi-doped yttrium iron garnet films (BiYIG), where the PMA results from a magnetoelastic anisotropy caused by the epitaxial strain of the film. (The substrate must be carefully chosen if the film is to have PMA.) Lastly, Appendix E examines the dynamics of FePd, which show PMA in the bulk. "PMA in the bulk" really means a strong uniaxial anisotropy arising from bulk crystal structure. For such a material to have PMA, it must be grown as a thin film with the easy axis (in this case, the c-axis) aligned to the film normal.

1.3.4 Gilbert Damping

To account for dissipation in the magnetization dynamics, we will modify Eq. 1.2 to include a phenomenological dampinglike torque in the form introduced by Gilbert [28]:

$$\frac{d\mathbf{M}}{dt} = \gamma \mathbf{M} \times \mathbf{H}_{eff} - \frac{\alpha}{M_s} \mathbf{M} \times \frac{d\mathbf{M}}{dt} \ , \tag{1.10}$$

where α is the Gilbert damping constant—a central theme of this thesis. Equation 1.10 is commonly referred to as the Landau-Lifshitz-Gilbert (LLG) equation. It can be shown that for $\alpha \ll 1$, Eq. 1.6 and Eq. 1.7 remain good approximations. Equation 1.10 is solved for the dynamic magnetization $\mathbf{m}(t)$ which is linearly related to the alternating applied field $\mathbf{h}(t)$ in the small precession amplitude regime. This linear relationship is given by $\mathbf{m} = \boldsymbol{\chi}(\omega) \cdot \mathbf{h}$, where $\boldsymbol{\chi}(\omega)$ is the dynamic susceptibility tensor. The components of

$\boldsymbol{\chi}(\omega)$ are Lorentzians, the imaginary parts of which are related to the power absorption of the magnetic film. It is straightforward to obtain the linewidth of the Lorentzians:

$$\Delta H_{FWHM} = \frac{2\alpha\omega}{\gamma} \ , \tag{1.11}$$

where ΔH_{FWHM} is the full-width-at-half-maximum (FWHM) of the absorption peak when the magnetic field H_0 is varied and the frequency ω is held fixed. ΔH_{FWHM} is related to the linewidth in the frequency domain through $\Delta H_{FWHM} = (d\omega/dH)^{-1} \Delta\omega_{FWHM}$. Equation 1.11 is used to experimentally determine the Gilbert damping α: The field-swept linewidth ΔH_{FWHM} is measured as a function of applied frequency, and the slope of resulting line is proportional to α. The gyromagnetic ratio γ is usually obtained by fits to Eq. 1.6 or Eq. 1.7, depending on the direction of the applied field H_0.

1.3.5 Kamberský Damping

In the previous section it was mentioned that the introduction of Gilbert damping is a phenomenological way of handling dissipation in magnetization dynamics. In this section, we introduce some of the work that has been done to understand damping from a first-principles viewpoint, much of which has followed from the work of Kamberský [29–31]. In the literature, it is common to separate Kamberský damping into two distinct mechanisms: conductivity-like damping and resistivity-like damping. The nomenclature is due to the fact that the former scales with the electronic relaxation time τ and the latter inversely so, which will soon be shown.

The approach of Kamberský is essentially to take the spin-orbit interaction, manipulate it with Kubo formalism, and extract a susceptibility from which a damping constant can be identified. For this problem, the relevant fluctuation-dissipation relation connects the magnetization damping and spin-orbital torque correlations, and for this reason the model is frequently called the Kamberský torque-correlation model. Probably the most oft-cited result of Kamberský [30] is the following expression for the Gilbert damping coefficient:

$$\alpha = \frac{\gamma\hbar}{M_s} \sum_{n,m} \int \frac{d\mathbf{k}}{(2\pi)^3} |\Gamma^-_{nm}(\mathbf{k})|^2 W_{nm}(\mathbf{k}) \tag{1.12}$$

where $\Gamma^-_{nm}(\mathbf{k}) = \langle n, \mathbf{k}| \left[\sigma^-, H_{SO}\right] |m, \mathbf{k}\rangle$ are the matrix elements of the spin-orbital

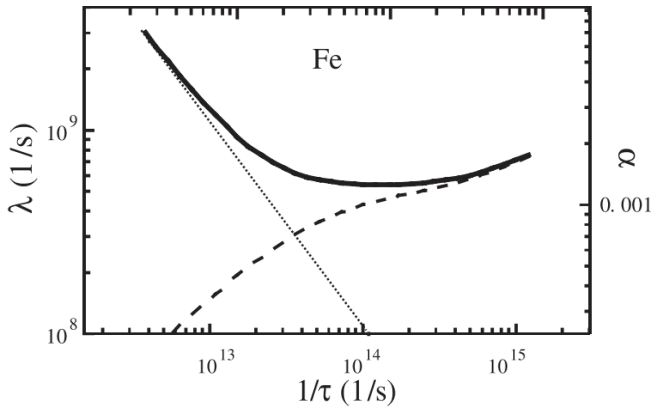

Figure 1.1: Dependence of Gilbert damping on electronic relaxation time in Fe using the Kamberský torque-correlation model. Solid line indicates total damping, dotted line indicates intraband scattering contribution, and dashed line indicates interband scattering contribution. From Ref. [1].

torque operator and $W_{nm}(\mathbf{k})$ is the spectral overlap function of bands n and m. Explicitly, the spectral overlap function is given by

$$W_{nm}(\mathbf{k}) = \frac{1}{\pi}\int \frac{d\epsilon}{\hbar}\left(-\frac{df(\epsilon)}{d\epsilon}\right) A_{n\mathbf{k}}(\epsilon)A_{m\mathbf{k}}(\epsilon) \tag{1.13}$$

where $f(\epsilon)$ is the equilibrium Fermi occupation factor and the electron spectral functions $A_{n\mathbf{k}}(\epsilon)$ are Lorentzians centered at $\epsilon_{n\mathbf{k}}$ of width $\hbar/\tau$ [1], with τ the electronic relaxation time. The Lorentzians are broadened in order to phenomenologically account for electronic scattering mechanisms, which play a critical role. In many cases, it is sufficient to think of $|\Gamma^{-}_{nm}(\mathbf{k})|^2$ as the strength of the spin-orbit interaction. (This is not the case for considerations of anisotropic damping, however, where this quantity can depend on the orientation of the magnetization and must be handled carefully [32, 33]). Eq. 1.12 includes two types of scattering processes: intraband scattering ($m = n$) and interband scattering ($m \neq n$). We now proceed to treat each case separately and will see that intraband scattering is connected with conductivity-like damping and interband scattering with resistivity-like damping.

Intraband Scattering

In this section we estimate the damping that comes from intraband scattering. We will not take Eq. 1.12 as a starting point. Rather, we begin with the breathing Fermi surface approach [29, 34]. This approach is less rigorous, but has the advantage of providing an intuitive picture of the scattering processes and will give us the appropriate dependence on the relaxation time τ. The basic premise of this argument is that the Fermi surface will acquire a time dependence when the magnetization precesses, which is due to the spin-orbit interaction. Consequently, the equilibrium states have a time-dependent occupation due to the finite electronic momentum relaxation time. We start by considering the effective field due to the population of excited electronic states:

$$\mathbf{H}_{intra} = -\sum_{n,\mathbf{k}} \rho_{n\mathbf{k}} \nabla_{\mathbf{M}} \epsilon_{n\mathbf{k}} \tag{1.14}$$

where $\rho_{n\mathbf{k}}$ is the instantaneous occupation of the state $|n, \mathbf{k}\rangle$ and $\epsilon_{n\mathbf{k}}$ is the energy of this state. We assume, in a relaxation-time approximation, that the occupation number obeys the simple rate law

$$\frac{d\rho_{n\mathbf{k}}}{dt} = -\frac{\rho_{n\mathbf{k}} - f_{n\mathbf{k}}}{\tau} \tag{1.15}$$

where $f_{n\mathbf{k}}$ is the equilibrium occupation number and τ is the electronic relaxation time, which we will take to be independent of n and $\mathbf{k}$. We solve for $\rho_{n\mathbf{k}}$ at timescales slow compared to the local relaxation time τ,

$$\rho_{n\mathbf{k}} = f_{n\mathbf{k}} - \tau \frac{df_{n\mathbf{k}}}{dt} \tag{1.16}$$

and substitute into Eq. 1.14:

$$\mathbf{H}_{intra} = -M_s^{-2} \sum_{i,j} \mathbf{R} \cdot \frac{d\mathbf{M}}{dt} \ , \tag{1.17}$$

where

$$\mathbf{R}_{ij} = -\sum_{n,\mathbf{k}} \frac{\partial f_{n\mathbf{k}}}{\partial \epsilon_{n\mathbf{k}}} \frac{\partial \epsilon_{n\mathbf{k}}}{\partial \alpha_i} \frac{\partial \epsilon_{n\mathbf{k}}}{\partial \alpha_j} \tau \tag{1.18}$$

and $\alpha_i = M_i/M_s$ are the direction cosines of the magnetization. For small deviations from equilibrium, $\partial \epsilon_{n\mathbf{k}}/\partial \alpha_i$ are evaluated at the equilibrium position. The factor of $df_{n\mathbf{k}}/d\epsilon$ is sharply peaked at the Fermi level and can be approximated by $N(\epsilon_F)$ upon

summation. It remains to find the change in energy levels $\partial\epsilon_{n\mathbf{k}}/\partial\alpha_i$ resulting from precession. When the magnetization is aligned with a high-symmetry direction, the precession is confined to the plane normal to the static magnetization, which we take to be the x-y plane. If we assume that the spin-orbital torque is isotropic, then we can estimate $(\partial\epsilon_{n\mathbf{k}}/\partial\alpha_i)^2 \simeq 1/2|\Gamma^-|^2$. Then by comparing with Eq. 1.10, we have the following estimate for the Gilbert damping due to intraband scattering:

$$\alpha \approx \frac{3}{2}\frac{\gamma}{M_s}N(\epsilon_F)|\Gamma^-|^2\tau \ , \tag{1.19}$$

which indeed scales with the relaxation time and thus the conductivity. In addition, Schoen *et al.* [35] have shown a correlation between α and the $N(\epsilon_F)$ obtained from electronic structure calculations. Khodadadi *et al.* [36] recently demonstrated conductivity-like behavior in clean epitaxial Fe.

Interband Scattering

In the case of interband scattering, the connection to the electronic relaxation time is even clearer. When $n \neq m$ in Eq. 1.13, the overlap of the electronic spectral functions $A_{n\mathbf{k}}$ and $A_{m\mathbf{k}}$ is greater when the spectral width (relaxation time) is larger (smaller). Thus, for $n \neq m$, the contribution to α scales inversely with the electronic relaxation time and is aptly referred to as resistivity-like damping.

The bubbling Fermi surface model is a common picture of interband scattering [1, 37]. The magnetization precession can be thought of as a time-dependent perturbation to the spin-orbit interaction which induces transitions between bands. These are called spin-flip transitions, which are suppressed in Heusler alloys with high spin polarization due to the large exchange-driven band splitting. The effective field resulting from these transitions is

$$\mathbf{H}_{inter} = -\sum_{n,\mathbf{k}} \epsilon_{n\mathbf{k}} \nabla_{\mathbf{M}} \rho_{n\mathbf{k}} \ . \tag{1.20}$$

Note the similarity to Eq. 1.14: Intraband scattering arises from time-dependent energy levels, whereas interband scattering originates from time-dependent occupation numbers. The transition rate between bands n and m is given by Fermi's golden rule:

$$\Lambda_{nm}(\mathbf{k}) = \frac{2\pi}{\hbar}|\Gamma^-_{nm}(\mathbf{k})|^2\delta(\epsilon_n - \epsilon_m - \hbar\omega) \ , \tag{1.21}$$

where $\Gamma^{-}_{nm}(\mathbf{k})$ is the spin-orbital torque matrix element and ω is the rate of spin precession. The occupation numbers obey the Lindblad master equation:

$$\frac{\partial \rho_{n\mathbf{k}}}{\partial t} = \sum_{m \neq n} \Lambda_{nm}(\mathbf{k}) \left[\rho_{m\mathbf{k}} - \rho_{n\mathbf{k}}\right] \ . \tag{1.22}$$

This rate law can be written in the form of an effective field via Eq. 1.20

$$\mathbf{H}_{eff} = -\frac{1}{8\pi M_s} \sum_{n,\mathbf{k}} \sum_{m \neq n} \frac{\Lambda_{nm}(\mathbf{k})}{\omega^2} \left[\rho_{n\mathbf{k}} - \rho_{m\mathbf{k}}\right] \left[\epsilon_{n\mathbf{k}} - \epsilon_{m\mathbf{k}}\right] \frac{d\mathbf{M}}{dt} \tag{1.23}$$

and compared to Eq. 1.10 to yield an expression for the interband Gilbert damping:

$$\alpha = \frac{\hbar^2 \gamma}{8\pi M_s} \sum_{n,\mathbf{k}} \sum_{m \neq n} \int d\epsilon_1 \, A_{n\mathbf{k}}(\epsilon_1) \int d\epsilon_2 \, A_{m\mathbf{k}}(\epsilon_2) \Lambda_{nm}(\mathbf{k}) \frac{f(\epsilon_2) - f(\epsilon_1)}{\hbar\omega} \frac{\epsilon_2 - \epsilon_1}{\hbar\omega} \ . \tag{1.24}$$

We now insert Eq. 1.21 for the transition rate, integrate over ϵ_2, and take the limit as $\omega \to 0$:

$$\alpha = \frac{\hbar\gamma}{4M_s} \sum_{n} \sum_{m \neq n} \int \frac{d\mathbf{k}}{(2\pi)^3} |\Gamma^{-}_{mn}|^2 \int d\epsilon_1 \, A_{n\mathbf{k}}(\epsilon_1) A_{m\mathbf{k}}(\epsilon_1) \left(-\frac{df(\epsilon_1)}{d\epsilon_1}\right) \ , \tag{1.25}$$

thereby obtaining a final expression which scales with resistivity (from the integral over ϵ_1, i.e. the spectral overlap) and agrees with Kamberský's torque-correlation model (Eq. 1.12).

1.3.6 Temperature Dependence of Gilbert Damping

The dependence of the Gilbert damping α on temperature (assuming the Kamberský contribution dominates) is determined in large part by the temperature dependence of the electronic relaxation time through the conductivity-like and resistivity-like Kamberský damping mechanisms. Figure 1.1 shows the dependence of the Gilbert damping α on the electronic relaxation time τ in Fe calculated in Ref. [1]. Intraband scattering dominates at high relaxation times and interband scattering at low relaxation times. Thus, one would expect the damping to decrease with increasing temperature at low temperatures, and increase with increasing temperature at high temperatures.[1]

[1] It is possible to observe both regimes in an individual sample, but very difficult. From Fig. 1.1 it is clear that the minimum in α as a function of scattering rate $1/\tau$ is rather broad. The electronic scattering rate would need to be tuned over at least two orders of magnitude to establish crossover behavior.

1.4 Ferromagnetic Resonance Experiment

A schematic of the FMR experimental setup used in the experiment discussed in this thesis is shown in Fig. 1.2. Explanations of this particular style of FMR measurement as well as other common styles can be found in Refs. [38–42]. The sample is placed face down on a coplanar waveguide (CPW) where it experiences a microwave magnetic field h_{mw} responsible for exciting the magnetization dynamics. The transmitted microwave power is measured using a rectifying diode, with the diode output connected to a lock-in amplifier. The applied magnetic field H consists of a static component H_0 and a time-varying component for field modulation $h_{fm}e^{i\omega t}$, with h_{fm} approximately a few Oe and $\omega/2\pi \simeq 200$ Hz, which is referenced by the lock-in amplifier. For a fixed microwave frequency, the static applied field H_0 is swept through the FMR field. The absorbed power for a given applied field is proportional to the imaginary ac susceptibility $\chi''(H_0 + h_{fm}e^{i\omega t})$, which in the limit of small h_{fm} can be approximated as $\chi''(H_0)+(d\chi''/dH)|_{H_0}h_{fm}e^{i\omega t}$. The lock-in amplifier selects the component of the signal oscillating at ω, making it so that the differential absorption $d\chi''/dH$ is measured. This has the advantage of removing background signals that do not depend on the applied field.

Figure 1.3 shows exemplary FMR lineshapes for a $[Co/Pd]_6$ multilayer[2] at (a) 10 K and (b) 300 K, both with perpendicular applied fields and microwave excitations of 40 GHz. The differential ac susceptiblity $d\chi/dH$ is fit to the derivative of a Lorentzian curve:

$$\begin{aligned} d\chi''/dH &\propto \frac{d}{dH}\left(\frac{\Delta H_{FWHM}/2}{(H_0 - H_{FMR})^2 + (\Delta H_{FWHM}/2)^2}\right) \\ &= \frac{-\Delta H_{FWHM}(H_0 - H_{FMR})}{((H_0 - H_{FMR})^2 + (\Delta H_{FWHM}/2)^2)^2}\ , \end{aligned} \tag{1.26}$$

where H_{FMR} is the FMR field and ΔH_{FWHM} is the full-width-at-half-maximum FMR linewidth. Both of these values are extracted from fits of the data to Eq. 1.26. As indicated in Fig. 1.3(a), the separation between extrema in a derivative lineshape is equal to $\Delta H_{FWHM}/\sqrt{3}$.

[2] Among the series of Co/Pd multilayers which are the focus of Chapter 5

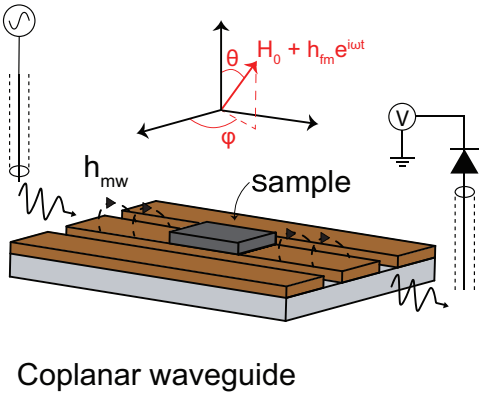

Figure 1.2: Schematic diagram of the FMR experimental setup showing sample, coplanar waveguide, and remaining microwave circuitry. A microwave source is used to generate the microwave frequency magnetic field h_{mw} for exciting magnetization dynamics in the sample. The applied magnetic field consists of a static component H_0 and a small (few Oe) oscillating component $h_{fm}e^{i\omega t}$ ($\omega/2\pi \simeq 200$ Hz) which is referenced to a lock-in amplifier.

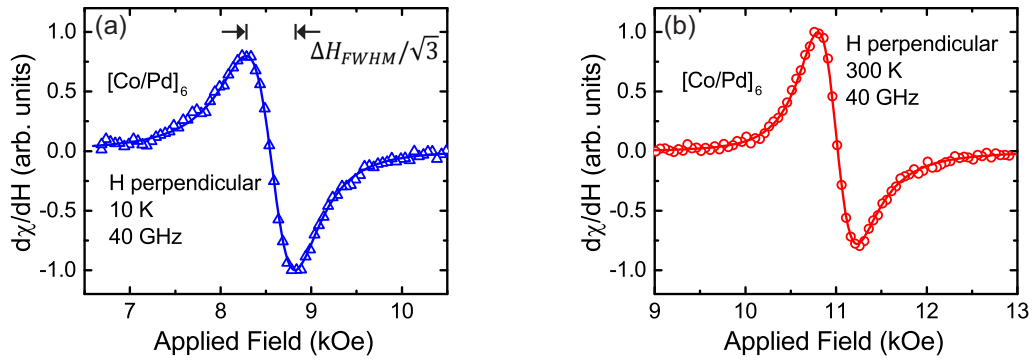

Figure 1.3: Example FMR lineshapes for a $[Co/Pd]_6$ multilayer at temperatures of (a) 10 K and (b) 300 K. For both cases the frequency of the microwave excitation was 40 GHz with magnetic field applied perpendicular to the plane. In panel (a) it is indicated that the separation between peaks is equal to the full-width-at-half-maximum linewidth ΔH_{FWHM} reduced by a factor of $\sqrt{3}$.

Chapter 2

Two-Magnon Scattering: Damping

2.1 Introduction

The theoretical understanding of the damping mechanism believed to govern longitudinal magnetization relaxation in metallic ferromagnets, originally due to Kamberský [29, 30], has in recent years resulted in quantitative damping estimates for realistic transition metal band structures [1, 32, 43]. Although of great interest where engineering of damping is desired [44], these calculations remain largely uncompared to experimental data. Kamberský damping may be characterized by the so-called Gilbert damping constant α in the Landau-Lifshitz-Gilbert macrospin torque equation of motion, and formally describes how the spin-orbit interaction in itinerant electron systems results in damping of magnetization dynamics [30]. Schoen *et al.* [35] have reported that α is minimized for Co-Fe alloy compositions at which the density-of-states at the Fermi level is minimized, in agreement with the Kamberský model prediction [45]. Furthermore, half-metallic, or nearly half-metallic ferromagnets such as full-Heusler compounds have been predicted to demonstrate an ultralow Kamberský α ($\leq 10^{-3}$) due to their spin-resolved band structure near the Fermi level [18]. Finally, anisotropy of the Kamberský damping in single crystals has been predicted, which is more robust for Fermi surfaces with single-band character [32, 33].

The Gilbert damping constant is often reported through measurements of the ferromagnetic resonance (FMR) linewidth ΔH, which may be expressed as a sum of individual contributions

$$\Delta H = \frac{2\alpha f}{\gamma} + \Delta H_0 + \Delta H_{TMS}, \tag{2.1}$$

where the first term is the Gilbert damping linewidth (f is the FMR frequency, γ is the gyromagnetic ratio), ΔH_0 is a frequency-independent inhomogeneous broadening, and ΔH_{TMS} represents an extrinsic two-magnon scattering (TMS) linewidth contribution [46, 47] that is, in general, a nonlinear function of frequency. In recent years it has been realized that TMS linewidths are pervasive for the conventional in-plane geometry of thin film FMR measurements, requiring either the perpendicular-to-plane FMR geometry [48] (for which TMS processes are suppressed) or sufficiently broadband measurements [49] to extract the bare Gilbert α. For instance, recent FMR linewidth studies on Heusler compounds have reported distinct TMS linewidths [50, 51], which challenged a simple inference of the Gilbert α.

In this chapter, we present FMR linewidth measurements for epitaxial Heusler thin films for all principal orientations of the magnetization with respect to the symmetry axes. For the in-plane configuration, large and anisotropic TMS-dominated linewidths are observed. In the perpendicular-to-plane configuration, for which the TMS process is inactive [46], the Gilbert α and inhomogeneous broadening are measured. We find evidence of a low ($\sim 10^{-3}$) Gilbert α in these Heusler thin films, accompanied by a large and anisotropic TMS contribution to the linewidth for in-plane magnetization. We conclude by discussing the interplay of low Gilbert α and large TMS, and we emphasize the nature by which the TMS may conceal the presence of anisotropic Kamberský α. The work presented in this chapter was published in *Physical Review B* (see Ref. [52]).

2.2 Samples

The Heusler alloy films used for these measurements were grown by molecular beam epitaxy (MBE) by co-evaporation of elemental sources in ultrahigh vacuum (UHV). The MgO(001) substrates were annealed at 700 °C in UHV followed by growth of a 20 nm thick MgO buffer layer by e-beam evaporation at a substrate temperature of 630 °C. The 10 nm thick Co_2MnAl and Co_2MnSi films were grown on the MgO buffer

layers at room temperature and then annealed at 600 °C for 15 minutes *in situ* in order to improve crystalline order and surface morphology. The 24 nm thick Co_2FeAl sample was grown using the same MgO substrate and buffer layer preparation, but at a substrate temperature of 250 °C with no post-growth anneal. Reflection high energy electron diffraction (RHEED) was monitored during and after growth of all samples and confirmed the expected epitaxial relationship of MgO(001)$\langle 110 \rangle$ || Heusler(001)$\langle 100 \rangle$. X-ray diffraction (XRD) demonstrated the existence of a single phase of (001)-oriented Heusler, along with the presence of the (002) reflection, confirming at least B2 ordering in all cases. In addition, for the Co_2MnSi film only, the (111) reflection was observed, indicating $L2_1$ ordering [see Fig. 2.1(a)]. (The process by which chemical ordering is determined using XRD is discussed in Appendix B.) All of the films were capped with several nm of e-beam evaporated AlOx for passivation prior to atmospheric exposure. The effective magnetization for the 24 nm thick Co_2FeAl film was determined from anomalous Hall effect saturation field to be 1200 emu/cm^3, which is consistent with measurements of Ref. [53] for $L2_1$ or B2-ordered films, along with 990 emu/cm^3 and 930 emu/cm^3 for the Co_2MnSi and Co_2MnAl films, respectively. Hereafter, we will refer to the Co_2MnSi(10 nm)/MgO as the "CMS" film, the Co_2MnAl(10 nm)/MgO film as the "CMA" film, and the Co_2FeAl(24 nm)/MgO film as the "CFA" film.

2.3 Experiment

Broadband FMR linewidth measurements were performed at room temperature with a coplanar waveguide (CPW) transmission setup, similar to that discussed in detail in Refs. [38, 40], placed between the pole faces of an electromagnet. A cleaved piece of the sample ($\sim$2 mm$\times$1 mm) was placed face-down over the centerline of the CPW. A rectifying diode was used to detect the transmitted microwave power, and a $\sim$100 Hz magnetic field modulation was used for lock-in detection of the transmitted power, resulting in a signal $\propto d\chi/dH$ (where χ is the film dynamic magnetic susceptibility). The excitation frequency could be varied from 0 to 50 GHz, and a microwave power near 0 dBm was typically used. It was verified that all measurements discussed in this chapter were in the small precession cone angle, linear regime. The orientation of the applied magnetic field could be rotated to arbitrary angle in the film plane (IP), or applied

Table 2.1: Summary of the magnetic properties extracted from the dependence of the resonance field on applied frequency for both field in-plane (||) and field perpendicular-to-plane ($\perp$) configurations. $2K_1/M_s$ and $4\pi M_{eff}$ are the in-plane and perpendicular-to-plane anisotropy fields, respectively (see Eq. 2.2), and g is the Landé g-factor.

Sample	$2K_1/M_s$ (Oe)	$4\pi M_{eff}^{\|\|}$ (kOe)	$4\pi M_{eff}^{\perp}$ (kOe)	$g^{\|\|}$	$g^{\perp}$
CMS	280	12.3	13.3	2.04	2.04
CMA	35	11.3	11.7	2.06	2.08
CFA	230	15.1	15.5	2.06	2.07
CFA 500 °C anneal	N/A	N/A	15.1	N/A	2.07

perpendicular to the film plane (PP). We emphasize again that TMS contributions are suppressed in the PP configuration [47]. The resonance fields were fit as a function of applied frequency in order to extract various magnetic properties of the films.

The magnetic free energy per unit volume used to generate the resonance conditions for these samples is given by

$$F_{\mathbf{M}} = -\mathbf{M}\cdot\mathbf{H} + K_1 \sin^2\phi\cos^2\phi + 2\pi M_{eff}^2 \cos^2\theta, \tag{2.2}$$

where $\mathbf{H}$ is the applied field, ϕ and θ are the azimuthal and polar angles of the magnetization, respectively, K_1 is a first order in-plane cubic anisotropy constant, and $4\pi M_{eff}$ is the PP saturation field, which includes the usual demagnetization energy and a first order uniaxial anisotropy due to interfacial effects. The parameters obtained by fitting to Eq. 2.2 are shown in Table 2.1. The uncertainty in these parameters was estimated by measuring a range of different sample pieces, and using the standard deviation of the values as the error bar. The long-range inhomogeneity characteristic of epitaxial samples makes this a more accurate estimate of the uncertainty than the fitting error. The magnetic-field-swept FMR lineshapes were fit to the derivative of Lorentzian functions [40] in order to extract the full-width at half-maximum linewidths ΔH [magnetic field units, Fig. 2.1(b)]. The maximum resonant frequency was determined by the maximum magnetic field that could be applied for both IP and PP electromagnet configurations, which was 10.6 kOe and 29 kOe, respectively. For the IP measurement, the angle of the applied field in the plane of the film was varied to determine the in-plane magnetocrystalline anisotropy of our samples, which was fourfold-symmetric for the three films characterized in this article. The anisotropy was confirmed using vibrating-sample

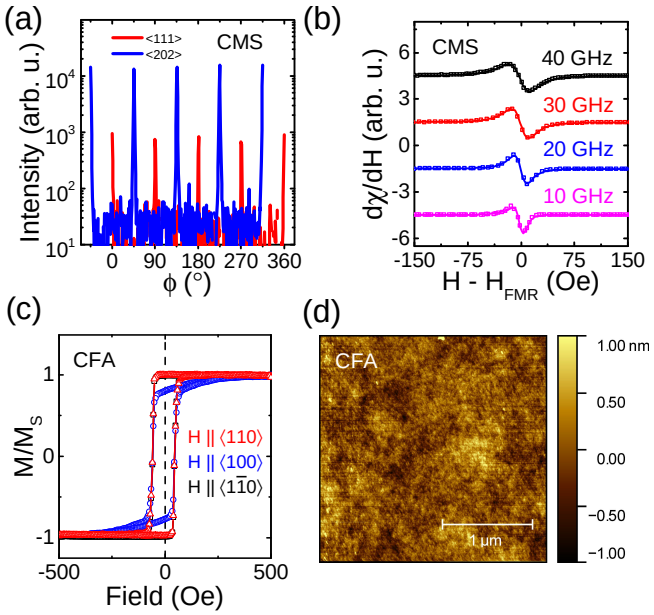

Figure 2.1: (a) Wide-angle x-ray diffraction ϕ-scans of $\langle 202 \rangle$ (blue) and $\langle 111 \rangle$ (red) peaks for the CMS film. (b) Typical derivative susceptibility lineshapes for these samples at different microwave excitation frequencies. The fits are shown as solid lines. (c) In-plane hysteresis loops for CFA obtained with a vibrating-sample magnetometer (VSM). (d) Atomic force microscopy (AFM) image of surface topography for CFA. RMS roughness is 0.2 nm.

Table 2.2: Gilbert damping α and inhomogeneous broadening ΔH_0 from the measurements in the perpendicular-to-plane configuration.

Sample	$\alpha_{001}(\times 10^{-3})$	ΔH_0 (Oe)
CMS	1.5 ± 0.1	9 ± 1
CMA	1.8 ± 0.2	12 ± 3
CFA	< 0.8	100 ± 6
CFA 500 °C anneal	1.1 ± 0.1	45 ± 1

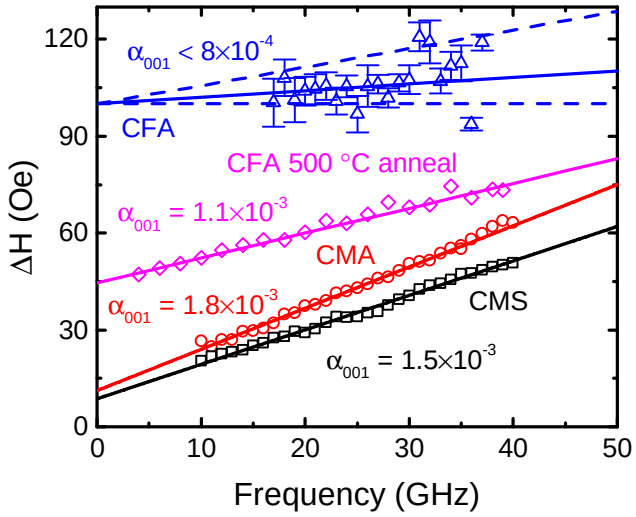

Figure 2.2: Linewidths as a function of frequency with the field applied perpendicular to plane, for which two-magnon scattering is inactive. The black squares are data for the CMS film, the red circles are for the CMA film, and the blue triangles are for the CFA film. In addition, linewidths are shown for a CFA film that was annealed at 500 °C *ex situ* (magenta diamonds). Corresponding linear fits are shown along with the extracted Gilbert damping factor α. The blue dashed lines indicate an upper bound of $\alpha_{001} = 8 \times 10^{-4}$ and a lower bound of $\alpha_{001} = 0$ for CFA.

magnetometry (VSM) measurements, an example of which is shown in Fig. 2.1(c), which shows IP easy and hard axis hysteresis loops for the CFA film. For the PP measurement, alignment was verified to within $\sim$0.1° to ensure magnetization saturation just above the PP anisotropy field, thus minimizing field-dragging contributions to the linewidth (artificial broadening due to **M** and **H** not being parallel).

2.4 Results and Analysis

2.4.1 Perpendicular-to-plane linewidths

First we discuss the results of the PP measurement. As stated in Sec. 2.3, the TMS extrinsic broadening mechanism is suppressed when the magnetization is normal to the plane of the film. We can thus fit our data to Eq. 2.1 with $\Delta H_{TMS} = 0$, greatly simplifying the extraction of the Gilbert damping constant α and the inhomogeneous

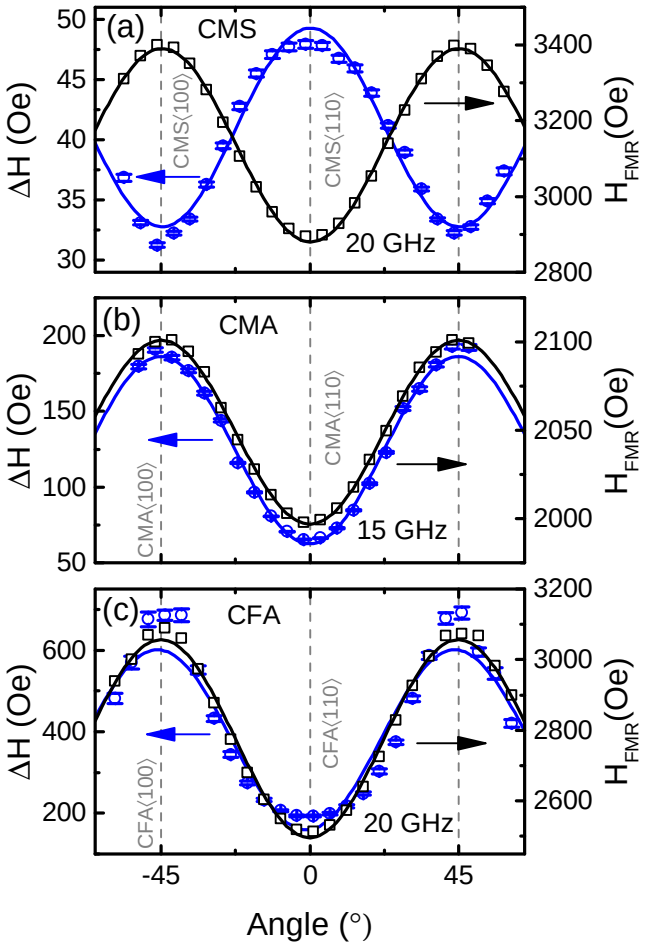

Figure 2.3: Azimuthal angular dependence of the linewidths (left ordinate, blue circles) and resonance fields (right ordinate, black squares) for (a) CMS, (b) CMA, and (c) CFA. The excitation frequency was 20 GHz for CMS, 15 GHz for CMA, and 20 GHz for CFA. The solid lines are sinusoidal fits.

broadening ΔH_0. Prior knowledge of ΔH_0 is particularly important for constraining the analysis of the IP measurements, as we shall discuss.

The dependence of ΔH on frequency for the CMS, CMA, and CFA films in the PP configuration is summarized in Fig. 2.2, in which fits to Eq. 2.1 are shown with ΔH_{TMS} set to zero. For the CMS film, $\alpha_{001} = (1.5 \pm 0.1) \times 10^{-3}$ and $\Delta H_0 = 9$ Oe, while for the CMA film $\alpha_{001} = (1.8 \pm 0.2) \times 10^{-3}$ and $\Delta H_0 = 12$ Oe. $Co_2MnSi_{2/3}Al_{1/3}$/MgO and $Co_2MnSi_{1/3}Al_{2/3}$/MgO films (both 10 nm thick) were also measured, with Gilbert damping values of $\alpha_{001} = (1.8 \pm 0.2) \times 10^{-3}$ and $\alpha_{001} = (1.5 \pm 0.1) \times 10^{-3}$, respectively (not shown). For CFA, we obtained a damping value of $\alpha_{001} = 3 \times 10^{-4}$ with an upper bound of $\alpha_{001} < 8 \times 10^{-4}$ and $\Delta H_0 = 100$ Oe. These fit parameters are also contained in Table 2.1. The source of the large inhomogeneous broadening for the CFA film is unclear: AFM measurements [Fig. 2.1(d)] along with XRD indicate that the film is both crystalline and smooth (RMS roughness ∼0.2 nm). Note that the range of frequencies shown in Fig. 2.2 are largely governed by considerations involving the Kittel equation [21]: measurements below 10 GHz were not used due to the increasing influence of slight misalignment on ΔH (through field-dragging) for resonant fields just above the saturation value. A piece of the CFA sample was annealed at 500 °C *ex situ*, which reduced the inhomogenoeus broadening to ∼45 Oe (still a relatively large value) and increased the Gilbert damping to $\alpha_{001} = 1.1 \times 10^{-3}$ (similar behavior in CFA was seen in Ref. [54]). The constraint of $\alpha_{001} < 8 \times 10^{-4}$ is among the lowest of reported Gilbert damping constants for metallic ferromagnets, but the $\alpha \sim 10^{-4}$ range is not unexpected based on Kamberský model calculations performed for similar full-Heusler compounds [18] or other recent experimental reports [55, 56]. It should be noted that Schoen *et al.* [35] have recently reported $\alpha = 5 \times 10^{-4}$ for $Co_{25}Fe_{75}$ thin films, where spin pumping and radiative damping contributions were subtracted from the raw measurement. Spin pumping contributions to the intrinsic damping are not significant in our films, as no heavy-metal seed layers have been used and the films have thicknesses of 10 nm or greater. For the radiative damping contribution [48] in the geometry of our CPW and sample, we calculate contributions $\alpha_{\mathrm{rad}} \lesssim 1 \times 10^{-4}$, which is below the uncertainty in our damping fit parameter.

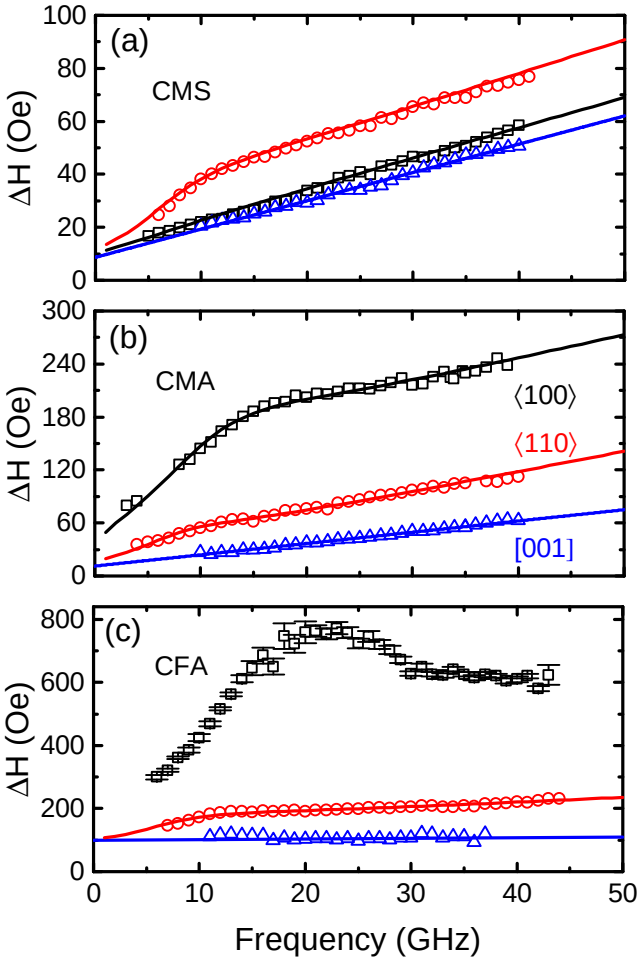

Figure 2.4: Linewidths along all three principal directions for CMS (a), CMA (b), and CFA (c). Heusler crystalline axes are labeled by ⟨100⟩ (black), ⟨110⟩ (red), and [001] (blue). In all three cases, ⟨110⟩ is the in-plane easy axis and ⟨100⟩ is the in-plane hard axis. The corresponding fits are shown as the solid curves, where the in-plane linewidths are fit using Eq. 2.3 and the out-of-plane linewidths are fit to the Gilbert damping model. The fit parameters are given in Table 2.3.

2.4.2 In-plane linewidths

With the intrinsic damping and inhomogeneous broadening characterized by the PP measurement, we turn our attention to the IP linewidth measurements, for which TMS contributions are present. For hard-axis measurements, frequencies $\lesssim 5$ GHz were not used due to the influence of slight magnetic field misalignment on the linewidths. For easy-axis measurements, the lower limit is determined by the zero-field FMR frequency. Figure 2.3 shows the dependences of the resonance fields and linewidths on the angle of the in-plane field. An important observation seen in Fig. 2.3 is that the linewidth extrema are commensurate with those of the resonance fields and therefore the magnetocrystalline anisotropy energy. This rules out field-dragging and mosaicity contributions to the linewidth, which can occur when the resonance field depends strongly on angle [57]. We note that similar IP angular dependence of the FMR linewidth, which was attributed to an anisotropic TMS mechanism caused by a rectangular array of misfit dislocations, has been reported by Kurebayashi *et al.* [58] and Woltersdorf and Heinrich [49] for epitaxial Fe/GaAs(001) ultrathin films.

To further study the anisotropy of the IP ΔH in our films, we have measured ΔH at the angles corresponding to the extrema of H_{FMR} (and ΔH) in Fig. 2.3 over a range of frequencies. These data are shown in Fig. 2.4, along with the PP ([001]) measurements for each sample. A distinguishing feature of the data shown in Fig. 2.4 is the significant deviation between IP and PP linewidths in all but one case (CMS$\langle 100 \rangle$). Large and nonlinear frequency dependence of the IP linewidths is strongly suggestive of an active TMS linewidth broadening mechanism. In the presence of TMS, careful analysis is required to separate the Gilbert damping from the TMS linewidth contributions. We therefore describe the TMS mechanism in more detail in the following section in order to analyze the IP linewidths in Fig. 2.4 and extract the Gilbert damping.

2.4.3 Two-magnon scattering model

The TMS mechanism leads to a characteristic nonlinear frequency dependence of ΔH [46, 47]. In Fig. 2.4, the IP ΔH is not a linear function of frequency, but possesses the "knee" behavior characteristic of the frequency dependence of linewidths dominated by the TMS mechanism. We have fit our data to the TMS model described by McMichael

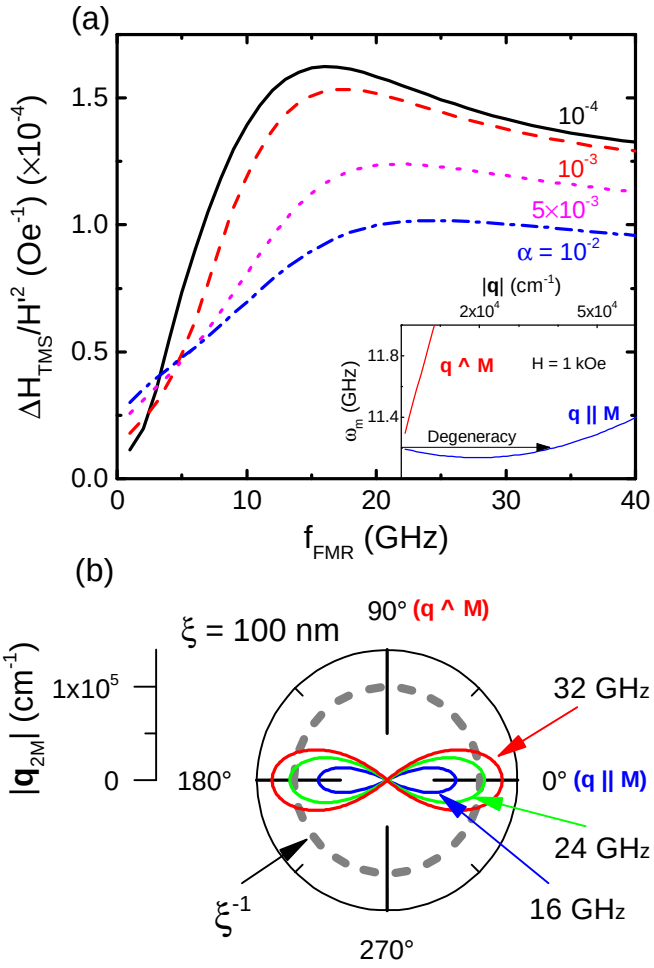

Figure 2.5: (a) Two-magnon scattering linewidth contribution for values of Gilbert damping $\alpha = 10^{-2}, 5 \times 10^{-3}, 10^{-3}$, and 10^{-4}. The inset shows magnon dispersions for an applied field of $H = 1$ kOe. (b) Contours of the degenerate mode wavenumber $\mathbf{q}_{2M}$ in the film plane as a function of wavevector angle relative to the magnetization for $f_{FMR} = 16$, 24, and 32 GHz. The dashed circle indicates the wavenumber of a defect with size $\xi = 100$ nm.

and Krivosik [47], in which the TMS linewidth ΔH_{TMS} is given by [59, 60]

$$\Delta H_{TMS} = \frac{\gamma^2 \xi^2 H'^2}{df/dH|_{f_{FMR}}} \int \Gamma_{0\mathbf{q}} C_{\mathbf{q}}(\xi) \delta_\alpha(\omega - \omega_{\mathbf{q}}) d^2q, \tag{2.3}$$

where $\Gamma_{0\mathbf{q}}$ is the defect-mediated interaction term between magnons at wavevector 0 and $\mathbf{q}$, $C_{\mathbf{q}}(\xi) = (1 + (q\xi)^2)^{-3/2}$ is the correlation function of the magnetic system with correlation length ξ, and H' is the magnitude of the characteristic inhomogeneity (units of magnetic field). The δ_α-function in Eq. 2.3 selects only the magnon scattering channels that conserve energy. In the limit of zero intrinsic damping, it is identical to the Dirac delta function, but for finite α it is replaced by a Lorentzian function of width $\delta\omega = (2\alpha\omega/\gamma)d\omega/dH$. The magnon dispersion relation determining $\omega_{\mathbf{q}}$ is the usual Damon-Eshbach thin film result [59, 61] with the addition of magnetocrystalline anisotropy stiffness field terms extracted from the dependence of the resonance field on the applied frequency for the IP configuration. The film thickness d affects the states available for two-magnon scattering through the dispersion relation, namely, the linear term which gives rise to negative group velocity for small q ($\propto -qd$). The IP FMR linewidth data shown in Fig. 2.4 were fit to Eq. 2.1 (with Eq. 2.3 used to evaluate ΔH_{TMS}) with ξ, α, and H' as fitting parameters (shown in Table 2.3). The correlation length ξ remains approximately constant for different in-plane directions, while the strength H' is larger for the $\langle 100 \rangle$ directions in the CMA and CFA samples and the $\langle 110 \rangle$ directions in the CMS sample. Some degree of uncertainty results from this fitting procedure, because for linewidth data collected over a limited frequency range, ξ and α are not completely decoupled as fitting parameters. In absolute terms, however, the largest systematic errors come from the exchange stiffness, which is not well-known. The error bars given in Table 2.3 were calculated by varying the exchange stiffness over the range 400 meV Å^2 to 800 meV Å^2, and recording the change in the fit parameters. This range of values was chosen based on previous Brillouin light scattering measurements of the exchange stiffness in similar Heusler compounds [62, 63]. In addition, we note that in Eq. 2.1 ΔH_0 is taken to be isotropic, with the value given by the PP linewidth measurements shown in Fig. 2.2. Although certain realizations of inhomogeneity may result in an anisotropic ΔH_0 (see Ref. [49] for a good discussion), doing so here would only serve to create an additional fitting parameter.

2.4.4 Effect of low intrinsic damping

The effect of low intrinsic damping on the two-magnon linewidth can be seen in Fig. 2.5(a). As α decreases, with all other parameters fixed, ΔH_{TMS} steadily increases and becomes increasingly nonlinear (and eventually nonmonotonic) with frequency. In particular, a "knee" in the frequency dependence becomes more pronounced for low damping (see e.g. Fig. 2.5(a) curve for $\alpha = 10^{-4}$). The physics giving rise to the knee behavior is illustrated in Fig. 2.5(b). The TMS process scatters magnons from zero to non-zero wavevector at small q. There is assumed to be sufficient disorder to allow for the momentum q to be transferred to the magnon system. There will always be, however, a length scale ξ below which the disorder decreases, so that the film becomes effectively more uniform at large wavevectors. The corresponding FMR frequencies are those for which the contours of constant frequency (the figure eights in Fig. 2.5) in q-space have extrema at $q \sim \xi^{-1}$. The TMS rate is also determined by the interplay of the magnon density of states, the effective area in q-space occupied by the modes that conserve energy, and the Gilbert damping. The knee behavior is more pronounced for low α due to the increased weight of the van Hove singularity coming from the tips of the figure eights, in the integrand of Eq. 2.3. Although a larger window of energies, set by the width of δ_α, is available for larger α, this smears out the singularity in the magnon density of states, removing the sharp knee in the TMS linewidth as a function of frequency. The PP measurement confirms that all of these epitaxial Heusler films lie within the range $\alpha < 2 \times 10^{-3}$. Ferromagnetic films with ultralow α are therefore increasingly prone to large TMS linewidths (particularly for metals with large M_s). The TMS linewidths will also constitute a larger fraction of the total linewidth due to a smaller contribution from the Gilbert damping. In practice, this is why experimental reports [35, 55, 56] of ultralow α have almost all utilized the PP geometry.

2.4.5 Discussion

The results of the IP linewidth fits to Eqs. 2.1 and 2.3 are summarized in Table 2.3. In the case of CMS, the high-frequency slopes in Fig. 2.4(a) approach the same value along each direction, as would be expected when the frequency is large enough for the TMS wavevector to exceed the inverse of any defect correlation length. In this limit, α

Table 2.3: Summary of the fitting parameters used to fit the in-plane data of Fig. 2.4 (black squares and red circles) to Eqs. 2.1 and 2.3. CFA refers to the unannealed Co_2FeAl sample.

Sample (Field Direction)	α ($\times 10^{-3}$)	ξ (nm)	H' (Oe)
CMS$\langle 110 \rangle$	1.6 ± 0.2	40 ± 25	55 ± 30
CMS$\langle 100 \rangle$	1.5 ± 0.1	40 ± 25	30 ± 15
CMA$\langle 110 \rangle$	3.1 ± 0.2	70 ± 20	30 ± 5
CMA$\langle 100 \rangle$	4.7 ± 0.4	55 ± 10	90 ± 5
CFA$\langle 110 \rangle$	2.0 ± 0.3	20 ± 10	175 ± 60
CFA$\langle 100 \rangle$	N/A	N/A	N/A

is isotropic (within error limits).

Next, we discuss the CMA IP data shown in Fig. 2.4(b) and Table 2.3. It is clear from this figure that a good fit can be obtained along both $\langle 100 \rangle$ and $\langle 110 \rangle$ directions. In Table 2.3 it can be seen that the value of the defect correlation length ξ is approximately the same along both directions. However, the values of α we obtain from fitting to Eqs. 2.1 and 2.3 do not agree well with the PP value of $\alpha_{001} = 1.8 \times 10^{-3}$ (Fig. 2.2). Anisotropic values of α have been both predicted [32, 33] and observed [64], and an anisotropic α is possibly the explanation of our best-fit results. The in-plane $\langle 100 \rangle$ and [001] directions are equivalent in the bulk, so the anisotropy would necessarily be due to an interface anisotropy energy [64] or perhaps a tetragonal distortion due to strain [65].

Finally, we discuss the CFA linewidths shown in Fig. 2.4(c) and Table 2.3. This sample has by far the largest two-magnon scattering contribution, which is likely related to the anomalously large inhomogeneous broadening and low intrinsic damping [see Fig. 2.5(a)] observed in the PP measurement. A good fit of the data was obtained when the field was applied along the $\langle 110 \rangle$ direction. Notably, the IP $\langle 110 \rangle$ best fit value of 2.1×10^{-3} is nearly a factor of 3 larger than the α_{001} upper bound on the same sample (Table 2.1), strongly suggesting an anisotropic Gilbert α. A striking anisotropy in the IP linewidth was revealed upon rotating the magnetization to the $\langle 100 \rangle$ orientation. For the $\langle 100 \rangle$ case, which yielded the largest TMS linewidths measured in this family of films, we were not able to fit the data to Eq. 2.3 using a set of physically reasonable input parameters. We believe that this is related to the consideration that higher order terms

in the inhomogeneous magnetic energy (see Ref. [59]) need to be taken into account. Another reason why this may be the case is that the model of McMichael and Krivosik [47] assumes the inhomogeneities to be grain-like, whereas the samples are epitaxial [see Fig. 2.1(a)]. Atomic force microscopy images of these samples [Fig. 2.1(d)] imply that grains, if they exist, are much larger than the defect correlation lengths listed in Table 2.3, which are of order 10's of nm. We also note that there does not appear to be a correlation between the strength of two-magnon scattering H' and the cubic anisotropy field $2K_1/M_s$, which would be expected for grain-induced two-magnon scattering.

2.5 Summary and Conclusion

We conclude by discussing the successes and limitations of the McMichael and Krivosik [47] model in analyzing our epitaxial Heusler film FMR linewidth data. We have shown that two-magnon scattering is the extrinsic linewidth-broadening mechanism in our samples. Any model which takes this as its starting point will predict much of the qualitative behavior we observe, such as the knee in the frequency dependence and the large linewidths IP for low α films. The TMS model used in this article (for the purpose of separating TMS and Gilbert linewidth contributions) is, however, only as accurate as its representation of the inhomogeneous magnetic field and the underlying assumption for the functional form of $C_{\mathbf{q}}(\xi)$. Grain-like defects are assumed, which essentially give a random magnetocrystalline anisotropy field. We did not, however, explicitly observe grains in our samples with AFM, at least below lengthscales of $\sim$10 μm [Fig. 2.1(d)]. Misfit dislocations, a much more likely candidate in our opinion, would cause an effective inhomogeneous magnetic field which could have a more complicated spatial profile and therefore lead to anisotropic two-magnon scattering (see Ref. [49]). The perturbative nature of the model also brings its own limitations, and we believe that the CFA$\langle 100 \rangle$ data, for which we cannot obtain a satisfactory fit, are exemplary of a breakdown in the model for strong TMS. Future work should go into methods of treating the two-magnon scattering differently based on the type of crystalline defects present, which will in turn allow for a more reliable extraction of the Gilbert damping α and facilitate the observation of anisotropic Gilbert damping, enabling quantitative comparison to first-principles calculations.

Regardless of the limitations of the model, we emphasize three critical observations drawn from the linewidth measurements presented in this chapter. First, in all cases we observe large and anisotropic TMS linewidth contributions, which imply inhomogeneity correlation lengthscales of order tens-to-hundreds of nanometers. The microscopic origin of these inhomogeneities is the subject of ongoing work, but are likely caused by arrays of misfit dislocations [49]. The relatively large lengthscale of these defects may cause them to be easily overlooked in epitaxial film characterization techniques such as XRD and cross-sectional HAADF-STEM, but they still strongly influence magnetization dynamics. These defects and their influence on the FMR linewidth through TMS complicate direct observation of Kamberský's model for anisotropic and (in the case of Heusler compounds) ultralow intrinsic damping in metallic ferromagnets. Second, we observed low intrinsic damping through our PP measurement, which was $< 2 \times 10^{-3}$ for all of our samples. Finally, we have presented the mechanism by which FMR linewidths in ultralow damping films are particularly likely to be enhanced by TMS, the anisotropy of which may dominate any underlying anisotropic Kamberský damping.

Chapter 3

Two-Magnon Scattering: Frequency Pulling

3.1 Introduction

Magnetization dynamics of ferromagnets are influenced by many factors, such as magnetocrystalline anisotropy, interfacial anisotropy, and Gilbert damping. It is of technological interest to study these phenomena in order to understand, for example, the physics governing magnetization switching by spin torque [44, 66, 67]. Interfacial anisotropies are particularly relevant for these applications, where materials with perpendicular anisotropy are sought due to the lower energy cost associated with switching of the magnetization [68]. Anisotropy arising from broken symmetry at the interfaces in ultrathin magnetic films is commonly probed using ferromagnetic resonance (FMR) techniques [64, 69], usually by measuring the FMR fields as a function of driving frequency or applied field orientation.

Two-magnon scattering (TMS), an extrinsic relaxation process of uniform magnetization precession in ferromagnets, is an important phenomenon that influences magnetization dynamics. TMS is commonly observed as a broadening of FMR lineshapes, but it may also lead to a shift in the FMR frequency [46, 47, 59]. Although the broadening of the FMR lineshape caused by TMS is often impossible to ignore, the latter effect is more subtle and almost universally neglected when FMR data are used to extract static magnetic properties of materials. Failure to properly account for this effect, however,

may lead to inaccurate estimates of magnetic anisotropy energies, potentially leading to the inference of a substantial interface anisotropy where there is none.

In this chapter, we demonstrate the existence of a frequency-pulling effect in ferromagnetic resonance induced by two-magnon scattering in polycrystalline $Fe_{0.7}Ga_{0.3}$ thin films for in-plane applied magnetic fields.[1] We arrive at this result by calculating the frequency shift based on our analysis of the linewidth broadening caused by two-magnon scattering (which is a large effect and is easier to observe). This is possible due to the complementary nature of the two phenomena. We show that the observed resonance frequencies are only consistent with the data taken for perpendicular-to-plane fields (i.e., can be fit using the same perpendicular anisotropy field) when they are adjusted to account for the two-magnon frequency shifts. We conclude by demonstrating this effect in additional samples of different thicknesses, simultaneously showing that the magnitude of the frequency shifts scales with the magnitude of the two-magnon linewidths as the theory predicts. These results were published in *Applied Physics Letters* (see Ref. [70]).

3.2 Samples: Growth & Characterization

The samples used in this report are 17 nm, 26 nm, and 33 nm $Fe_{0.7}Ga_{0.3}$ films (thicknesses determined by x-ray reflectivity). The 33 nm films were deposited on Si/SiO_2 substrates at room temperature by dc magnetron sputtering of an $Fe_{0.7}Ga_{0.3}$ target. The base pressure of the deposition chamber was 5×10^{-8} torr and the working pressure was maintained at 5×10^{-3} torr by Ar gas (99.999%). The composition of the $Fe_{0.7}Ga_{0.3}$ films was quantitatively analyzed by energy dispersive spectroscopy (EDS). The 17 nm and 26 nm films were obtained by etching the 33 nm films with an ion mill. The lack of magnetic anisotropy in the plane of the film was verified with vibrating sample magnetometry (VSM) and FMR for the 33 nm film. Grain boundaries were observed with atomic force microscopy (AFM), yielding an average grain diameter of $\sim$15 nm [see Fig. 3.1(a)]. This is in good agreement with the structural coherence length, which was estimated to be 13 nm with XRD. Figure 3.1(b) shows a two-dimensional XRD detector image of the $Fe_{0.7}Ga_{0.3}$ (110) peak for the 33 nm film, where the center of the

[1] The $Fe_{0.7}Ga_{0.3}$ films are desirable for this study due to their polycrystallinity (isotropy)—this eliminates the possibility of magnetocrystalline anisotropy. Absence of magnetocrystalline anisotropy makes it more straightforward to detect the influence of TMS on the FMR frequency.

detector coincides with a scattering vector normal to the film plane. The intensity of this Bragg peak is approximately constant for fixed values of the scattering angle 2θ as the scattering vector is canted into the plane [as evidenced by the "ring" in Fig. 3.1(b)], indicating the absence of texture.

3.3 Experiment & Results

Ferromagnetic resonance lineshapes were measured at room temperature using a coplanar waveguide with modulation of the applied magnetic field for lock-in detection as described in Chapter 2. The coplanar waveguide was placed in series with a rectifying diode that measured the transmitted microwave power. The applied dc magnetic field was modulated with a 220 Hz ac magnetic field having an amplitude of a few Oe for lock-in detection of the differential absorption. The microwave frequency was varied up to 52 GHz with power from 5 to 10 dBm. The lineshapes were measured for both in-plane (IP) and perpendicular-to-plane (PP) applied fields. When the magnetization is IP, there exist magnons degenerate with the $\mathbf{q} = 0$ FMR magnon [see Fig. 3.1(c)]. This leads to a possible scattering mechanism of the FMR mode, observable through its nonlinear effect on the field-swept linewidth as a function of frequency [46, 47, 59], shown in Fig. 3.1(d) for the 33 nm $Fe_{0.7}Ga_{0.3}$ film. This is the TMS process, and it is allowed as long as some assisting process enables conservation of momentum.

The resonance frequency was fit as a function of the applied magnetic field H_0 to the Kittel equation for a thin film with no in-plane magnetic anisotropy, which reads as

$$\omega_{FMR} = \gamma\sqrt{H_0(H_0 + 4\pi M_{eff})} \tag{3.1}$$

for H_0 in the plane and

$$\omega_{FMR} = \gamma(H_0 - 4\pi M_{eff}) \tag{3.2}$$

for H_0 perpendicular to the plane [71], with γ the gyromagnetic ratio and $4\pi M_{eff}$ the effective demagnetizing field. Henceforward we will express the gyromagnetic ratio in terms of the Landé g-factor, *via* $\gamma = g\frac{\mu_B}{\hbar}$. Figure 3.2 shows field-dependent resonance dispersions of the 33 nm film for IP and PP applied fields, along with fits to Eqs. (3.1) and (3.2). For the PP case we obtain $g = 2.0564 \pm 0.0007$ and $4\pi M_{eff} = 13.821 \pm 0.004$ kOe, and for the IP case $g = 2.14 \pm 0.01$ and $4\pi M_{eff} = 11.7 \pm 0.2$ kOe. The

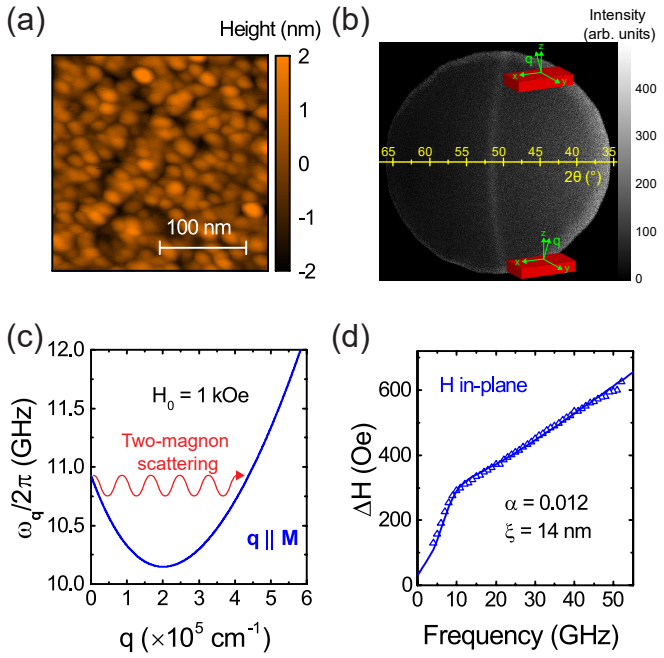

Figure 3.1: (a) Atomic force microscopy image of the 33 nm $Fe_{0.7}Ga_{0.3}$ film. Root-mean-square roughness is 0.7 nm. (b) Two-dimensional XRD detector image of the 33 nm $Fe_{0.7}Ga_{0.3}$ film showing the (110) Bragg peak (given by the "ring" at $2\theta \simeq 52°$). The center of the detector corresponds to the symmetric configuration, in which the scattering vector $\mathbf{q}$ is normal to the plane of the film ($q_x = q_y = 0$). The scattering vector is canted into the film plane as one moves vertically from the center of the detector, as indicated by the coordinate axes. The structural coherence length determined from the full-width-at-half-maximum of the Bragg peak is 13 nm. (c) Thin-film magnon dispersion for in-plane magnetization and wavevectors $\mathbf{q} \parallel \mathbf{M}$, with an arrow indicating the two-magnon scattering process. (d) Field-swept FMR linewidths of the 33 nm $Fe_{0.7}Ga_{0.3}$ film with in-plane applied magnetic field overlaid with a fit to a combined two-magnon scattering and Gilbert damping model. The Gilbert damping α (a fit parameter) and defect correlation length ξ (fixed) are shown on the figure.

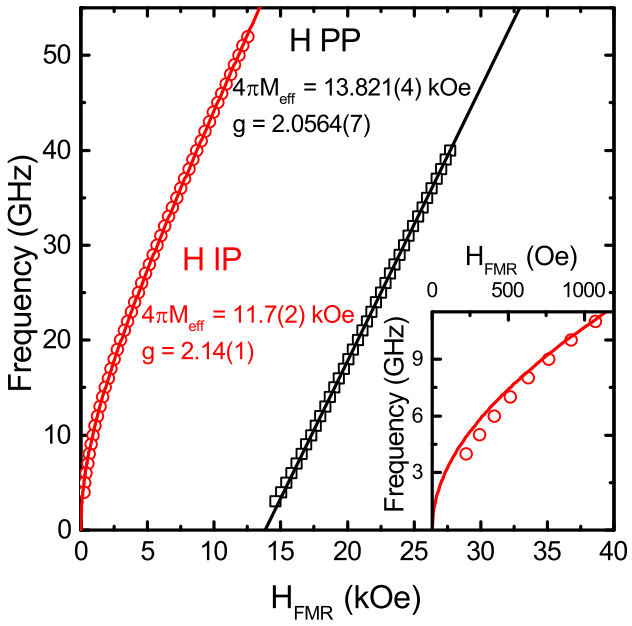

Figure 3.2: Frequency as a function of resonance field for the 33 nm film obtained with IP (red circles) and PP (black squares) orientations of the magnetic field, overlaid with fits to Eqs. (3.1) and (3.2), respectively. Fit parameters $4\pi M_{eff}$ and g-factor are indicated on the figure for both cases. Inset shows a close-up of the IP orientation at low frequencies.

PP value of $4\pi M_{eff} = 13.821$ kOe is higher than previous bulk measurements [2] but is similar to values obtained in thin films [72]. The inset shows a close-up of the IP data at low frequencies, from whence it is clear that a discrepancy exists between the IP data and the fit to Eq. (3.1). For the 26 nm and 17 nm thicknesses we observe the same qualitative behavior. In the case of the 26 nm film we measure $4\pi M_{eff} = 14.0736 \pm 0.0006$ kOe and $g = 2.060 \pm 0.001$ for PP fields, compared to $4\pi M_{eff} = 12.17 \pm 0.01$ kOe and $g = 2.133 \pm 0.007$ for IP fields. For the 17 nm film we measure $4\pi M_{eff} = 13.0049 \pm 0.0005$ kOe and $g = 2.054 \pm 0.001$ for PP fields, compared to $4\pi M_{eff} = 11.623 \pm 0.006$ kOe and $g = 2.120 \pm 0.004$ for IP fields. In addition, the IP data for both the 17 nm and 26 nm films cannot be fit well to Eq. (3.1) at low fields (similar to what is seen for the 33 nm film, shown in the inset of Fig. 3.2). There is no in-plane magnetic anisotropy, so the discrepancy cannot be attributed to an in-plane anisotropy field. Furthermore, the parameters yielded by the fits in either case are drastically different. In light of these inconsistencies, we proceed to investigate the effect of TMS on the IP field-dependent resonance dispersion.

3.4 Theory of TMS Line Shifts

One of the primary characteristics of TMS is that it can be suppressed by orienting the magnetization perpendicular-to-plane, a result of the disappearance of degeneracies in the spin wave dispersion as the magnetization is rotated perpendicular to the plane [73]. Later this fact will be used to control for TMS, allowing the observation of the noninteracting or "bare" properties when the film is perpendicularly magnetized.

The breaking of momentum conservation in TMS necessitates the presence of defects in order to drive the process. There are numerous categories of defects which may cause TMS. Among the prominent ones are surface roughness [46, 74], dislocation networks [49], and grain boundaries [47, 59]. We will focus here on TMS induced by grain boundaries, having confirmed the structural isotropy of the films with XRD as well as observing grains directly with AFM. These characterization data also allow us to constrain the defect lengthscale, which partially determines the strength of coupling between $\mathbf{q} = 0$ and $\mathbf{q} \neq 0$ magnons. In the context of TMS, the grains lead to a spatially inhomogeneous and random anisotropy field. The inhomogeneous field allows

for interaction between the FMR mode and modes at nonzero wavevector, providing both an additional relaxation channel and a change in the effective stiffness of the FMR mode. These can be described as imaginary and real shifts in the FMR frequency, respectively. A perturbative model of TMS for this system gives the following result for the complex frequency shift of the FMR mode due to interactions with modes at nonzero wavevector [47, 59, 60]:

$$\Delta\omega_{TMS} = \gamma^2\xi^2 H'^2 \int d^2\mathbf{q}\ \Lambda_{0\mathbf{q}} \frac{1}{(1+(q\xi)^2)^{3/2}} \frac{1}{\pi} \frac{1}{(\omega-\omega_{FMR})-i\delta\omega} \tag{3.3}$$

where H' is the root-mean-square inhomogeneity field, ξ is the defect correlation length, $\Lambda_{0\mathbf{q}}$ is the magnon-magnon coupling strength (see Ref. [60]), and $\delta\omega = (d\omega/dH|_{H_{FMR}})\frac{\alpha\omega}{\gamma}$ is the Gilbert frequency half-width-at-half-maximum linewidth. The imaginary part of Eq. (3.3) corresponds to the well-known TMS contribution to the FMR scattering rate, i. e. linewidth. Lesser known, however, is the real part, which describes a shift of the FMR frequency due to TMS. This effect has been previously reported in ultrathin films of $Ni_{0.5}Fe_{0.5}$ [75], but a lack of broadband measurements leaves the results open to interpretation (such as the possibility of it having arisen from interface anisotropy). In addition, the strength of two-magnon scattering in our system is much greater.

3.5 Analysis & Discussion

We begin our analysis by fitting the field-swept linewidths to the imaginary part of Eq. (3.3), including contributions from Gilbert damping (linear with frequency) and inhomogeneous broadening (constant with frequency, determined from the PP measurement). We hold the defect correlation length ξ fixed to 14 nm based on the structural characterization described earlier. The fit parameters are α and H', which we use to calculate the FMR frequency shifts from the real part of Eq. (3.3). Notably, the Gilbert damping α determines both the Gilbert linewidth *and* the two-magnon linewidth—the latter is clear upon inspection of Eq. (3.3) and is discussed at length in Chapter 2.

The fractional FMR frequency shifts for the 17 nm, 26 nm, and 33 nm films are shown in Fig. 3.3. The solid curves give the predicted fractional frequency shifts based on the fits of the linewidths. The points in Fig. 3.3 represent the observed fractional frequency shifts, determined by taking the difference between the observed FMR frequencies and

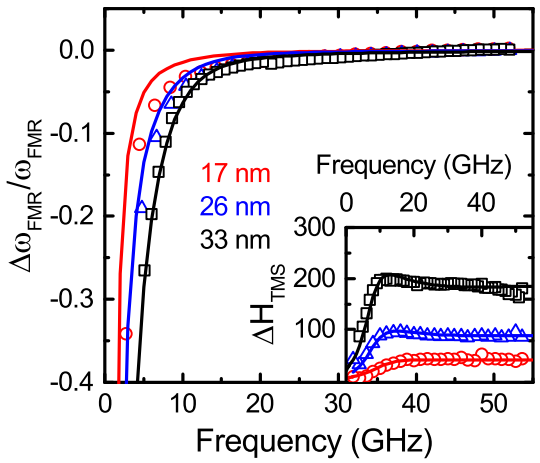

Figure 3.3: Frequency shifts induced by two-magnon scattering for the 17 nm (red points), 26 nm (blue points), and 33 nm (black points) $Fe_{0.7}Ga_{0.3}$ films. The predicted frequency shifts given by the solid curves are calculated from the real part of Eq. (3.3) using the fit parameters from the fits of the linewidths. Inset shows the two-magnon linewidths for the three films along with fits to the imaginary part of Eq. (3.3). The two-magnon linewidths are determined by subtracting the Gilbert damping and inhomogeneous linewidths (the inhomogeneous linewidths are determined from the PP measurement).

the FMR frequencies predicted by Eq. (3.1) (taking $4\pi M_{eff}$ from the PP measurement). The strong frequency-pulling effect of TMS is evident from the main panel of Fig. 3.3, with red shifts approaching 1 GHz at low frequencies.

The two-magnon linewidths for the three films are shown in the inset. The solid curves give the fits to the imaginary part of Eq. (3.3), while the points are obtained by taking the observed linewidths and subtracting both the Gilbert and inhomogeneous broadening (taken from the PP measurement) contributions. A notable observation from Fig. 3.3 is the correlation between the magnitudes of the two-magnon linewidths and frequency shifts for the three films, which is a prediction of Eq. 3.3.

We now discuss how the aforementioned inconsistency between IP and PP field-dependent resonance dispersions, and the inability to obtain a good fit of the IP data to Eq. (3.1), can be explained by the frequency-pulling effect of TMS. The absence of TMS for PP magnetization is of particular convenience in our case because it allows determination of the effective demagnetizing field $4\pi M_{eff}$ and the Landé g-factor, which

together can in principle be used to predict the FMR field-dependent dispersion for IP magnetization. A direct measurement of the dispersion for IP magnetization is not possible due to the frequency shifts caused by TMS. To address this problem, the IP FMR frequencies are blue-shifted using the red curve shown in Fig. 3.3, representing the FMR frequencies in the absence of TMS. We then fit the corrected IP FMR frequencies to Eq. (3.1), fixing $4\pi M_{eff}$ to the PP value of 13.821 kOe (for the 33 nm film) and leaving the g-factor as a free parameter. (A small amount of surface anisotropy may be produced by an anisotropy of the orbital moment of the film, leading to an anisotropic g-factor [71].) The shifted IP FMR frequencies at low fields, along with a fit to Eq. (3.1) for fixed $4\pi M_{eff}$, are shown in Fig. 3.4 for the 33 nm film—these values represent the bare FMR frequencies in the absence of two-magnon scattering. The fit yields $g = 2.045 \pm 0.001$, which is less than 1% lower than the PP value of $g = 2.0564 \pm 0.0007$. Also shown are the FMR frequencies before being adjusted for two-magnon interactions (blue data points). The inset of Fig. 3.4 shows the bare FMR frequencies and fit up to high fields. This process was also carried out for the 26 nm and 17 nm films, whereby the agreement with Eq. (3.1) was significantly improved. The fits of the IP data to Eq. (3.1) yielded $g = 2.039 \pm 0.002$ for the 26 nm film and $g = 2.045 \pm 0.002$ for the 17 nm film (both $\lesssim 1\%$ lower than the PP values). It is clear from Fig. 3.4 that the frequency-pulling effect of TMS is successful at explaining the inconsistencies we have encountered.

3.6 Conclusion

In conclusion, we observe a frequency-pulling effect of the ferromagnetic resonance in thin films of $Fe_{0.7}Ga_{0.3}$ for magnetization in the plane of the film. It is shown that this effect can be explained by the hybridization of the ferromagnetic resonance with nonuniform magnons as a result of the two-magnon scattering interaction. The frequency shifts can be predicted from the two-magnon induced broadening of the lineshapes, whereby a consistency is obtained with the lineshapes measured when the magnetization is perpendicular to the plane of the film. These results highlight the importance of accounting for two-magnon scattering when using ferromagnetic resonance as a characterization technique, a fact which is usually ignored in the determination of static properties.

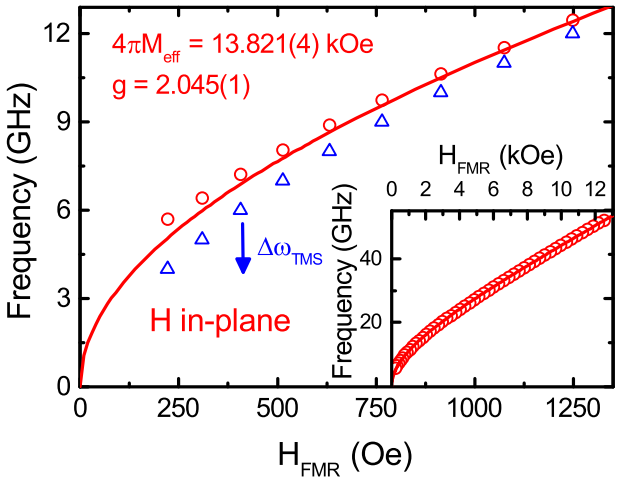

Figure 3.4: Ferromagnetic resonance frequencies of the 33 nm film at low fields for the IP configuration. The red data points are blue-shifted by amounts given by the red curve in Fig. 3.3, overlaid with a fit to Eq. (3.1). The effective demagnetizing field $4\pi M_{eff}$ is fixed to 13.821 kOe based on the fit to the PP data (black squares of Fig. 3.2); the only fit parameter is the Landé g-factor. The blue data points are the observed resonance frequencies, before two-magnon interactions are not taken into account. The inset shows all of the adjusted resonance frequencies up to high fields.

Chapter 4

Magnetoelastic Gilbert Damping

4.1 Introduction

Among the primary considerations in the design of spintronics devices is Gilbert damping. However, a full understanding of the mechanisms which cause damping of magnetization dynamics in ferromagnets remains elusive. Reports of anisotropy in the Gilbert damping have proven to be useful tools in the understanding of the underlying mechanisms involved [32, 64, 65], but there is much that is yet unclear. Studies of the temperature dependence also promise to be a uniquely powerful tool for a complete physical understanding [36, 54], however, there are few such reports in existence.

Recently, it has been shown that spins can be coherently coupled over large distances ($\sim$1 mm) using magnon-phonon coupling [76–78]. It is also well known that magnetization dynamics can be excited elastically through this phenomenon [79], but its effect on Gilbert damping has been largely confined to theoretical calculations [80–83] and lacks clear experimental validation. Furthermore, most studies have focused on yttrium iron garnet (YIG), which is weakly magnetostrictive.

In this chapter, we demonstrate a large and anisotropic magnetoelastic contribution to the Gilbert damping in highly magnetostrictive $Fe_{0.7}Ga_{0.3}$ films through broadband measurements of the ferromagnetic resonance (FMR) linewidths over a wide range of temperatures. The perpendicular-to-plane linewidths exhibit a relatively low minimum in the Gilbert damping of approximately 0.004, similar to that of bcc Fe [35]. At room

temperature, the Gilbert damping is as large as a factor of 10 greater with field applied in plane relative to out of plane. In fact, for any given sample and temperature, the anisotropy is, at minimum, about a factor of 2. We argue this is due to a mitigation of the magnetoelastic contribution for perpendicular magnetization, arising from finite-thickness boundary conditions and weak elastic coupling to the substrate. The nonmonotonic temperature dependence of the Gilbert damping also shows the competing effects of the magnetostriction, which increases at low temperature, and the phonon viscosity, which generally decreases at low temperature. The results contained in this chapter have been published in *Physical Review B* (see Ref. [84]).

4.2 Sample Growth and Measurement Technique

The $Fe_{0.7}Ga_{0.3}$ films studied in this chapter were deposited on SiO_2/Si wafers at room temperature by dc magnetron sputtering of an $Fe_{0.7}Ga_{0.3}$ target. The base pressure of the deposition chamber was 5×10^{-8} torr, and the working pressure was kept at 5×10^{-3} torr with Ar gas. The composition of the $Fe_{0.7}Ga_{0.3}$ films was quantitatively analyzed by energy dispersive spectroscopy (EDS). Films were grown with thicknesses of 21 nm, 33 nm, 57 nm, and 70 nm (the 21 nm, 57 nm, and 70 nm belong to the same growth series). An additional 33 nm film was grown at 200 °C. The 33 nm room temperature deposition was etched using an ion mill to obtain films with thicknesses of 17 nm and 26 nm. The thicknesses of the films were measured using x-ray reflectivity (see Fig. 4.1 for reflectivity of select films).

The FMR linewidths were measured using a setup involving a coplanar waveguide and modulation of the applied magnetic field for lock-in detection as described in Ch. 1 and Ref. [52]. Measurements were done with the field applied in the plane (IP) and perpendicular to the plane (PP) of the film. The sample temperature was varied from 5 K to 400 K for both IP and PP configurations with microwave excitation frequencies up to 52 GHz. The measurement probe was designed by NanOsc for a Quantum Design Physical Property Measurement System (PPMS). The resonance fields and linewidths were isotropic in the plane, and the absence of in-plane magnetic anisotropy—with the exception of the 70 nm film, where a small uniaxial anisotropy was observed—was verified with vibrating sample magnetometry (shown in Fig. 4.2 for select films). We

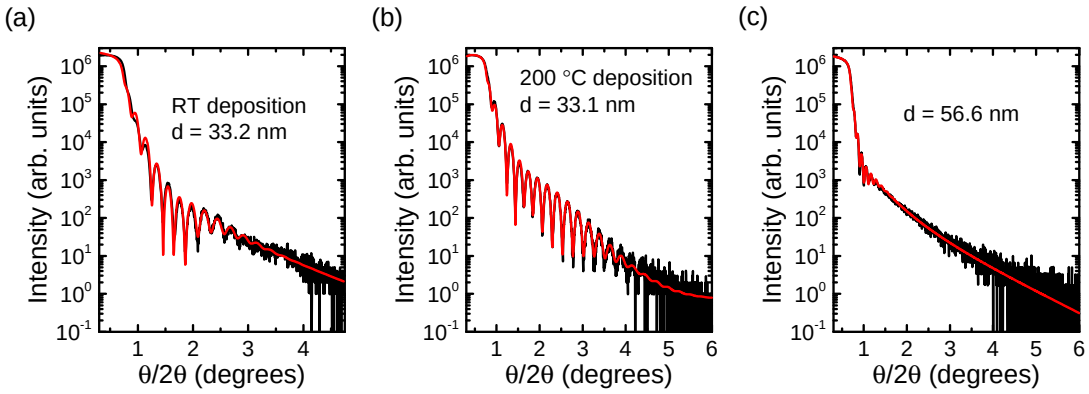

Figure 4.1: X-ray reflectivity data (black) overlaid with fits (red) for the (a) 33 nm (room temperature deposition), (b) 33 nm (200 °C deposition), and (c) 57 nm films. Thicknesses d obtained from the fits are indicated on the figure.

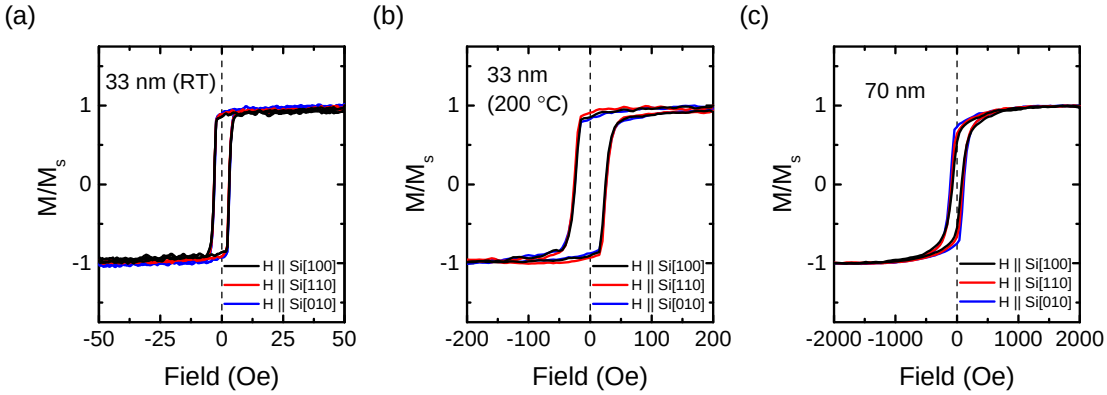

Figure 4.2: Vibrating sample magnetometry of (a) 33 nm (room temperature deposition), (b) 33 nm (200 °C deposition), and (c) 70 nm films for $H \parallel$ Si[100] (black), $H \parallel$ Si[110] (red), and $H \parallel$ Si[010] (blue).

place an upper bound of $\simeq 125$ Oe on the anisotropy field of the 70 nm based on the angular dependence of the FMR fields, which is about a factor of 10 smaller than the linewidths and has no impact on our main conclusions. The absence of anisotropy in the other samples is also consistent with the abundance of grain boundaries observed with atomic force microscopy (AFM).

4.3 Results, Initial Analysis, & Data Anomalies

In analyzing the FMR linewidths, we consider three contributions: Gilbert damping $4\pi\alpha f/\gamma$ (α is the Gilbert damping coefficient, f is the microwave frequency, and γ is the gyromagnetic ratio), inhomogeneous broadening ΔH_0, and two-magnon scattering ΔH_{TMS} (for IP fields). Eddy current damping and radiative damping contributions [48] are neglected because we expect them to be small ($< 10^{-4}$) for these films. Linewidths of the 70 nm film at 300 K for both configurations of the applied field are shown in Fig. 4.5(a), and the IP linewidths with individual contributions to the linewidth plotted separately in Fig. 4.5(b). We fit the IP linewidths using a model of two-magnon scattering based on granular defects [47, 52, 59]. The fit for the 70 nm film is shown in Fig. 4.5(b), along with the two-magnon contribution alone given by the magenta curve. The fit parameters are the Gilbert damping α (indicated in the figure) and the RMS inhomogeneity field H'. The defect correlation length ξ is fixed to 17 nm based on the structural coherence length obtained with x-ray diffraction (XRD) [Fig. 4.3(c)], which agrees well with the average grain diameter observed with AFM [Fig. 4.4(c)]. Furthermore, the high-frequency slope of the linewidths approaches that of the Gilbert damping since the two-magnon linewidth becomes constant at high frequencies [see Fig. 4.5(b)].

We now compare the IP and PP linewidths of the 70 nm film shown in Fig. 4.5(a). The two-magnon scattering mechanism is inactive with the magnetization perpendicular to the plane [46], and so the PP linewidths are fit linearly to extract the Gilbert damping. We obtain a value of 0.0035 ± 0.0001 for PP fields and 0.039 ± 0.0005 for IP fields, corresponding to an anisotropy larger than a factor of 10. Li *et al.* [65] recently reported a large anisotropy ($\sim$ factor of 4) in epitaxial $Co_{50}Fe_{50}$ thin films.

First we discuss the dependence of the PP Gilbert damping α_{PP} on temperature for

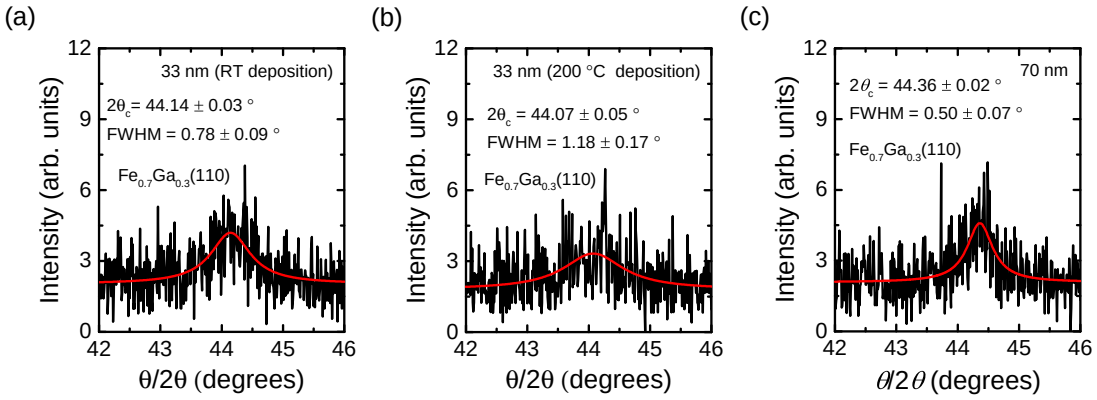

Figure 4.3: X-ray diffraction symmetric $\theta/2\theta$ scans for (a) 33 nm room temperature deposition, (b) 33 nm 200 °C deposition, and (c) 70 nm films. Full width at half maxima (FWHM) and 2θ center positions are indicated on the figure.

all of the films, shown in Fig. 4.6. We observe a significant temperature dependence in all cases (with the exception of the 33 nm room temperature deposition), characterized by a maximum at around 50 K. Then, at the lowest temperatures (5 to 10 K), α_{PP} approaches the same value for all of the films ($\simeq 0.004$).

Now we turn to the temperature dependence of the IP Gilbert damping α_{IP} shown in Fig. 4.9. The values here were obtained by fitting the linewidths linearly, but excluding the low-frequency points ($\lesssim 20$ GHz) since the two-magnon scattering becomes constant only at high frequencies [49]. Here we note, upon comparison with Fig. 4.6, that a large anisotropy of the Gilbert damping exists for all of the samples. In the 70 nm film, for instance, α_{IP} is more than a factor of 10 larger than α_{PP} at 300 K. In the temperature dependence of α_{IP}, we observe behavior which is similar to that seen in α_{PP} (Fig. 4.6), namely, a maximum at around 50 K (with the exception of the 21 nm film). Here, however, α_{IP} does not approach a common value at the lowest temperatures in all of the samples as it does in the PP case.

The IP Gilbert damping is larger than the PP Gilbert damping for all of the samples over the entire range of temperatures measured. This anisotropy of the Gilbert damping—along with the nonmonotonic temperature dependence—in all seven samples implies a contribution to the Gilbert damping in addition to Kamberský damping. We have verified that the orientation of FeGa(110) planes is completely random with XRD

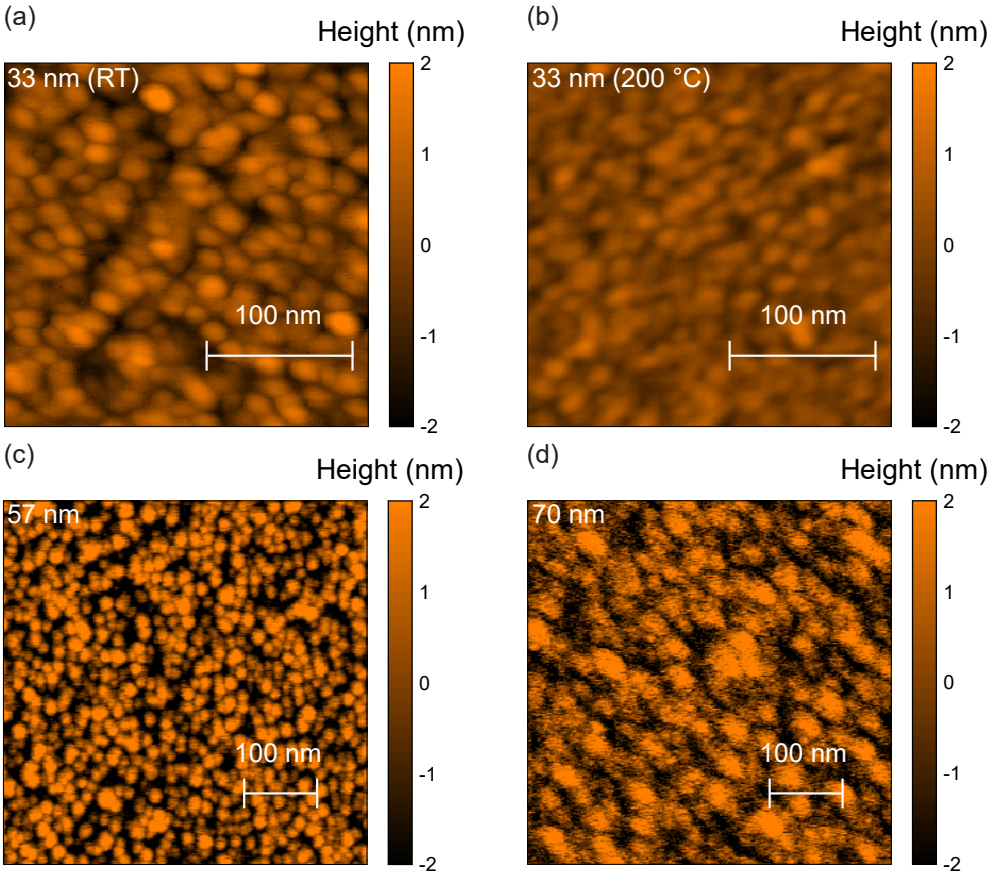

Figure 4.4: Atomic force micrographs for (a) 33 nm (room temperature deposition), (b) 33 nm (200 °C deposition), (c) 57 nm, and (d) 70 nm films. RMS roughnesses are (a) 0.7 nm, (b) 0.4 nm, (c) 1.5 nm, and (d) 1.3 nm.

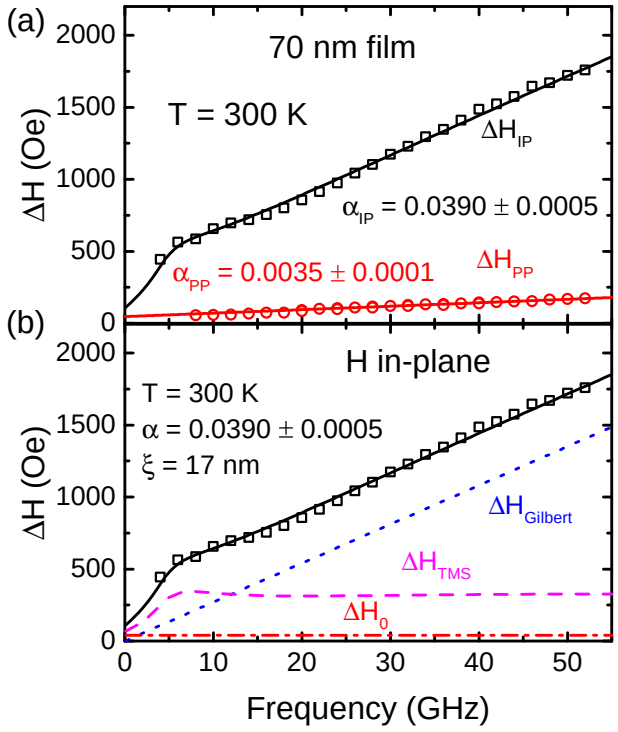

Figure 4.5: (a) FMR linewidths for IP (black squares) and PP (red circles) configurations for the 70 nm film. The IP linewidths are fit to a model of two-magnon scattering and the PP linewidths are fit using the standard Gilbert damping model. (b) Total linewidth (solid black), Gilbert linewidth (dotted blue), two-magnon scattering linewidth (dashed magenta), and inhomogeneous broadening (dashed/dotted red) for the 70 nm film with IP field.

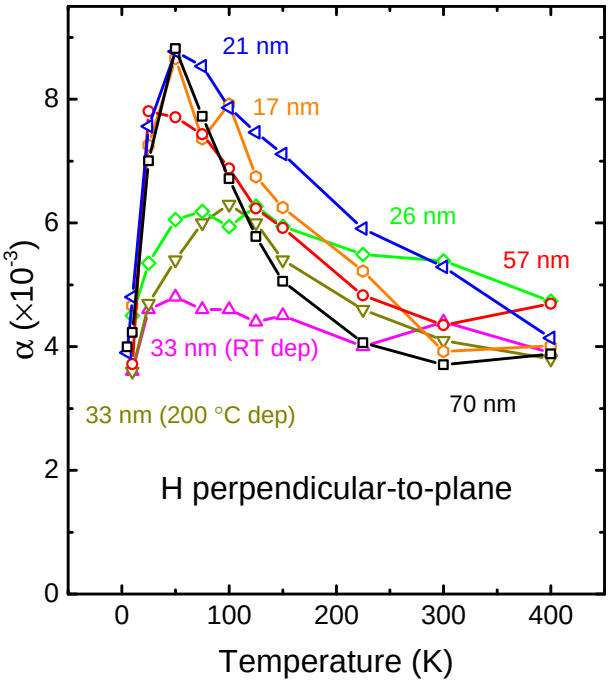

Figure 4.6: Gilbert damping α for PP field shown as a function of temperature for the 17 nm (orange), 21 nm (blue), 26 nm (green), 33 nm room temperature deposition (magenta), 33 nm 200 °C deposition (gold), 57 nm (red), and 70 nm (black) $Fe_{0.7}Ga_{0.3}$ films.

for the 33 nm (both depositions) and 70 nm films (see Fig. 4.7 for select films), and it is therefore not possible that the anisotropy is due to Kamberský damping. Interface anisotropy has reportedly led to anisotropic Kamberský damping in ultrathin (∼1 nm) films of Fe [64], but this is highly unlikely in our case due to the relatively large thicknesses of the films. In addition, the fact that the damping anisotropy shows no clear correlation with film thickness furthers the case that interface effects, which tend to show a larger anisotropy in thinner films [64], cannot be the cause. The longitudinal resistivity ρ_{xx} of the 33 nm (both depositions) and 70 nm films shows very weak temperature dependence(see Fig. 4.8). In the Kamberský model, the temperature dependence of the damping is primarily determined by the electron momentum relaxation time τ, and we would therefore not expect the Kamberský damping to show a significant temperature dependence for samples where the residual resistivity ratio is approximately unity. It is plausible that the Kamberský damping would still show a temperature dependence in situations where the spin polarization is a strong function of temperature, due to changes in the amount of interband spin-flip scattering (discussed in Chapter 1). This kind of damping, however, would be expected to decrease at low temperature [1, 31]. The temperature dependence we observe for both α_{PP} and α_{IP} is therefore inconsistent with Kamberský's model, and the similarity between the two cases in this regard suggests that the enhanced Gilbert damping has a common cause that is mitigated in the PP configuration.

4.4 Model of Magnetoelastic Damping

It has been proposed that magnetoelastic coupling can lead to Gilbert-like magnetization damping through phonon relaxation processes [25, 80, 82]. Similar treatments calculate the magnetoelastic energy loss through interaction with the thermal population of phonons [81, 85]. The Kamberský mechanism is often assumed to be the dominant Gilbert damping mechanism in metallic samples, so magnetoelastic Gilbert damping is usually studied in magnetic insulators, particularly yttrium iron garnet (YIG). There is the possibility, however, for the magnetoelastic damping to dominate in metallic samples where the magnetostriction is large, such as in Fe-Ga alloys. Later we will discuss how magnetoelastic damping can be mitigated in thin films by orienting the magnetization

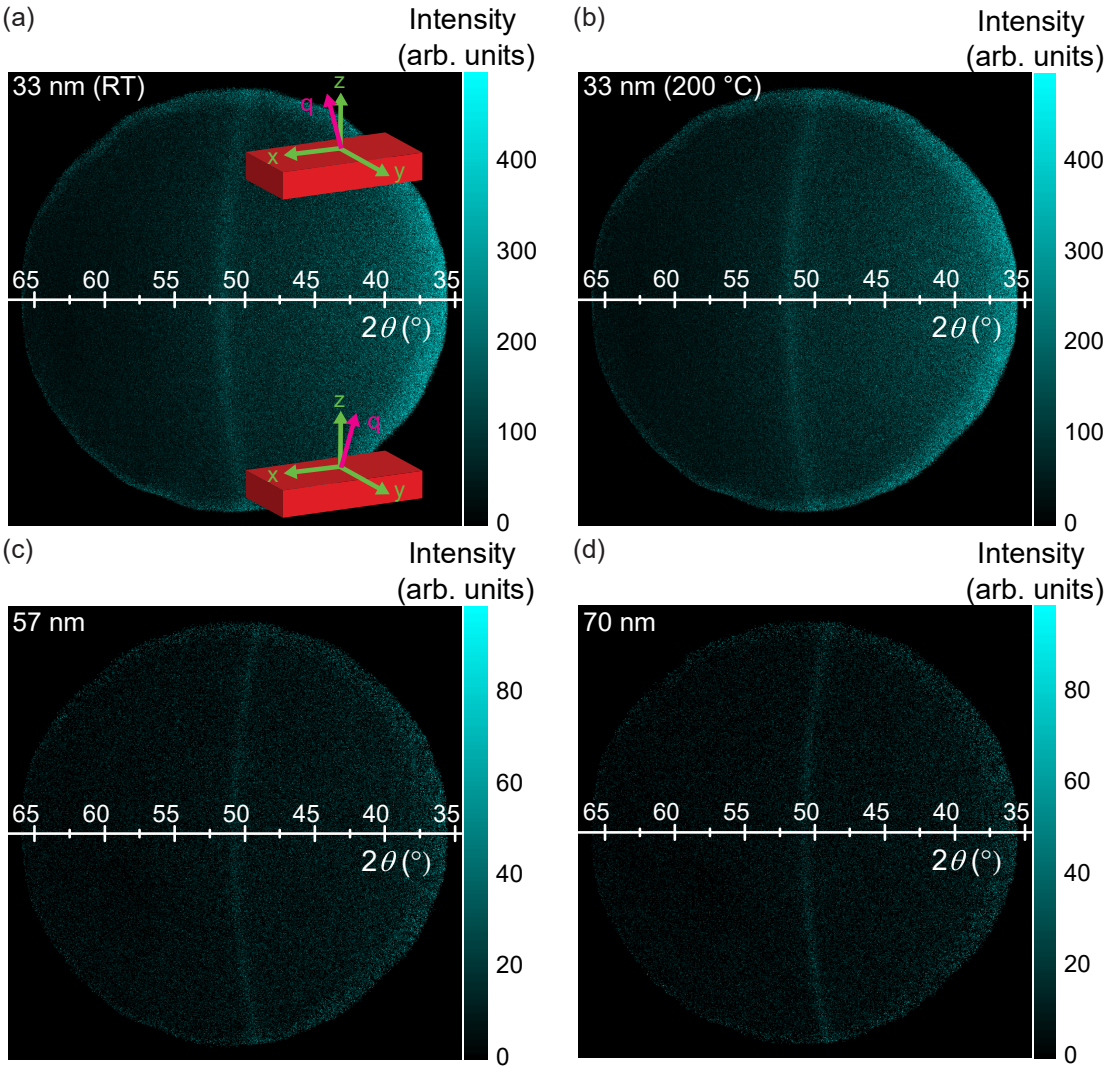

Figure 4.7: Two-dimensional detector images of the $Fe_{0.7}Ga_{0.3}(110)$ peak for (a) 33 nm (room temperature deposition), (b) 33 nm (200 °C deposition), (c) 57 nm, and (d) 70 nm films. The total scattering angle is 2θ and is shown on the abscissa. The measurement is conducted such that the symmetric configuration corresponds to the center of the detector, which is to say that the incident radiation is at an angle $\omega \simeq 26^\circ$ relative to the sample surface. In panel (a), the effect of moving vertically from the center of the detector on the scattering vector $\mathbf{q}$ is shown ($\mathbf{q}$ is canted into the y-z plane).

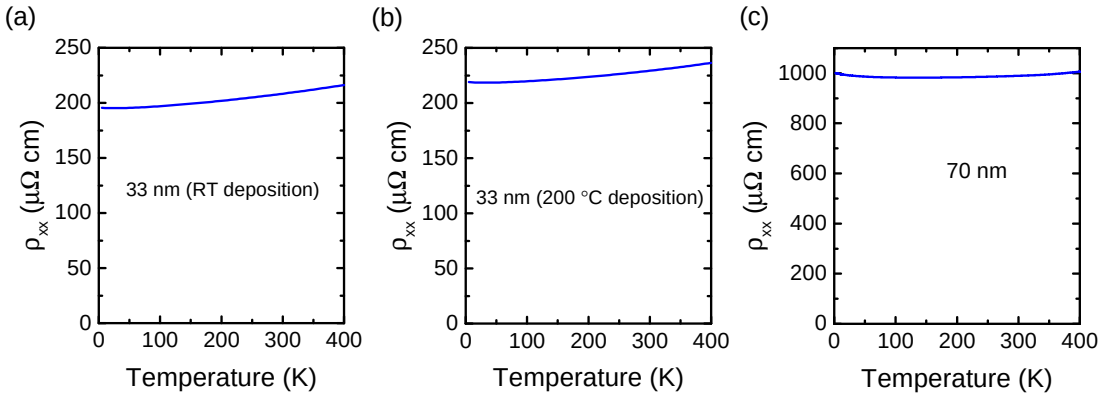

Figure 4.8: Longitudinal resistivity ρ_{xx} as a function of temperature for the (a) 33 nm (room temperature deposition), (b) 33 nm (200 °C deposition), and (c) 70 nm films.

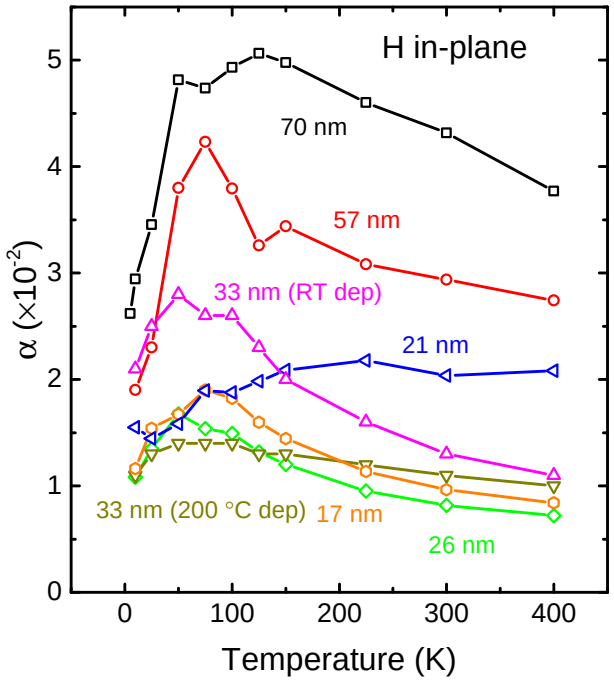

Figure 4.9: Gilbert damping α for IP field shown as a function of temperature for the 17 nm (orange), 21 nm (blue), 26 nm (green), 33 nm room temperature deposition (magenta), 33 nm 200 °C deposition (gold), 57 nm (red), and 70 nm (black) $Fe_{0.7}Ga_{0.3}$ films.

perpendicular to the plane, and how the degree to which it is mitigated depends on the boundary conditions of the film.

Here we outline a theory of magnetoelastic damping, which relies on the damping of magnetoelastic modes through phonon relaxation mechanisms. Figure 4.10 illustrates the flow of energy through such a process. Analytically, the procedure is to equate the steady-state heating rate due to Gilbert damping to the heating rate due to crystal viscosity, and solve for the Gilbert damping α in terms of the crystal shear viscosity η and the magnetostrictive coefficients λ_{hkl}. Shear strain u_{ij} resulting from the magnetoelastic interaction can be expressed as $u_{ij} = \lambda_{111} m_i m_j$ [26], where $m_i \equiv M_i/M_s$ are the reduced magnetizations. The leading-order shears thus have equations of motion given by $\dot{u}_{iz} = \lambda_{111} \dot{m}_i$, where $i = x$ or y, and z is the direction of the static magnetization so that $m_z \approx 1$. Longitudinal modes are quadratic in the dynamical component of the magnetization [25] and so will be neglected in this analysis.

The heating rate due to Gilbert damping can be written as $\dot{Q}_\alpha = \frac{M_s}{\gamma} \alpha (\dot{m}_x^2 + \dot{m}_y^2)$, and the heating rate due to the damping of phonon modes as $\dot{Q}_\eta = 4\eta(\dot{u}_{xz}^2 + \dot{u}_{yz}^2) = 4\eta\lambda_{111}^2(\dot{m}_x^2 + \dot{m}_y^2)$ [82], with the factor of 4 accounting for the symmetry of the strain tensor. Equating the two, and solving for α (henceforward referred to as α_{me}), we obtain

$$\alpha_{me} = \frac{4\gamma}{M_s} \eta \lambda_{111}^2 \ . \tag{4.1}$$

We will restrict our attention to the case of isotropic magnetostriction, and set $\lambda_{111} = \lambda$.

In order to use Eq. 4.1 to estimate α_{me} in our films, we first estimate the shear viscosity, given for transverse phonons with frequency ω and relaxation time τ as [86]

$$\eta = \frac{2\rho c_t^2}{\omega^2 \tau} \ , \tag{4.2}$$

where ρ is the mass density and c_t is the transverse speed of sound. Using $\omega/2\pi =$ 10 GHz, $\tau = 10^{-11}$ s, and $c_t = 2.5$ km/s, we obtain $\eta \approx 2.3$ Pa s. (The estimate of the phonon relaxation time τ is based on a phonon mean free path of the order of the grain size: $\sim$10 nm.) Furthermore, the magnetostriction of an equivalent sample has been measured to be $\sim$100 ppm at room temperature [87]. Then, with $\gamma/2\pi = 29$ GHz/T and $M_s = 1123$ emu/cc (extracted from FMR data taken at 300 K), we estimate $\alpha_{me} \approx$

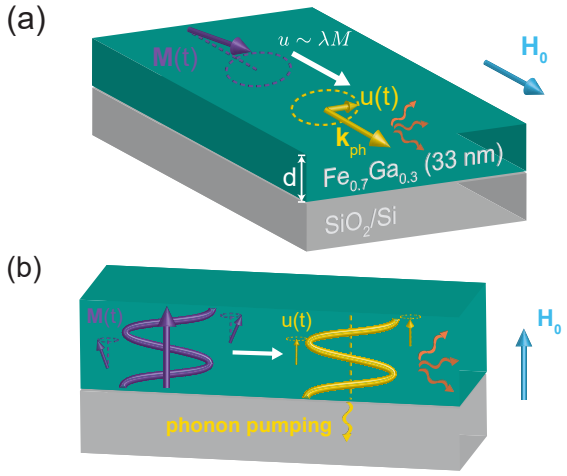

Figure 4.10: (a) Depiction of the magnetoelastic damping process for magnetization in plane and (b) perpendicular to plane, where $\mathbf{M}(t)$ is the magnetization vector and $u(t)$ is the lattice displacement. In panel (b), the magnon-phonon conversion process is suppressed when $d < \pi/k_{ph}$, where d is the film thickness and k_{ph} is the transverse phonon wavenumber at the FMR frequency.

0.016. This estimate gives us immediate cause to suspect that magnetoelastic Gilbert damping is significant (or even dominant) in these films.

We now discuss why the magnetoelastic damping can be much weaker for PP magnetization in sufficiently thin films. We will start by assuming that there is no coupling between the film and substrate, and later we will relax this assumption. In this case the only phonons excited by the magnetization, to leading-order in the magnetizations and strains, are transverse modes propagating in the direction of the static magnetization [25]. One may assume that the minimum allowable phonon wavenumber is given by π/d, where d is the film thickness, since this corresponds to the minimum wavenumber for a substrate having much lower acoustic impedance than the film (requiring the phonons to have antinodes at the interfaces) [83]. (We also assume an easy-axis magnetic anisotropy at the interfaces, so that the magnetization is pinned at the interfaces.) We expect then that the magnetoelastic damping will be suppressed for cases where the phonon wavelength, at the frequency of the precessing magnetization, is greater than

twice the film thickness [see Fig. 4.10(b)]. Thus, in sufficiently thin films (with weakly-coupled substrates), the magnetoelastic damping process can be suppressed when the magnetization is perpendicular to the plane. However, the magnetoelastic damping can be active (albeit mitigated) when there is nonnegligible or "intermediate" coupling to the substrate.

Before moving on, we briefly note the implications of Eq. (4.1) for the temperature dependence of the Gilbert damping. On the basis of the magnetostriction alone, α_{me} would be expected to increase monotonically as temperature is decreased (λ has been shown to increase by nearly a factor of 2 from room temperature to 4 K in bulk samples with similar compositions [2]). However, the viscosity η is expected to decrease at low temperature, leading to the possibility of a local maximum in α_{me}. In polycrystalline samples where the grain size is smaller than the phonon wavelength, viscous damping of phonons due to thermal conduction caused by stress inhomogeneities can be significant [86, 88]. (In our case the phonon wavelengths are $\sim$ 100 nm and the grain sizes are $\sim$ 10 nm.) This effect scales with temperature as $\eta \sim T\alpha_T^2/C\chi$ [88], where α_T is the thermal expansion coefficient, C is the specific heat at constant volume, and χ is the compressibility. At higher temperatures, α_T and C will approach constant values, and χ will always depend weakly on temperature. We therefore expect that the viscosity is approximately linear in T. In this case, α_{me} is maximized where $\lambda^2(T)$ has an inflection point.

4.5 Reconciliation of Data with Magnetoelastic Damping Model

We proceed to explain our data in terms of the mechanism described above, turning our attention again to the PP Gilbert damping for all of the films shown in Fig. 4.6. We previously argued that the magnetoelastic damping mechanism will be suppressed for the case where the acoustic impedances of the film and substrate are mismatched. However, the clear dependence on temperature, which we have already shown is inconsistent with Kamberský damping, appears to be consistent with the magnetoelastic damping mechanism. We estimate that the acoustic impedance of the film (defined as the product of mass density ρ and transverse speed of sound c_t [83]) is about a

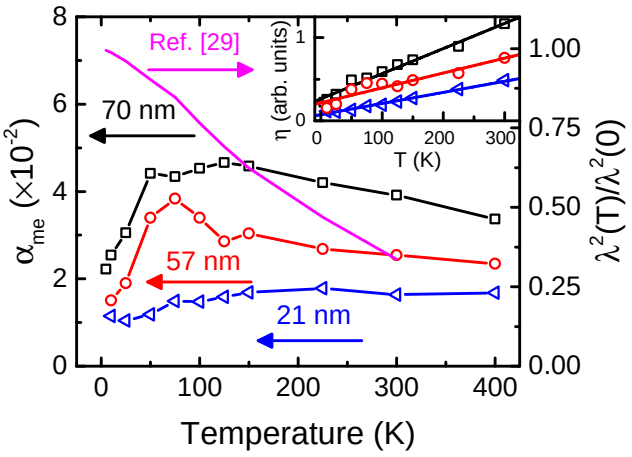

Figure 4.11: Magnetoelastic Gilbert damping α_{me} for the 21 nm (blue), 57 nm (red), and 70 nm (black) films (left ordinate) and $\lambda^2(T)/\lambda^2(0)$ from Clark *et al.* [2] (magenta; right ordinate) shown as a function of temperature. Inset shows the ratio of α_{me} and $\lambda^2(T)/\lambda^2(0)$, labeled as $\eta(T)$, along with linear fits for the 21 nm (blue), 57 nm (red), and 70 nm (black) films.

factor of 2 larger than the substrate. This suggests that the elastic coupling between the film and substrate, albeit weak, may be nonnegligible. Furthermore, experiments with YIG/GGG heterostructures (where the acoustic match is good) have demonstrated magnetic excitation of phononic standing waves that have boundary conditions dictated by the combined thickness of the film and substrate, rather than the film thickness alone (i.e., the wavelengths are much larger than the film thickness) [76, 89]. In this case, the Gilbert damping may contain some contribution from the magnetoelastic mechanism. A final point is that α_{PP} approaches $\simeq 0.004$ at 5 to 10 K for all of the films. Both the magnetostriction and the viscosity are quantities which could have significant variation between samples, leading to variations in α_{me}. However, the viscosity becomes small at low temperature, which means that the Gilbert damping will approach the Kamberský "limit," a property that is determined by the electronic structure, implying that the Kamberský damping is $\simeq 0.004$ in these films and that it is the primary contribution to the Gilbert damping near $T = 0$.

Now we revisit the IP Gilbert damping shown in Fig. 4.9. In this configuration, there is a strong temperature dependence of the Gilbert damping similar to that of the

PP case, again implying the presence of magnetoelastic damping. However, the overall magnitude is much higher. That is because in this case arbitrarily long wavelength phonons can be excited regardless of the thickness of the film. Although we cannot directly measure the magnetostriction as a function of temperature, we estimate the scaling behavior of λ by interpolating the data in Ref. [2] taken for bulk samples of similar composition. In order to demonstrate that α_{IP} scales with temperature as expected from the model, we have plotted the quantities α_{me} and $\lambda^2(T)/\lambda^2(0)$ as functions of temperature in Fig. 4.11—where we define the quantity $\alpha_{me} \equiv \alpha_{IP} - 0.004$—for the 21 nm, 57 nm, and 70 nm films (which are part of the same growth). The correlation between the two quantities is not completely convincing. There is, however, an additional temperature dependence in α_{me} besides $\lambda^2(T)$, namely, the viscosity $\eta(T)$. The inset of Fig. 4.11 shows the ratio of α_{me} and $\lambda^2(T)$, which [from Eq. (4.1)] is proportional to $\eta(T)$. The linear fits provide strong evidence that the mechanism behind the viscosity is indeed the thermal conduction process that we have argued is approximately linear in T. We point out that the 21 nm sample, where α_{IP} exhibits a temperature dependence that is qualitatively different from the rest of the samples (see Fig. 4.9), has a viscosity with similar temperature dependence to the 50 nm and 70 nm films. This suggests that the mechanism underlying the magnetoelastic Gilbert damping is indeed the same. It is noteworthy that the maximum in α_{me} ($\sim$ 50 to 75 K for all of the samples) coincides approximately with the inflection point in $\lambda^2(T)$. This was a consequence of our assumption that $\eta(T)$ should be roughly linear. We also obtain a significant value for the zero-temperature viscosity, which is around 25 % of the value at 300 K. This is likely due to boundary-scattering processes, which will prevent α_{me} from going to zero at low temperatures, particularly for in-plane magnetization where α_{me} is much larger than 0.004 (our estimate for the Kamberský damping). For the PP case, α_{me} is much smaller due to limitations on the wavelengths of phonons that can be excited, so the Gilbert damping of all the samples approaches the Kamberský limit of 0.004 near zero temperature. We also find that $\eta(T)$ is linear for the 33 nm (200 °C deposition) film, but has a more complicated dependence on T for the 17 nm, 26 nm, and 33 nm (room temperature deposition) films (the latter three notably being from the same growth). The viscosity near zero temperature is within roughly a factor of 2 for all seven of the samples, however.

Finally, we propose that this mechanism may be responsible for a Gilbert damping anisotropy of similar magnitude reported in Ref. [65], observed in an epitaxial $Co_{0.5}Fe_{0.5}$ thin film. The authors attributed the anisotropy to the Kamberský mechanism [1, 29–31], arising from tetragonal distortions of the lattice. The magnetostriction is known to be highly anisotropic in bulk $Co_{0.5}Fe_{0.5}$, *viz.*, $\lambda_{100} = 150$ ppm and $\lambda_{111} = 30$ ppm [90]. We therefore expect that the Gilbert damping arising from the mechanism we have described may be much larger for $\mathbf{M} \parallel (110)$ than $\mathbf{M} \parallel (100)$, which is precisely what the authors observed.

4.6 Conclusion

In summary, we observe large and anisotropic magnetoelastic Gilbert damping in $Fe_{0.7}Ga_{0.3}$ polycrystalline thin films (thicknesses ranging from 17 to 70 nm). At 300 K, the damping coefficient is more than a factor of 10 larger for field in plane than it is for field perpendicular to the plane in the 70 nm film. The large anisotropy is caused by a mitigation of the magnetoelastic effect for perpendicular-to-plane fields due to a dependence on the elastic coupling of the film to the substrate, which in our case is weak. Finally, there is a nonmonotonic temperature dependence of the Gilbert damping, which we show is consistent with our model.

Chapter 5

Phonon Pumping in Co/Pd Multilayers

5.1 Introduction to Co/Pd Multilayers

The ability to couple the spin degree of freedom with other degrees of freedom, such as charge or strain, is crucial to many spintronic applications. The coupling of spin to strain is a phenomenon known as magnetostriction, which is known to directly influence magnetization dynamics [76, 84, 91–98]. Some work on dynamical magnon-phonon coupling has focused on the generation of phonons by ferromagnetic resonance (FMR) in a magnetic thin film and subsequent propagation of the phonons into the substrate, which is referred to as phonon pumping [77, 83, 92, 99, 100]. Much of the early work on phonon pumping lacked broadband frequency dependence, which is necessary for fully characterizing the effect as well as demonstrating the existence of multiple resonances. Recent experimental work on phonon pumping has largely relied on time-resolved Kerr measurements [94, 95, 98], which are susceptible to strain excitation through laser heating rather than due to magnetization dynamics alone. Also, the temperature dependence of this effect has not been studied, which may provide new insights into the underlying physics.

In this chapter, we demonstrate the phonon pumping effect by ferromagnetic resonance in a series of $[Co/Pd]_n$ multilayers with perpendicular magnetic anisotropy (PMA). PMA means that the easy direction of the magnetization is perpendicular to

the plane of the film. This is in contrast to the usual case where the easy direction is in the plane of the film—this is caused by magnetostatic effects. Generally speaking, the magnetostatic energy will dominate interfacial effects that favor PMA in a thin film provided the thickness is greater than ∼1 to 10 nm. (There are, however, cases where a material has PMA in the bulk, such as in FePd, which is discussed in Appendix E.) It is shown that the strength of the effect is strongly temperature dependent (a factor of ~ 4 enhancement at 10 K relative to 300 K)—much more than would be expected from the temperature dependence of the magnon-phonon coupling alone (less than a factor of 2 enhancement)—which is due to the sensitivity of the phonon pumping to the pinning of the dynamic magnetization. We also show that the frequencies of the phonon pumping resonances can be tuned by varying n, the number of Co/Pd repetitions. The results of this chapter are contained in a manuscript currently under review at *Physical Review Letters*.

Co/Pd multilayers are well-known for their strong magnon-phonon coupling and PMA [101] and have been demonstrated for use in perpendicular magnetic tunnel junctions (p-MTJ) [102], including cases where synthetic antiferromagnets (SAF) made from Co/Pd multilayers were used for the reference layers [103, 104]. The PMA is particularly significant for this application since phonon pumping is more efficient for perpendicular magnetization. The reason is that the strongest coupling in this configuration is to transverse phonons propagating perpendicular to the interfaces [25, 83, 105], which can easily escape into the substrate. $[\text{Co}(0.8\text{ nm})/\text{Pd}(1.5\text{ nm})]_n$ multilayers (n = 6, 11, 15, and 20) were grown by dc magnetron sputtering at room temperature with a base pressure of $< 5\times10^{-8}$ Torr using Ar gas at a working pressure of 2.0 mTorr. The thicknesses of the Co and Pd layers are 0.8 nm and 1.5 nm, respectively, for all of the samples and will henceforth be omitted. Ferromagnetic resonance (FMR) of the $[\text{Co/Pd}]_n$ multilayers [Fig. 5.1(a)] was measured using a coplanar waveguide setup with modulation of the applied magnetic field for lock-in detection of the transmitted microwave power, which was rectified with a Schottky diode detector. Further details of the experiment, including example FMR lineshapes, are given in Chapter 1. Magnetometry measurements were performed on all the multilayers using superconducting quantum interference device (SQUID) magnetometry. SQUID was used to measure hysteresis loops over a range of temperatures (5 to 300 K) for both in-plane and out-of-plane applied fields, which

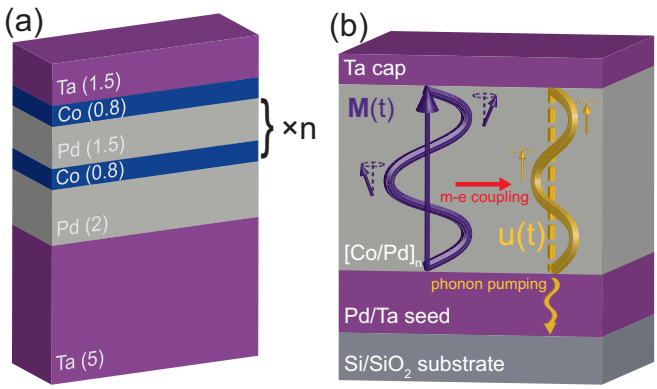

Figure 5.1: (a) Stack structure of the $[\mathrm{Co/Pd}]_n$ multilayers. Thicknesses of each layer are given in parentheses and have units of nm. The Co(0.8 nm)/Pd(1.5 nm) bilayer is repeated a total of n times as indicated on the figure. (b) Schematic of the phonon pumping process in the configuration where the magnetization $\mathbf{M}(t)$ is normal to the plane of the film. The magnetization depth profile is given by a sine wave (for simplicity) with pinning at the interfaces. The magnetoelastic coupling (shown by the red arrow) leads to the creation of a phonon standing wave with displacement $u(t)$. The phonon pumping process is shown by the wavy gold arrow representing the leakage of phonons into the seed layers and substrate.

confirmed an out-of-plane easy axis in all the samples. SQUID was also used to measure the saturation magnetization as a function of temperature in the multilayers.

5.2 Resonant Damping Via Phonon Pumping

We first demonstrate the effect of phonon pumping on the FMR linewidths and how it depends on the number of Co/Pd repetitions in the multilayer stack. Figure 5.1(b) shows a schematic of the phonon pumping process, where magnetization dynamics are damped by the leakage of magnetoelastically-driven phonons into the substrate. Figure 5.2 shows FMR linewidths measured in a perpendicular field as a function of frequency at 150 K for four different $[\mathrm{Co/Pd}]_n$ multilayer structures with $n = 6$, 11, 15, and 20. The lower frequency limit of the measurements is determined by the perpendicular anisotropy field (which sets the zero-field FMR frequency) for the $n = 6$ and 11 samples. For the $n = 15$ and 20 samples, the FMR signal disappears at low field, where the sample is no longer saturated. This observation is corroborated by out-of-plane magnetic hysteresis loops,

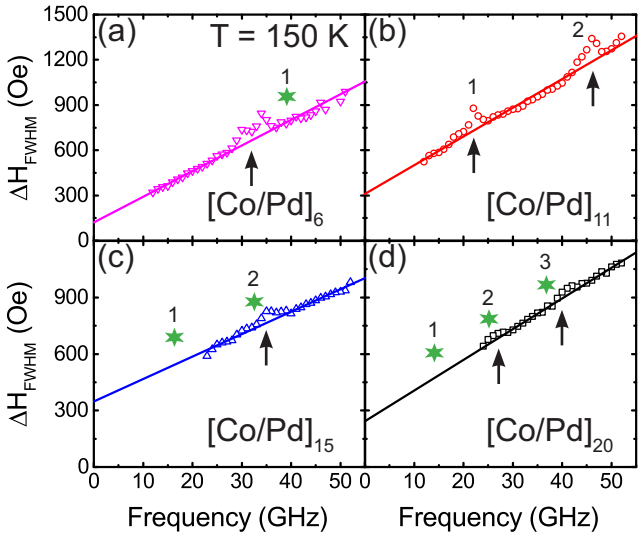

Figure 5.2: Ferromagnetic resonance linewidths as a function of frequency with applied magnetic field out of plane at $T = 150$ K for (a) $[Co/Pd]_6$ (magenta triangles), (b) $[Co/Pd]_{11}$ (red circles), (c) $[Co/Pd]_{15}$ (blue triangles), and (d) $[Co/Pd]_{20}$ (black squares). The vertical arrows indicate the positions of the phonon pumping resonances, and the green stars indicate the corresponding positions predicted from the positions observed in the $[Co/Pd]_{11}$ multilayer. The numbers labelling the stars correspond to the number of half-waves in the thickness resonance so that, e.g., "3" means a phonon standing wave with wavelength $\lambda = 3d/2$, where d is the thickness of the magnetic portion of the multilayer.

which show the nucleation of domains before zero field is reached.

For all of the samples shown in Fig. 5.2, there are resonant linewidth enhancements that appear at specific frequencies. The linear background is due to the Gilbert damping, for which fits were generated by excluding points within 3 GHz of the center of the peaks. For the $n = 11$ and 20 multilayers, there are two resonant peaks in the linewidth. In the $n = 11$ multilayer, the frequency of the high-frequency peak is double that of the low-frequency peak, implying that these represent the first and second harmonics of a fundamental resonance. In the $n = 20$ multilayer, the high-frequency peak is 3/2 that of the low-frequency peak, suggesting that the low- and high-frequency peaks are the second and third harmonics of a fundamental resonance, respectively. We cannot observe the fundamental resonance, however, since it is expected at a frequency ($\simeq 13$

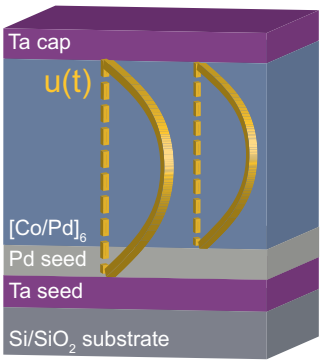

Figure 5.3: Schematic showing two standing-wave transverse acoustic phonons having displacement $u(t)$. The dashed lines indicate the lines of zero displacement. Both phonons have a node at the top of the $[Co/Pd]_6$ multilayer. The phonon on the left has a node at the bottom of the Pd seed layer, while the phonon on the right has a node at the bottom of the $[Co/Pd]_6$ multilayer

to 14 GHz) at which the sample is unsaturated. For the $n = 6$ and 15 multilayers, there is one peak in the linewidth. This corresponds to the fundamental resonance in the $n = 6$ multilayer, and the second harmonic in the $n = 15$ multilayer. The fundamental resonance is undetectable in the $n = 15$ multilayer because it occurs at a frequency ($\simeq$ 16 GHz) at which the sample is unsaturated. We note that the resonance in the $[Co/Pd]_6$ multilayer exhibits a twin-peak structure, with the two peaks separated by approximately 4 GHz. This may be due to the existence of standing waves with nodes at both the interface between the 2-nm Pd and 5-nm Ta seed layers *and* the interface between the Co and 2-nm Pd seed layer [shown in Fig. 5.1(a)]. (A schematic of both modes is shown in Fig. 5.3.) Were this the case, one would expect a spacing of about 4 GHz, as we observe. This hypothesis predicts a peak spacing of $\lesssim$ 1 GHz for the thicker multilayers, which would explain why the twin-peak structure is only observed in the $[Co/Pd]_6$ multilayer.

The vertical arrows in Fig. 5.2 indicate the positions of the resonances for each multilayer. Transverse acoustic phonon standing waves are expected at frequencies where d, the thickness of the stack excluding capping and seed layers, matches an integer number of phonon half wavelengths. This condition can be expressed as $f = c_t/(2d/m)$ (c_t is the transverse speed of sound and m is a positive integer). Longitudinal phonons are neglected because they couple to the magnetization at higher order [25, 83, 106].

The hypothesis that the multilayer is a half-wave resonator is based on the fact that the highly-dense Ta capping and seed layers will lead to pinning of the phonons at these interfaces. The green stars in panels (a), (c), and (d) indicate the positions of the resonances predicted from the positions observed in the $[Co/Pd]_{11}$ multilayer in panel (b), where the effect is strongest. The numbers labelling the stars indicate the order of the resonance, so that a resonance of order m corresponds to a phonon standing wave of wavelength $\lambda = 2d/m$. From this we note that there is good agreement between the observed and predicted positions of the resonances, which demonstrates that the resonances can indeed be thought of as "thickness" resonances. The most significant deviation is observed in the $[Co/Pd]_6$ sample, which is the thinnest and therefore most sensitive to changes in the effective thickness at the top and bottom interfaces.

We did not observe any thickness resonances for IP magnetization, which is expected due to the fact that the strongest coupling is to phonons propagating parallel to the static magnetization [25, 83, 106] which will therefore not propagate into the substrate. We demonstrate this fact in Fig. 5.4, where the FMR linewidths (with Gilbert damping and inhomogeneous broadening contributions subtracted) of the $[Co/Pd]_{11}$ multilayer with IP magnetization are shown at different temperatures. The lower-frequency limit was set by the field below which the sample was unsaturated. The dashed curves are the fits obtained from the PP linewidths. The disagreement between the IP FMR linewidths and the solid curves demonstrates the lack of thickness resonances, and therefore phonon pumping, for IP magnetization.

5.3 Temperature Dependence of Phonon Pumping

The temperature dependence of the phonon pumping contribution to the FMR linewidths of the $[Co/Pd]_{11}$ multilayer is shown in Fig. 5.5 for temperatures ranging from 10 to 300 K. The phonon pumping contribution is quantified by fitting the full-width-at-half-maximum (FWHM) FMR linewidths to the form

$$\Delta H_{FWHM} = \Delta H_0 + 2\alpha\omega/\gamma + \Delta H_{ph}(\omega) \ , \tag{5.1}$$

where ΔH_0 is the frequency-independent inhomogeneous broadening, $2\alpha\omega/\gamma$ is the contribution from Gilbert damping (α is the Gilbert damping constant and γ is the gyromagnetic ratio), and $\Delta H_{ph}(\omega)$ is the nonlinear frequency-dependent contribution from

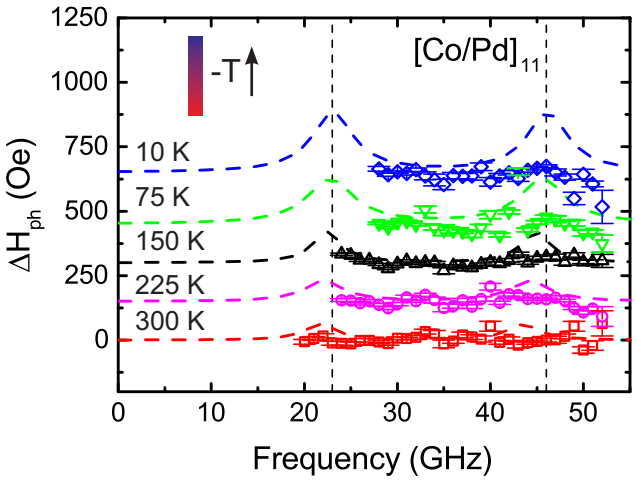

Figure 5.4: Ferromagnetic resonance linewidths—with Gilbert damping and inhomogeneous broadening contributions subtracted—as a function of frequency for the $[Co/Pd]_{11}$ multilayer with in-plane magnetization at temperatures of 10 K (blue diamonds), 75 K (green triangles), 150 K (black triangles), 225 K (magenta circles), and 300 K (red squares). The dashed curves are fits to different sets of data—the corresponding $\Delta H_{ph}(\omega)$ with perpendicular-to-plane magnetization—for the purposes of contrast. The data below 300 K were given a positive vertical offset so that the individual datasets could be more easily distinguished.

phonon pumping. We assume a phenomenological Lorentzian lineshape for the form of $\Delta H_{ph}(\omega)$:

$$\Delta H_{ph}(\omega) = \sum_n 2A_n \frac{\delta\omega/2}{(\omega - n\omega_0)^2 + (\delta\omega/2)^2} \ , \tag{5.2}$$

where $\delta\omega$ is the FWHM of the resonance, ω_0 is the frequency of the fundamental half-wave resonance, and A_n sets the amplitude (the factor of 2 is needed to convert from HWHM to FWHM). In the case of the $[Co/Pd]_{11}$ multilayer, we enforce the constraints that the high-frequency resonance is exactly twice the low-frequency resonance and that the amplitudes of both resonances are equal. The widths of the resonances—inversely proportional to the lifetime of the phonons in the multilayer—are set by the acoustic impedance ratios at the boundaries, so that a strong mismatch will yield a sharp resonance [83, 92, 93, 105, 107]. In principle, phonon relaxation within the multilayer can influence the resonance width [93, 105, 107], but this is likely negligible since the widths are independent of temperature. The elastic coupling of the multilayer to the substrate, which determines the width of the resonances for the case of phonon pumping, depends negligibly on temperature, which is not generally the case for phonon relaxation within the multilayer [84, 108].

It is clear from Fig. 5.5 that the intensity of the thickness resonances increases strongly at low temperature. (In contrast, the Gilbert damping—shown in Fig. 5.6—depends very weakly on temperature.) The amplitudes of the resonances are about a factor of 4 larger at 10 K relative to 300 K. A strong temperature dependence of the amplitude of the resonances is seen for all of the multilayers, increasing at low temperature by a magnitude similar to that seen in Fig. 5.5 for the $[Co/Pd]_{11}$ sample. Also noteworthy is the small upward shift in the frequency of the resonances with decreasing temperature. This is consistent with the expectation that the elastic moduli should increase at low temperature, causing an increase in the speed of sound (which is proportional to the frequency of a given thickness resonance). The frequencies of the first and second thickness resonances shift from 22 and 44 GHz to 23 and 46 GHz, respectively.

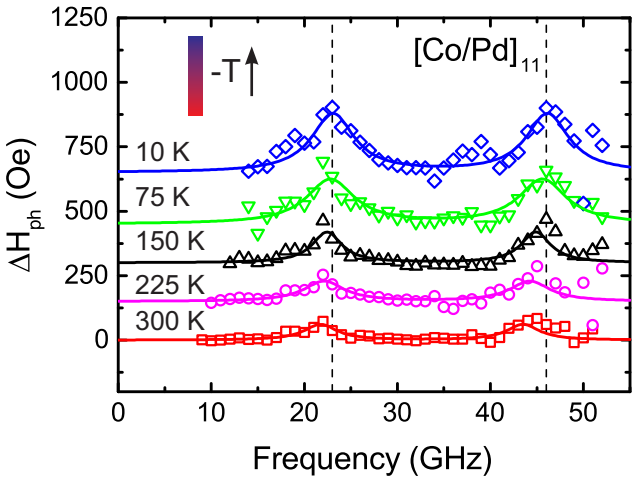

Figure 5.5: Evolution of the phonon pumping contribution to the FMR linewidths ΔH_{ph} with temperature for the $[Co/Pd]_{11}$ multilayer at temperatures of 10 K (blue diamonds), 75 K (green triangles), 150 K (black triangles), 225 K (magenta circles), and 300 K (red squares). The vertical dashed lines indicate the locations of the phonon pumping peaks, 23 GHz and 46 GHz (at 10 K), which correspond to phonon wavelengths of $\lambda = 2d$ and $\lambda = d$, respectively, where d is the thickness of the multilayer (excluding capping and seed layers). The data below 300 K are offset vertically so that the individual datasets could be more easily distinguished.

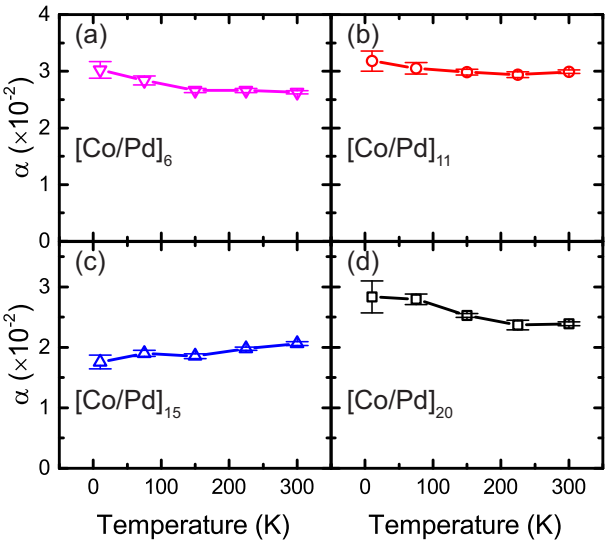

Figure 5.6: Gilbert damping as a function of temperature measured with applied field out of the plane for (a) $[Co/Pd]_6$, (b) $[Co/Pd]_{11}$, (c) $[Co/Pd]_{15}$, and (d) $[Co/Pd]_{20}$ multilayers.

5.4 Effect of Surface Pinning on Phonon Pumping

There has been significant theoretical work attempting to model phonon pumping [83, 99, 105–107, 109–111], and so we will not give a comprehensive overview here. All models predict that the phonon pumping amplitude should go as the square of the magnetoelastic coefficient, which can be understood in terms of Fermi's golden rule (similar to the case for the magnetoelastic Gilbert damping derived in Chapter 4). One of the primary factors influencing the phonon pumping is the nonuniformity of the dynamic magnetization, which is necessary for exciting acoustic phonons (since they have nonzero wave vector). The model presented by Streib *et al.* [83] assumes uniform magnetization within the film, with the only nonuniformity coming from the discontinuity of the magnetization at the interfaces of the film. It is important to note that this model predicts the excitation of only odd-integer half-wave resonances ($d = \lambda/2,\ 3\lambda/2,\ \ldots$) due to destructive interference at frequencies where the phonons are even-integer half-waves. Our data show clearly that both even and odd resonances are excited, however, which relates to the fact that the dynamic magnetization in these

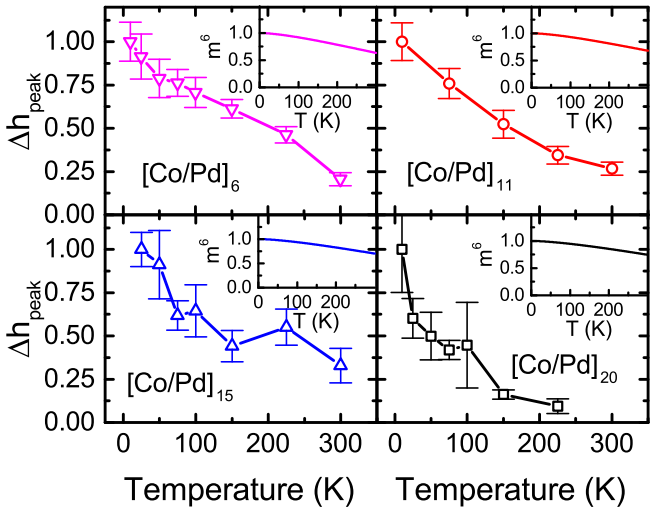

Figure 5.7: Normalized peak values of $\Delta H_{ph}(\omega)$ as a function of temperature, defined by $\Delta h_{peak} \equiv \Delta H_{peak}(T)/\Delta H_{peak}(10\,\mathrm{K})$, for the (a) $[\mathrm{Co/Pd}]_6$, (b) $[\mathrm{Co/Pd}]_{11}$, (c) $[\mathrm{Co/Pd}]_{15}$, and (d) $[\mathrm{Co/Pd}]_{20}$ multilayers. Insets show m^6 as a function of temperature.

multilayers is certainly nonuniform. Furthermore, the boundary conditions likely differ at the bounding interfaces at the top and bottom of the multilayer (Ta/Co on top and Co/Pd on bottom). The interior of the multilayer also promotes nonuniform static magnetization due to the nonuniformity inherent in the proximity-induced magnetism in the Pd layers. The differences between our observations and the predictions of the model of Streib *et al.* [83] underscore the importance of boundary conditions in the phonon pumping process, and it is probable that the complex magnetization depth profile associated with magnetic multilayers serves to enhance the phonon pumping.

The temperature dependence of the phonon pumping strength is expected to be primarily due to the dependence of magnetostriction on temperature [83, 92]. It can be shown that since the magnetoelastic energy is quadratic in the magnetization cosines [25], the magnetoelastic energy should scale with temperature as $m^3(T)$ [112–114], where $m(T) \equiv M(T)/M(0)$ is the reduced magnetization. As mentioned earlier, the phonon pumping amplitude depends on the square of the magnetoelastic energy and would therefore be expected to scale with temperature as m^6.

Figure 5.7 shows the temperature dependence of the maximum value of $\Delta H_{ph}(\omega)$

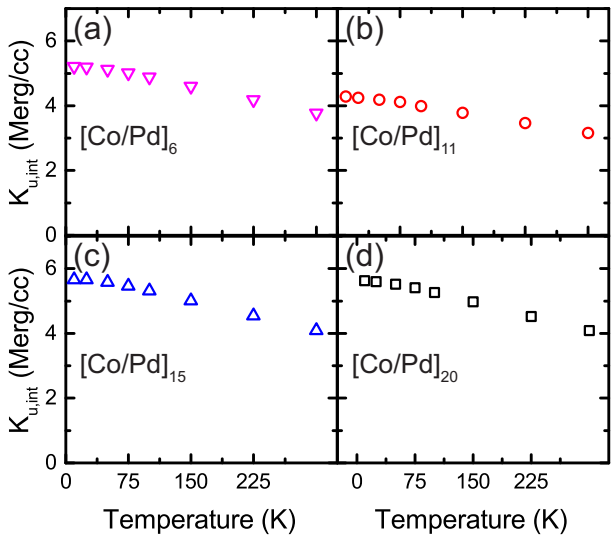

Figure 5.8: Uniaxial interface anisotropy $2K_{u,int}/M_s = 4\pi M_s - H_{k,eff}$ as a function of temperature for the (a) $[Co/Pd]_6$, (b) $[Co/Pd]_{11}$, (c) $[Co/Pd]_{15}$, and (d) $[Co/Pd]_{20}$ multilayers.

for all the multilayers, normalized by the maximum value at 10 K. The damping enhancement depends quite strongly on temperature, with the effect being a factor of at least 4 greater at low temperature compared to room temperature. This depends on temperature much more strongly than m^6 (shown in the insets of Fig. 5.7), which ranges from $\simeq 0.65$ to 0.75 at 300 K in the four multilayers. In addition to the magnetoelastic coupling, the pinning of the dynamic magnetization can strengthen the coupling to phonons, since they are driven by variations in the magnetization [25]. The pinning at the exterior interfaces of the multilayer [Co/Ta on the top and Co/Pd on the bottom, see Fig. 5.1(a)] becomes stronger at low temperature due to an increase in the interfacial anisotropy energy [114].

The pinning is also seen to have an effect on the FMR field, observed through a stronger-than-expected temperature dependence of the interface anisotropy measured with FMR. The interface anisotropy of the multilayers was determined from the relation $2K_{u,int}/M_s = 4\pi M_s - H_{k,eff}$, where $H_{k,eff}$ is the net perpendicular anisotropy field measured with FMR and M_s is the saturation magnetizion determined from SQUID VSM. The interface anisotropy $K_{u,int}$ is shown as a function of temperature in Fig. 5.8

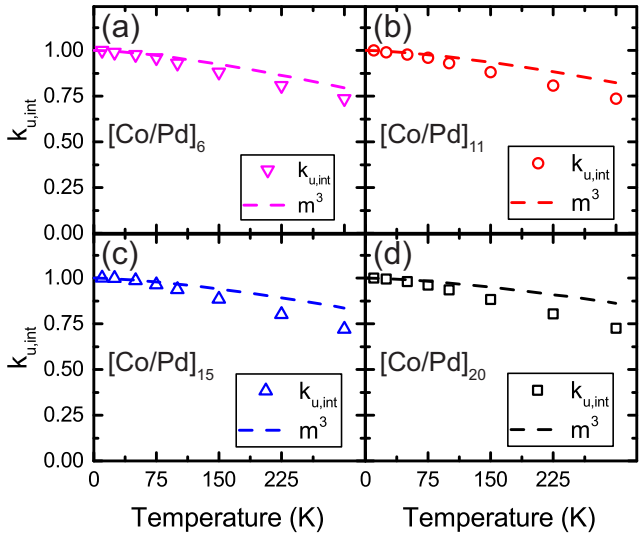

Figure 5.9: Reduced anisotropy field $k_{u,int} \equiv K_{u,int}(T)/K_{u,int}(10\text{ K})$ (symbols) and m^3 (dashed lines) as functions of temperature for the (a) $[\text{Co/Pd}]_6$, (b) $[\text{Co/Pd}]_{11}$, (c) $[\text{Co/Pd}]_{15}$, and (d) $[\text{Co/Pd}]_{20}$ multilayers.

for the four multilayers.

A uniaxial interface anisotropy, like the magnetoelastic anisotropy, is expected to scale with temperature as the cube of the saturation magnetization [114]. The reduced interface anisotropy $k_{u,int} \equiv K_{u,int}(T)/K_{u,int}(10\text{ K})$ is shown as a function of temperature in Fig. 5.9, along with the quantity m^3. From Fig. 5.9 it can be seen that the interface anisotropy depends more strongly on temperature than the m^3 scaling law. This is consistent with our previous statement that the magnetization is more strongly pinned at low temperature. The reason is that the anisotropy energy measured with FMR overestimates the real anisotropy in the presence of pinning, because the pinning adds exchange energy [115]. This has the same effect as increasing the interface anisotropy (in the case of perpendicular magnetization), namely, a decrease in the FMR field for a given frequency.

To estimate the order of magnitude of the effect of pinning on the FMR field, we start by assuming that the measured interface anisotropy $K_{u,int}$ consists of the true interface anisotropy energy $K_{u,int}^{true}$ and a pinning energy (arising from increased exchange energy

induced by the pinning) K_p, so that

$$K_{u,int} = K_{u,int}^{true} + K_p \ . \tag{5.3}$$

We can quantify K_p by looking at the difference between the temperature scaling of the measured, normalized interface anisotropy $k_{u,int}$ and the expected m^3 scaling. We will also assume that K_p is vanishingly small compared to $K_{u,int}^{true}$ at 300 K, so that $K_{u,int}(300\text{ K}) \simeq K_{u,int}^{true}(300\text{ K})$. In that case, we can calculate the expected interface anisotropy field at low temperature via

$$K_{u,int}^{true}(10\text{ K}) \simeq K_{u,int}^{true}(300\text{ K})/m^3(300\text{ K}) \ , \tag{5.4}$$

where $m^3(10\text{ K})$ is approximated as unity. For the $[\text{Co/Pd}]_6$ multilayer, $K_{u,int}(300\text{ K}) \simeq$ 3.8 Merg/cc and $m^3(300\text{ K}) \simeq 0.79$, so $K_{u,int}^{true}(10\text{ K}) \simeq 4.8$ Merg/cc. Then, using Eq. 5.3 and the fact that $K_{u,int}(10\text{ K}) \simeq 5.2$ Merg/cc, we obtain $K_p(10\text{ K}) \simeq 0.4$ Merg/cc. The pinning energy is therefore about 10 % of the interface anisotropy energy. The pinning field is $H_p(10\text{ K}) = 2K_p(10\text{ K})/M_s(10\text{ K}) \simeq 1.1$ kOe. The estimated magnitude of the pinning field is about a factor of 10 smaller than the interface anisotropy field (~ 10 kOe), so the pinning produces an effect of reasonable magnitude.

5.5 Dispersive Effect of Phonon Pumping

We consider here the effect of coupling to phonons on the effective field acting on the dynamic magnetization. Figure 5.10 shows the observed shifts in FMR field as a function of frequency for the $[\text{Co/Pd}]_6$ and $[\text{Co/Pd}]_{11}$ multilayers at 10 K. The shifts are quantified by deviations of the FMR fields from the Kittel dispersion, so that the FMR field as a function of frequency is given by

$$H_{FMR} = \omega/\gamma - H_{k,eff} + \delta H_{FMR}(\omega) \ , \tag{5.5}$$

where $H_{k,eff}$ is the uniaxial out-of-plane anisotropy field (containing both shape and interface contributions, defined here as positive for a PMA material), and $\delta H_{FMR}(\omega)$ is the frequency-dependent shift in FMR field due to phonon pumping. The Kramers-Kronig relations of linear response theory imply that an absorptive effect, here a resonant enhancement of the FMR linewidths, must be accompanied by a dispersive effect, i.e.

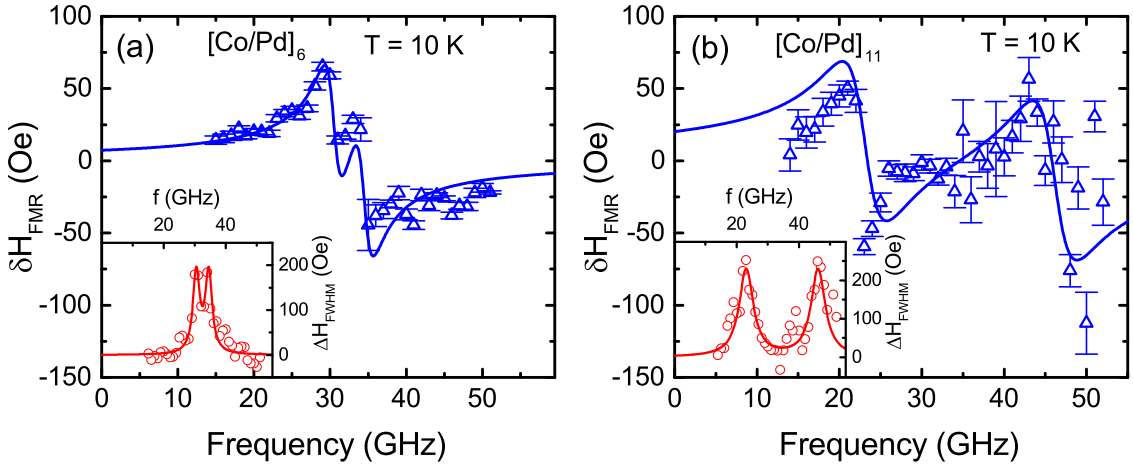

Figure 5.10: Shifts in the FMR field as a function of frequency at 10 K for the (a) $[Co/Pd]_6$ and (b) $[Co/Pd]_{11}$ multilayers. The insets in both panels show the corresponding linewidth enhancements as a function of frequency at 10 K. The solid curves in the main panels are predictions based on the fits of the linewidths in the insets using Kramers-Kronig relations.

a shift in the FMR field. Given that the absorptive response is a Lorentzian, given by Eq. (5.2), the field shifts caused by the dispersive response must be of the form

$$\delta H_{FMR}(\omega) = \sum_n -A_n \frac{\omega - n\omega_0}{(\omega - n\omega_0)^2 + (\delta\omega/2)^2} \ , \tag{5.6}$$

where the parameters $\delta\omega$, ω_0, and A are the same as in Eq. (5.2). The solid curves in the main panels of Fig. 5.10 are predictions of the FMR field shifts based on the linewidth enhancements (the absorptive response): The parameters $\delta\omega$, ω_0, and A_n are determined from fits of the linewidths to Eq. (5.2) [via Eq. (5.1)], and used to predict the FMR field shifts via Eq. 5.6 with no free parameters. It can be seen from Fig. 5.10 that there is good agreement between the observed and predicted FMR field shifts. We also note that the twin-peak structure seen in the linewidths of the $[Co/Pd]_6$ multilayer [inset of Fig. 5.10(a)] manifests as a kink between the two extrema in the FMR field shifts [main panel of Fig. 5.10(a)].

5.6 Conclusion

The Co/Pd multilayer system is an ideal platform for phonon pumping due to the strong magnon-phonon interaction and PMA, which opens up the possibility of engineering devices that utilize this effect at zero applied field in the advantageous perpendicular configuration. As we have demonstrated, the frequency of the phonon pumping resonance is highly tunable through the number of Co/Pd repetitions, which notably does not significantly affect the magnitude of the PMA. It is therefore feasible to engineer a Co/Pd multilayer that experiences a phonon pumping resonance at zero external field.

In conclusion, we report a strong phonon pumping effect in a series of Co/Pd PMA multilayers. The phonon pumping is observed primarily through resonant damping enhancements of the FMR mode, which are determined by the thickness of the multilayer. A complementary effect—a shift in the FMR field caused by phonon pumping—was also demonstrated and, furthermore, could be predicted from the damping enhancements using Kramers-Kronig relations. The phonon pumping effect is strongly enhanced at low temperatures—more so than would be expected from the temperature dependence of the magnon-phonon coupling alone. The pinning of the dynamic magnetization serves to enhance the coupling between the two modes, and is ultimately responsible for the anomalous temperature dependence since the pinning becomes stronger at low temperature. Our results indicate that interfacial engineering will play a key role in either enhancing or suppressing this process, and should be an emphasis of future work.

Chapter 6

Conclusion and Outlook

In this thesis, we have experimentally elucidated the physical mechanisms that can cause magnetization damping in a number of different thin film and multilayer structures. A general motif is that the Kamberský model of damping introduced in Chapter 1 is often insufficient to predict what is observed in experiment. The systems studied in this thesis have potential for use in spintronic applications, and quantification of damping is essential because it governs key metrics such as speed and efficiency in many of these applications.

In Chapter 2, we demonstrated the existence of a strong TMS damping mechanism in a series of epitaxial Heusler alloy thin films. The mechanism can be suppressed by orienting the magnetization perpendicular to the film plane. It was shown that the low intrinsic damping of these materials enhances the extrinsic TMS scattering contribution. In Chapter 3 we demonstrated that two-magnon scattering can cause a shift in the resonance frequency, and that it is in fact complementary to the damping caused by TMS. Chapter 4 demonstrated a strong magnetoelastic damping mechanism in a series of $Fe_{0.7}Ga_{0.3}$ thin films. The signatures of this mechanism were both the giant anisotropy and anomalous temperature dependence of the Gilbert damping. Finally, in Chapter 5, we demonstrated a form of damping that was magnetoelastic in origin—but qualitatively different than the one discussed in Chapter 4—in a series of $[Co/Pd]_n$ multilayers. This mechanism is known as phonon pumping because energy is carried away by phonons that are pumped into the substrate by the magnetization dynamics. The temperature dependence of the effect revealed that the interfacial pinning of the

dynamic magnetization enhances the pumping efficiency.

Despite the knowledge gained from this work, it is important to note that we have restricted our attention to systems having effectively infinite lateral dimensions. Shrinking the lateral dimensions to the nanoscale is necessary for real-world applications, and it has already been demonstrated that additional damping mechanisms can arise due to lateral confinement [116–118]. Furthermore, there has not been any work on the effects of magnon-phonon coupling on damping in nanostructures. Probes like Brillouin light scattering that can detect both magnon and phonon excitations—in principle for individual nanostructures—would be effective for this purpose. Ultrafast laser probes can also accomplish this [119], but the heating of the sample due to the intensity of the laser pulse can excite longitudinal phonons very efficiently, obscuring the intrinsically stronger coupling of the magnetization to transverse phonons. In this thesis we have shown that the effects of confinement in the vertical direction play an essential role in determining the magnitude of damping originating from magnetoelastic coupling, which implies that it will become even more relevant when confinement is imposed in all directions.

References

[1] K. Gilmore, Y. U. Idzerda, and M. D. Stiles, "Identification of the Dominant Precession-Damping Mechanism in Fe, Co, and Ni by First-Principles Calculations," Phys. Rev. Lett. **99**, 027204 (2007).

[2] A. E. Clark, M. Wun-Fogle, J. B. Restorff, K. W. Dennis, T. A. Lograsso, and R. W. McCallum, "Temperature dependence of the magnetic anisotropy and magnetostriction of $Fe_{100-x}Ga_x$ (x = 8.6, 16.6, 28.5)," J. Appl. Phys. **97**, 10M316 (2005).

[3] T. Graf, C. Felser, and S. S. Parkin, "Simple rules for the understanding of Heusler compounds," Prog. Solid State Chem. **39**, 1 (2011).

[4] R. A. Duine, K. J. Lee, S. S. Parkin, and M. D. Stiles, "Synthetic antiferromagnetic spintronics," Nat. Phys. **14**, 217 (2018).

[5] M. N. Baibich, J. M. Broto, A. Fert, F. N. Van Dau, F. Petroff, P. Eitenne, G. Creuzet, A. Friederich, and J. Chazelas, "Giant magnetoresistance of (001)Fe/(001)Cr magnetic superlattices," Phys. Rev. Lett. **61**, 2472 (1988).

[6] C. Chappert, A. Fert, and F. N. Van Dau, "The emergence of spin electronics in data storage," Nat. Mater. **6**, 813 (2007).

[7] M. I. D'yakonov and V. I. Perel', "Current-induced spin orientation of electrons in semiconductors," Phys. Lett. A **35**, 459 (1971).

[8] Y. K. Kato, R. C. Meyers, A. C. Gossard, and D. D. Awschalom, "Observation of the Spin Hall Effect in Semiconductors," Science **306**, 1910 (2004).

[9] K. Narayanapillai, X. Qiu, Y. Wang, J. Kwon, J. Yu, L. M. Loong, W. Legrand, J. Yoon, K. Banerjee, and H. Yang, "Spin-Transfer versus Spin-Orbit Torque MRAM," in *2016 IEEE International Nanoelectronics Conference (INEC)* (2016) pp. 1–2.

[10] A. A. Serga, A. V. Chumak, and B. Hillebrands, "YIG magnonics," J. Phys. D. Appl. Phys. **43**, 264002 (2010).

[11] A. V. Chumak, V. I. Vasyuchka, A. A. Serga, and B. Hillebrands, "Magnon spintronics," Nat. Phys. **11**, 453 (2015).

[12] S. K. Kim, G. S. D. Beach, K.-J. Lee, T. Ono, T. Rasing, and H. Yang, "Ferrimagnetic spintronics," Nat. Mater. **21**, 24 (2022).

[13] S. Manipatruni, D. E. Nikonov, C.-C. Lin, T. A. Gosavi, H. Liu, B. Prasad, Y.-L. Huang, E. Bonturim, R. Ramesh, and I. A. Young, "Scalable energy-efficient magnetoelectric spin–orbit logic," Nature **565**, 35 (2019).

[14] K. Manna, Y. Sun, L. Muechler, J. Kübler, and C. Felser, "Heusler, Weyl and Berry," Nat. Rev. Mater. **3**, 244 (2018).

[15] R. A. de Groot, F. M. Mueller, P. G. van Engen, and K. H. J. Buschow, "New Class of Materials: Half-Metallic Ferromagnets," Phys. Rev. Lett. **50**, 2024 (1983).

[16] T. A. Peterson, S. J. Patel, C. C. Geppert, K. D. Christie, A. Rath, D. Pennachio, M. E. Flatté, P. M. Voyles, C. J. Palmstrøm, and P. A. Crowell, "Spin injection and detection up to room temperature in Heusler alloy/n-GaAs spin valves," Phys. Rev. B **94**, 235309 (2016).

[17] I. Galanakis, P. H. Dederichs, and N. Papanikolaou, "Origin and properties of the gap in the half-ferromagnetic Heusler alloys," Phys. Rev. B **66**, 134428 (2002).

[18] C. Liu, C. K. A. Mewes, M. Chshiev, T. Mewes, and W. H. Butler, "Origin of low Gilbert damping in half metals," Appl. Phys. Lett. **95**, 022509 (2009).

[19] J. H. Griffiths, "Anomalous high-frequency resistance of ferromagnetic metals," Nature **158**, 670 (1946).

[20] C. Kittel, "Interpretation of Anomalous Larmor Frequencies in Ferromagnetic Resonance Experiment," Phys. Rev. **71**, 270 (1947).

[21] C. Kittel, "On the Theory of Ferromagnetic Resonance Absorption," Phys. Rev. **73**, 155 (1948).

[22] A. H. Morrish, "Resonance in Strongly Coupled Dipole Systems," in *The Physical Principles of Magnetism*, Vol. 152 (Wiley-IEEE Press, 2001) Chap. 10, pp. 539–639.

[23] J. Smit and H. G. Beljers, "Ferromagnetic Resonance Absorption in $BaF_{12}O_{19}$, a Highly Anisotropic Crystal," Philips Res. Rep. **10**, 113 (1955).

[24] H. Suhl, "Ferromagnetic Resonance in Nickel Ferrite Between One and Two Kilomegacycles," Phys. Rev. **97**, 555 (1955).

[25] C. Kittel, "Interaction of Spin Waves and Ultrasonic Waves in Ferromagnetic Crystals," Phys. Rev. **110**, 836 (1958).

[26] L. D. Landau, E. M. Lifshitz, and L. P. Pitaevskii, *Electrodynamics of Continuous Media*, 2nd ed., Course of Theoretical Physics, Vol. 8 (Pergamon Press, Oxford, 1984).

[27] R. C. O'Handley, *Modern Magnetic Materials* (John Wiley & Sons, Inc., 2000).

[28] T. Gilbert, "A Phenomenological Theory of Damping in Ferromagnetic Materials," IEEE Trans. Magn. **40**, 3443 (2004).

[29] V. Kamberský, "On the Landau-Lifshitz relaxation in ferromagnetic metals," Can. J. Phys. **48**, 2906 (1970).

[30] V. Kamberský, "On ferromagnetic resonance damping in metals," Czechoslov. J. Phys. **26**, 1366 (1976).

[31] V. Kamberský, "Spin-orbital Gilbert damping in common magnetic metals," Phys. Rev. B **76**, 134416 (2007).

[32] K. Gilmore, M. D. Stiles, J. Seib, D. Steiauf, and M. Fähnle, "Anisotropic damping of the magnetization dynamics in Ni, Co, and Fe," Phys. Rev. B **81**, 174414 (2010).

[33] T. Qu and R. H. Victora, "Dependence of Kambersky damping on Fermi level and spin orientation," J. Appl. Phys. **115**, 17C506 (2014).

[34] V. Korenman and R. E. Prange, "Anomalous Damping of Spin Waves in Magnetic Metals," Phys. Rev. B **6**, 2769 (1972).

[35] M. A. W. Schoen, D. Thonig, M. L. Schneider, T. J. Silva, H. T. Nembach, O. Eriksson, O. Karis, and J. M. Shaw, "Ultra-low magnetic damping of a metallic ferromagnet," Nat. Phys. **12**, 839 (2016).

[36] B. Khodadadi, A. Rai, A. Sapkota, A. Srivastava, B. Nepal, Y. Lim, D. A. Smith, C. Mewes, S. Budhathoki, A. J. Hauser, M. Gao, J.-F. Li, D. D. Viehland, Z. Jiang, J. J. Heremans, P. V. Balachandran, T. Mewes, and S. Emori, "Conductivitylike Gilbert Damping due to Intraband Scattering in Epitaxial Iron," Phys. Rev. Lett. **124**, 157201 (2020).

[37] K. Gilmore, Y. U. Idzerda, and M. D. Stiles, "Spin-orbit precession damping in transition metal ferromagnets (invited)," J. Appl. Phys. **103**, 07D303 (2008).

[38] S. S. Kalarickal, P. Krivosik, M. Wu, C. E. Patton, M. L. Schneider, P. Kabos, T. J. Silva, and J. P. Nibarger, "Ferromagnetic resonance linewidth in metallic thin films: Comparison of measurement methods," J. Appl. Phys. **99**, 093909 (2006).

[39] I. Harward, T. O'Keevan, A. Hutchison, V. Zagorodnii, and Z. Celinski, "A broadband ferromagnetic resonance spectrometer to measure thin films up to 70 GHz," Rev. Sci. Instrum. **82**, 095115 (2011).

[40] E. Montoya, T. McKinnon, A. Zamani, E. Girt, and B. Heinrich, "Broadband ferromagnetic resonance system and methods for ultrathin magnetic films," J. Magn. Magn. Mater. **356**, 12 (2014).

[41] I. S. Maksymov and M. Kostylev, "Broadband stripline ferromagnetic resonance spectroscopy of ferromagnetic films, multilayers and nanostructures," Phys. E Low-dimensional Syst. Nanostructures **69**, 253 (2015).

[42] T. J. Silva, H. T. Nembach, J. M. Shaw, B. Doyle, K. Oguz, K. O'Brien, and M. Doczy, "Characterization of Magnetic Nanostructures for Spin-Torque Memory Applications with Macro- and Microscale Ferromagnetic Resonance," in *Metrology and Diagnostic Techniques for Nanoelectronics*, edited by Z. Ma and D. G. Seiler (Pan Stanford Publishing Pte. Ltd., Singapore, 2016) Chap. 16.

[43] D. Steiauf and M. Fähnle, "Damping of spin dynamics in nanostructures: An ab initio study," Phys. Rev. B **72**, 064450 (2005).

[44] D. Ralph and M. Stiles, "Spin transfer torques," J. Magn. Magn. Mater. **320**, 1190 (2008).

[45] S. Mankovsky, D. Ködderitzsch, G. Woltersdorf, and H. Ebert, "First-principles calculation of the Gilbert damping parameter via the linear response formalism with application to magnetic transition metals and alloys," Phys. Rev. B **87**, 014430 (2013).

[46] R. Arias and D. L. Mills, "Extrinsic contributions to the ferromagnetic resonance response of ultrathin films," Phys. Rev. B **60**, 7395 (1999).

[47] R. D. McMichael and P. Krivosik, "Classical Model of Extrinsic Ferromagnetic Resonance Linewidth in Ultrathin Films," IEEE Trans. Magn. **40**, 2 (2004).

[48] M. A. W. Schoen, J. M. Shaw, H. T. Nembach, M. Weiler, and T. J. Silva, "Radiative damping in waveguide-based ferromagnetic resonance measured via analysis of perpendicular standing spin waves in sputtered permalloy films," Phys. Rev. B **92**, 184417 (2015).

[49] G. Woltersdorf and B. Heinrich, "Two-magnon scattering in a self-assembled nanoscale network of misfit dislocations," Phys. Rev. B **69**, 184417 (2004).

[50] S. Mizukami, D. Watanabe, M. Oogane, Y. Ando, Y. Miura, M. Shirai, and

T. Miyazaki, "Low damping constant for Co_2FeAl Heusler alloy films and its correlation with density of states," J. Appl. Phys. **105**, 07D306 (2009).

[51] S.-Z. Qiao, Q.-N. Ren, R.-R. Hao, H. Zhong, Y. Kang, S.-S. Kang, Y.-F. Qin, S.-Y. Yu, G.-B. Han, S.-S. Yan, and L.-M. Mei, "Broad-Band FMR Linewidth of Co_2MnSi Thin Films with Low Damping Factor: The Role of Two-Magnon Scattering," Chinese Phys. Lett. **33**, 047601 (2016).

[52] W. K. Peria, T. A. Peterson, A. P. McFadden, T. Qu, C. Liu, C. J. Palmstrøm, and P. A. Crowell, "Interplay of large two-magnon ferromagnetic resonance linewidths and low Gilbert damping in Heusler thin films," Phys. Rev. B **101**, 134430 (2020).

[53] Y. Cui, J. Lu, S. Schäfer, B. Khodadadi, T. Mewes, M. Osofsky, and S. A. Wolf, "Magnetic damping and spin polarization of highly ordered B2 Co_2FeAl thin films," J. Appl. Phys. **116**, 073902 (2014).

[54] A. Kumar, F. Pan, S. Husain, S. Akansel, R. Brucas, L. Bergqvist, S. Chaudhary, and P. Svedlindh, "Temperature-dependent Gilbert damping of Co_2FeAl thin films with different degree of atomic order," Phys. Rev. B **96**, 224425 (2017).

[55] M. Oogane, A. P. McFadden, K. Fukuda, M. Tsunoda, Y. Ando, and C. J. Palmstrøm, "Low magnetic damping and large negative anisotropic magnetoresistance in half-metallic $Co_{2-x}Mn_{1+x}Si$ Heusler alloy films grown by molecular beam epitaxy," Appl. Phys. Lett. **112**, 262407 (2018).

[56] C. Guillemard, S. Petit-Watelot, L. Pasquier, D. Pierre, J. Ghanbaja, J.-C. Rojas-Sánchez, A. Bataille, J. Rault, P. Le Fèvre, F. Bertran, and S. Andrieu, "Ultralow Magnetic Damping in Co_2Mn-Based Heusler Compounds: Promising Materials for Spintronics," Phys. Rev. Appl. **11**, 064009 (2019).

[57] K. Zakeri, J. Lindner, I. Barsukov, R. Meckenstock, M. Farle, U. von Hörsten, H. Wende, W. Keune, J. Rocker, S. S. Kalarickal, K. Lenz, W. Kuch, K. Baberschke, and Z. Frait, "Spin dynamics in ferromagnets: Gilbert damping and two-magnon scattering," Phys. Rev. B **76**, 104416 (2007).

[58] H. Kurebayashi, T. D. Skinner, K. Khazen, K. Olejník, D. Fang, C. Ciccarelli, R. P. Campion, B. L. Gallagher, L. Fleet, A. Hirohata, and A. J. Ferguson, "Uniaxial anisotropy of two-magnon scattering in an ultrathin epitaxial Fe layer on GaAs," Appl. Phys. Lett. **102**, 062415 (2013).

[59] P. Krivosik, N. Mo, S. Kalarickal, and C. E. Patton, "Hamiltonian formalism for two magnon scattering microwave relaxation: Theory and applications," J. Appl. Phys. **101**, 083901 (2007).

[60] S. S. Kalarickal, P. Krivosik, J. Das, K. S. Kim, and C. E. Patton, "Microwave damping in polycrystalline Fe-Ti-N films: Physical mechanisms and correlations with composition and structure," Phys. Rev. B **77**, 054427 (2008).

[61] J. R. Eshbach and R. W. Damon, "Surface Magnetostatic Modes and Surface Spin Waves," Phys. Rev. **118**, 1208 (1960).

[62] T. Kubota, J. Hamrle, Y. Sakuraba, O. Gaier, M. Oogane, A. Sakuma, B. Hillebrands, K. Takanashi, and Y. Ando, "Structure, exchange stiffness, and magnetic anisotropy of $Co_2MnAl_xSi_{1-x}$ Heusler compounds," J. Appl. Phys. **106**, 113907 (2009).

[63] O. Gaier, J. Hamrle, S. Trudel, B. Hillebrands, H. Schneider, and G. Jakob, "Exchange stiffness in the Co_2FeSi Heusler compound," J. Phys. D. Appl. Phys. **42**, 29 (2009).

[64] L. Chen, S. Mankovsky, S. Wimmer, M. A. W. Schoen, H. S. Körner, M. Kronseder, D. Schuh, D. Bougeard, H. Ebert, D. Weiss, and C. H. Back, "Emergence of anisotropic Gilbert damping in ultrathin Fe layers on GaAs(001)," Nat. Phys. **14**, 490 (2018).

[65] Y. Li, F. Zeng, S. S.-L. Zhang, H. Shin, H. Saglam, V. Karakas, O. Ozatay, J. E. Pearson, O. G. Heinonen, Y. Wu, A. Hoffmann, and W. Zhang, "Giant Anisotropy of Gilbert Damping in Epitaxial CoFe Films," Phys. Rev. Lett. **122**, 117203 (2019).

[66] J. Sinova, S. O. Valenzuela, J. Wunderlich, C. H. Back, and T. Jungwirth, "Spin Hall effects," Rev. Mod. Phys. **87**, 1213 (2015).

[67] A. Manchon, J. Železný, I. M. Miron, T. Jungwirth, J. Sinova, A. Thiaville, K. Garello, and P. Gambardella, "Current-induced spin-orbit torques in ferromagnetic and antiferromagnetic systems," Rev. Mod. Phys. **91**, 035004 (2019).

[68] F. Hellman, A. Hoffmann, Y. Tserkovnyak, G. S. D. Beach, E. E. Fullerton, C. Leighton, A. H. MacDonald, D. C. Ralph, D. A. Arena, H. A. Dürr, P. Fischer, J. Grollier, J. P. Heremans, T. Jungwirth, A. V. Kimel, B. Koopmans, I. N. Krivorotov, S. J. May, A. K. Petford-Long, J. M. Rondinelli, N. Samarth, I. K. Schuller, A. N. Slavin, M. D. Stiles, O. Tchernyshyov, A. Thiaville, and B. L. Zink, "Interface-induced phenomena in magnetism," Rev. Mod. Phys. **89**, 025006 (2017).

[69] J.-M. Beaujour, D. Ravelosona, I. Tudosa, E. E. Fullerton, and A. D. Kent, "Ferromagnetic resonance linewidth in ultrathin films with perpendicular magnetic anisotropy," Phys. Rev. B **80**, 180415 (2009).

[70] W. K. Peria, H. Yu, S. Lee, I. Takeuchi, and P. A. Crowell, "Two-magnon frequency-pulling effect in ferromagnetic resonance," Appl. Phys. Lett. **117**, 172401 (2020).

[71] M. Farle, "Ferromagnetic resonance of ultrathin metallic layers," Reports Prog. Phys. **61**, 755 (1998).

[72] D. B. Gopman, V. Sampath, H. Ahmad, S. Bandyopadhyay, and J. Atulasimha, "Static and Dynamic Magnetic Properties of Sputtered Fe–Ga Thin Films," IEEE Trans. Magn. **53**, 1 (2017).

[73] M. J. Hurben and C. E. Patton, "Theory of two magnon scattering microwave relaxation and ferromagnetic resonance linewidth in magnetic thin films," J. Appl. Phys. **83**, 4344 (1998).

[74] A. Y. Dobin and R. H. Victora, "Surface Roughness Induced Extrinsic Damping in Thin Magnetic Films," Phys. Rev. Lett. **92**, 257204 (2004).

[75] A. Azevedo, A. B. Oliveira, F. M. de Aguiar, and S. M. Rezende, "Extrinsic contributions to spin-wave damping and renormalization in thin $Ni_{50}Fe_{50}$ films," Phys. Rev. B **62**, 5331 (2000).

[76] K. An, A. N. Litvinenko, R. Kohno, A. A. Fuad, V. V. Naletov, L. Vila, U. Ebels, G. de Loubens, H. Hurdequint, N. Beaulieu, J. Ben Youssef, N. Vukadinovic, G. E. W. Bauer, A. N. Slavin, V. S. Tiberkevich, and O. Klein, "Coherent long-range transfer of angular momentum between magnon Kittel modes by phonons," Phys. Rev. B **101**, 060407 (2020).

[77] A. Rückriegel and R. A. Duine, "Long-Range Phonon Spin Transport in Ferromagnet–Nonmagnetic Insulator Heterostructures," Phys. Rev. Lett. **124**, 117201 (2020).

[78] B. Casals, N. Statuto, M. Foerster, A. Hernández-Mínguez, R. Cichelero, P. Manshausen, A. Mandziak, L. Aballe, J. M. Hernàndez, and F. Macià, "Generation and Imaging of Magnetoacoustic Waves over Millimeter Distances," Phys. Rev. Lett. **124**, 137202 (2020).

[79] M. Weiler, L. Dreher, C. Heeg, H. Huebl, R. Gross, M. S. Brandt, and S. T. B. Goennenwein, "Elastically Driven Ferromagnetic Resonance in Nickel Thin Films," Phys. Rev. Lett. **106**, 117601 (2011).

[80] H. Suhl, "Theory of the magnetic damping constant," IEEE Trans. Magn. **34**, 1834 (1998).

[81] E. Rossi, O. G. Heinonen, and A. H. MacDonald, "Dynamics of magnetization coupled to a thermal bath of elastic modes," Phys. Rev. B **72**, 174412 (2005).

[82] C. Vittoria, S. D. Yoon, and A. Widom, "Relaxation mechanism for ordered magnetic materials," Phys. Rev. B **81**, 014412 (2010).

[83] S. Streib, H. Keshtgar, and G. E. Bauer, "Damping of Magnetization Dynamics by Phonon Pumping," Phys. Rev. Lett. **121**, 027202 (2018).

[84] W. K. Peria, X. Wang, H. Yu, S. Lee, I. Takeuchi, and P. A. Crowell, "Magnetoelastic Gilbert damping in magnetostrictive $Fe_{0.7}Ga_{0.3}$ thin films," Phys. Rev. B **103**, L220403 (2021).

[85] A. Rückriegel, P. Kopietz, D. A. Bozhko, A. A. Serga, and B. Hillebrands, "Magnetoelastic modes and lifetime of magnons in thin yttrium iron garnet films," Phys. Rev. B **89**, 184413 (2014).

[86] L. D. Landau and E. M. Lifshitz, *Theory of Elasticity*, 3rd ed., Course of Theoretical Physics, Vol. 7 (Pergamon Press, Oxford, 1986).

[87] J. R. Hattrick-Simpers, D. Hunter, C. M. Craciunescu, K. S. Jang, M. Murakami, J. Cullen, M. Wuttig, I. Takeuchi, S. E. Lofland, L. Benderksy, N. Woo, R. B. Van Dover, T. Takahashi, and Y. Furuya, "Combinatorial investigation of magnetostriction in Fe–Ga and Fe–Ga–Al," Appl. Phys. Lett. **93**, 102507 (2008).

[88] C. Zener, "Internal Friction in Solids II. General Theory of Thermoelastic Internal Friction," Phys. Rev. **53**, 90 (1938).

[89] M. Ye, A. Brockmeyer, P. E. Wigen, and H. Dötsch, "Magnetoelastic Resonances in Epitaxial Garnet Films," J. Phys. Colloques **49**, C8 (1988).

[90] R. C. Hall, "Magnetic Anisotropy and Magnetostriction of Ordered and Disordered Cobalt-Iron Alloys," J. Appl. Phys. **31**, S157 (1960).

[91] H. Bömmel and K. Dransfeld, "Excitation of Hypersonic Waves by Ferromagnetic Resonance," Phys. Rev. Lett. **3**, 83 (1959).

[92] M. H. Seavey, "Phonon generation by magnetic films," Proc. IEEE **53**, 1387 (1965).

[93] R. Weber, "Magnon-Phonon Coupling in Metallic Films," Phys. Rev. **169**, 451 (1968).

[94] J. V. Jäger, A. V. Scherbakov, T. L. Linnik, D. R. Yakovlev, M. Wang, P. Wadley, V. Holy, S. A. Cavill, A. V. Akimov, A. W. Rushforth, and M. Bayer, "Picosecond inverse magnetostriction in galfenol thin films," Appl. Phys. Lett. **103**, 032409 (2013).

[95] J. V. Jäger, A. V. Scherbakov, B. A. Glavin, A. S. Salasyuk, R. P. Campion, A. W. Rushforth, D. R. Yakovlev, A. V. Akimov, and M. Bayer, "Resonant driving of

magnetization precession in a ferromagnetic layer by coherent monochromatic phonons," Phys. Rev. B **92**, 020404 (2015).

[96] J. Holanda, D. S. Maior, A. Azevedo, and S. M. Rezende, "Detecting the phonon spin in magnon–phonon conversion experiments," Nat. Phys. **14**, 500 (2018).

[97] C. Zhao, Y. Li, Z. Zhang, M. Vogel, J. E. Pearson, J. Wang, W. Zhang, V. Novosad, Q. Liu, and A. Hoffmann, "Phonon Transport Controlled by Ferromagnetic Resonance," Phys. Rev. Appl. **13**, 054032 (2020).

[98] D.-L. Zhang, J. Zhu, T. Qu, D. M. Lattery, R. H. Victora, X. Wang, and J.-P. Wang, "High-frequency magnetoacoustic resonance through strain-spin coupling in perpendicular magnetic multilayers," Sci. Adv. **6**, eabb4607 (2020).

[99] X. Zhang, G. E. W. Bauer, and T. Yu, "Unidirectional Pumping of Phonons by Magnetization Dynamics," Phys. Rev. Lett. **125**, 77203 (2020).

[100] S. M. Rezende, D. S. Maior, O. Alves Santos, and J. Holanda, "Theory for phonon pumping by magnonic spin currents," Phys. Rev. B **103**, 144430 (2021).

[101] S. Hashimoto, Y. Ochiai, and K. Aso, "Perpendicular magnetic anisotropy and magnetostriction of sputtered Co/Pd and Co/Pt multilayered films," J. Appl. Phys. **66**, 4909 (1989).

[102] Z. R. Tadisina, A. Natarajarathinam, B. D. Clark, A. L. Highsmith, T. Mewes, S. Gupta, E. Chen, and S. Wang, "Perpendicular magnetic tunnel junctions using Co-based multilayers," J. Appl. Phys. **107**, 09C703 (2010).

[103] A. Natarajarathinam, R. Zhu, P. B. Visscher, and S. Gupta, "Perpendicular magnetic tunnel junctions based on thin CoFeB free layer and Co-based multilayer synthetic antiferromagnet pinned layers," J. Appl. Phys. **111**, 07C918 (2012).

[104] Y.-J. Chang, A. Canizo-Cabrera, V. Garcia-Vazquez, Y.-H. Chang, and T.-h. Wu, "Perpendicular magnetic tunnel junctions with synthetic antiferromagnetic pinned layers based on [Co/Pd] multilayers," J. Appl. Phys. **113**, 17B909 (2013).

[105] R. L. Comstock and R. C. LeCraw, "Generation of Microwave Elastic Vibrations in a Disk by Ferromagnetic Resonance," J. Appl. Phys. **34**, 3022 (1963).

[106] T. Sato, W. Yu, S. Streib, and G. E. W. Bauer, "Dynamic magnetoelastic boundary conditions and the pumping of phonons," Phys. Rev. B **104**, 014403 (2021).

[107] M. H. Seavey, "Boundary-Value Problem for Magnetoelastic Waves in a Metallic Film," Phys. Rev. **170**, 560 (1968).

[108] A. I. Bezuglyj, V. A. Shklovskij, V. V. Kruglyak, and R. V. Vovk, "Temperature dependence of the magnon-phonon energy relaxation time in a ferromagnetic insulator," Phys. Rev. B **100**, 214409 (2019).

[109] M. Seavey, "Microwave Phonon Generation by Thin Magnetic Films," IEEE Trans. Ultrason. Eng. **10**, 49 (1963).

[110] C. F. Kooi, "Interaction of Phonons and Spin Waves," Phys. Rev. **131**, 1070 (1963).

[111] T. Kobayashi, R. C. Barker, J. L. Bleustein, and A. Yelon, "Ferromagnetoelastic Resonance in Thin Films. I. Formal Treatment," Phys. Rev. B **7**, 3273 (1973).

[112] C. Kittel and J. H. Van Vleck, "Theory of the Temperature Dependence of the Magnetoelastic Constants of Cubic Crystals," Phys. Rev. **118**, 1231 (1960).

[113] E. R. Callen and H. B. Callen, "Static Magnetoelastic Coupling in Cubic Crystals," Phys. Rev. **130**, 2600 (1963).

[114] H. Callen and E. Callen, "The present status of the temperature dependence of magnetocrystalline anisotropy, and the $l(l+1)/2$ power law," J. Phys. Chem. Solids **27**, 1271 (1966).

[115] R. V. Mikhaylovskiy, E. Hendry, and V. V. Kruglyak, "Negative permeability due to exchange spin-wave resonances in thin magnetic films with surface pinning," Phys. Rev. B **82**, 195446 (2010).

[116] J. M. Shaw, T. J. Silva, M. L. Schneider, and R. D. McMichael, "Spin dynamics and mode structure in nanomagnet arrays: Effects of size and thickness on linewidth and damping," Phys. Rev. B **79**, 184404 (2009).

[117] H. T. Nembach, J. M. Shaw, T. J. Silva, W. L. Johnson, S. A. Kim, R. D. McMichael, and P. Kabos, "Effects of shape distortions and imperfections on mode frequencies and collective linewidths in nanomagnets," Phys. Rev. B **83**, 094427 (2011).

[118] H. T. Nembach, J. M. Shaw, C. T. Boone, and T. J. Silva, "Mode- and size-dependent Landau-Lifshitz damping in magnetic nanostructures: Evidence for nonlocal damping," Phys. Rev. Lett. **110**, 1 (2013).

[119] C. Berk, M. Jaris, W. Yang, S. Dhuey, S. Cabrini, and H. Schmidt, "Strongly coupled magnon–phonon dynamics in a single nanomagnet," Nat. Commun. **10**, 2652 (2019).

[120] P. Webster, "Magnetic and chemical order in Heusler alloys containing cobalt and manganese," J. Phys. Chem. Solids **32**, 1221 (1971).

[121] Y. Takamura, R. Nakane, and S. Sugahara, "Analysis of $L2_1$-ordering in full-Heusler Co_2FeSi alloy thin films formed by rapid thermal annealing," J. Appl. Phys. **105**, 07B109 (2009).

[122] Y. Takamura, R. Nakane, and S. Sugahara, "Quantitative analysis of atomic disorders in full-Heusler Co_2FeSi alloy thin films using x-ray diffraction with Co $K\alpha$ and Cu $K\alpha$ sources," J. Appl. Phys. **107**, 09B111 (2010).

[123] S. H. Simon, *The Oxford Solid State Basics*, 1st ed. (Oxford University Press, Oxford, 2013).

[124] E. Prince, ed., *International Tables for Crystallography, Volume C*, 3rd ed. (Springer Dordrecht, 2004).

[125] B. Pradines, R. Arras, I. Abdallah, N. Biziere, and L. Calmels, "First-principles calculation of the effects of partial alloy disorder on the static and dynamic magnetic properties of Co_2MnSi," Phys. Rev. B **95**, 094425 (2017).

[126] L. Caretta, S.-H. Oh, T. Fakhrul, D.-K. Lee, B. H. Lee, S. K. Kim, C. A. Ross, K.-J. Lee, and G. S. D. Beach, "Relativistic kinematics of a magnetic soliton," Science **370**, 1438 (2020).

[127] P. Hansen, K. Witter, and W. Tolksdorf, "Magnetic and magneto-optic properties of lead- and bismuth-substituted yttrium iron garnet films," Phys. Rev. B **27**, 6608 (1983).

[128] L. Soumah, N. Beaulieu, L. Qassym, C. Carrétéro, E. Jacquet, R. Lebourgeois, J. Ben Youssef, P. Bortolotti, V. Cros, and A. Anane, "Ultra-low damping insulating magnetic thin films get perpendicular," Nat. Commun. **9**, 3355 (2018).

[129] P. He, X. Ma, J. W. Zhang, H. B. Zhao, G. Lüpke, Z. Shi, and S. M. Zhou, "Quadratic Scaling of Intrinsic Gilbert Damping with Spin-Orbital Coupling in $L1_0$ FePdPt Films: Experiments and *Ab Initio* Calculations," Phys. Rev. Lett. **110**, 077203 (2013).

[130] S. Iihama, A. Sakuma, H. Naganuma, M. Oogane, T. Miyazaki, S. Mizukami, and Y. Ando, "Low precessional damping observed for $L1_0$-ordered FePd epitaxial thin films with large perpendicular magnetic anisotropy," Appl. Phys. Lett. **105**, 142403 (2014).

[131] S. Iihama, A. Sakuma, H. Naganuma, M. Oogane, S. Mizukami, and Y. Ando, "Influence of $L1_0$ order parameter on Gilbert damping constants for FePd thin films investigated by means of time-resolved magneto-optical Kerr effect," Phys. Rev. B **94**, 174425 (2016).

[132] D. Zhang, D. Huang, R. J. Wu, D. Lattery, J. Liu, X. Wang, D. B. Gopman, K. A. Mkhoyan, J.-P. Wang, and X. Wang, "Low Gilbert damping and high thermal stability of Ru-seeded $L1_0$-phase FePd perpendicular magnetic thin films at elevated temperatures," Appl. Phys. Lett. **117**, 082405 (2020).

[133] X. Wang, S. Krylyuk, D. Josell, D. Zhang, J.-P. Wang, and D. B. Gopman, "Effect of Oblique Versus Normal Deposition on the Properties of Perpendicularly Magnetized $L1_0$ FePd Thin Films," IEEE Magn. Lett. **11**, 1 (2020).

Appendix A

Symbols, Acronyms, and Sample Naming Conventions

This appendix defines symbols, acronyms, and sample naming conventions that are used frequently in this thesis.

A.1 Symbols

Table A.1: Symbols

Symbol	Quantity (units)
α	Gilbert damping (unitless)
α_{me}	Magnetoelastic Gilbert damping (unitless)
ΔH_0	Inhomogeneous broadening (magnetic field)
g	Landé g-factor (unitless)
γ	Gyromagnetic ratio (frequency/magnetic field)
M_s	Saturation magnetization (moment/volume)
$4\pi M_{eff}$	Net perpendicular anisotropy field of a thin film (magnetic field)
$H_{k,eff}$	Equivalent to $4\pi M_{eff}$; commonly used for PMA materials (magnetic field)

Continued on next page

Table A.1 – continued from previous page

Symbol	Quantity (units)
ΔH	Full-width-at-half-maximum FMR linewidth (magnetic field)
ΔH_{FWHM}	Used interchangeably with ΔH (magnetic field)
ΔH_{TMS}	TMS contribution to the FMR linewidth (magnetic field)
ξ	Defect correlation length, esp. with respect to TMS (length)
(hkl)	Reciprocal lattice plane with Miller indices h, k, and l
$[hkl]$	The direction perpendicular to the (hkl) reciprocal lattice plane
$\langle hkl \rangle$	The family of directions equivalent by crystal symmetry to the $[hkl]$ direction

A.2 Acronyms

Table A.2: Acronyms

Acronym	Meaning
FMR	Ferromagetic Resonance
IP	In Plane
PMA	Perpendicular Magnetic Anisotropy
PP	Perpendicular to Plane
SAF	Synthetic Antiferromagnet
TMS	Two-Magnon Scattering
VSM	Vibrating-sample magnetometry
XRD	X-ray diffraction
XRR	X-ray reflectivity

Table A.3: Sample Names

Sample Name	Description
BiYIG	$Bi_{0.7}Y_{2.3}Fe_5O_{12}$
CFA	Co_2FeAl
CMA	Co_2MnAl
CMS	Co_2MnSi
Co/Pd	$[Co(0.8\ nm)/Pd(1.5\ nm]_n$ (n is the number of Co/Pd repetitions)

Appendix B

Determination of Chemical Order in Full Heusler Compounds Using X-Ray Scattering

B.1 Introduction

In this appendix we will lay out a summary of how the chemical order was determined for the Heusler films in Chapter 2, and also outline an approach that is more sophisticated but ultimately unnecessary. This approach is based on the "Webster model" [120], and was expanded in Refs. [121, 122]. Ref. [3] is also good for a general understanding. Throughout we will only refer to full Heusler compounds with stoichiometry X_2YZ, but this approach can be easily extended to half-Heuslers (XYZ) as well.

Another note on nomenclature: A2 means X-Y-Z disorder, B2 means Y-Z disorder, and $D0_3$ means X-Y disorder. This type of chemical disorder is often referred to as antisite disorder, where atoms randomly exchange lattice sites with another atomic species.

B.2 Rough Method

This initial approach classifies $D0_3$ as being under the A2 umbrella which is not, strictly speaking, correct. It is correct, however, in the limit that the sample is "at least B2,"

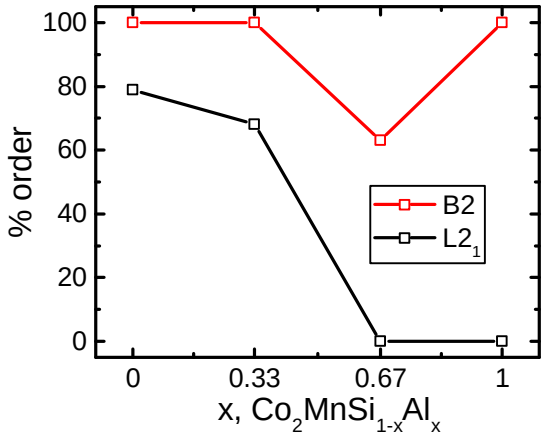

Figure B.1: Percent order of B2 (red) and $L2_1$ (black) in $Co_2MnSi_{1-x}Al_x$.

meaning that the only disordering is between Y and Z atoms. Full A2 disorder refers to when each site is randomly occupied (weighted by overall chemical composition). It is called this because the crystal structure becomes bcc with a single-atom basis when all sites are equivalent, and this is what A2 means in Strukturbericht notation.

When there is only B2 disorder, it is correct to quantify the amount of $L2_1$ order via the relative intensities of the (111) and (202) families of peaks. Fig. B.1 shows the results using this technique for the $Co_2MnSi_{1-x}Al_x$ series, which were calculated using relative intensities for Cu $K\alpha$ radiation.

B.3 Rigorous Method

The more rigorous approach takes into account all possible forms of antisite disorder. The ordered full Heusler crystal structure is $L2_1$ (Strukturbericht notation). The relevant forms of disorder are A2 (bcc), B2 (CsCl bcc), and $D0_3$ (Fe_3Al bcc). See Fig. B.3(a-c) for an illustration.

For A2 disorder, which is when all lattice sites are equivalent and hence the most disordered, the (002) reciprocal lattice peak is extinguished. It should be noted that the (002) peak of the $L2_1$ crystal structure can be thought of as the (001) peak of either the A2 or B2 structure since the lattice constant is halved, which can be seen in Fig.

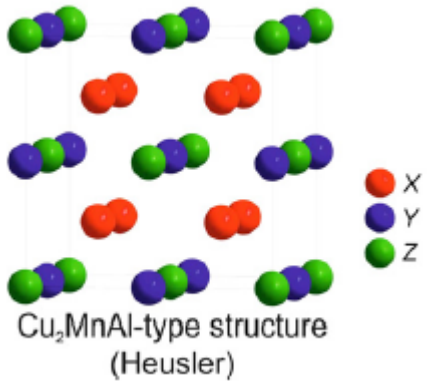

Figure B.2: The $L2_1$ crystal structure for an X_2YZ full Heusler compound. From Ref. [3].

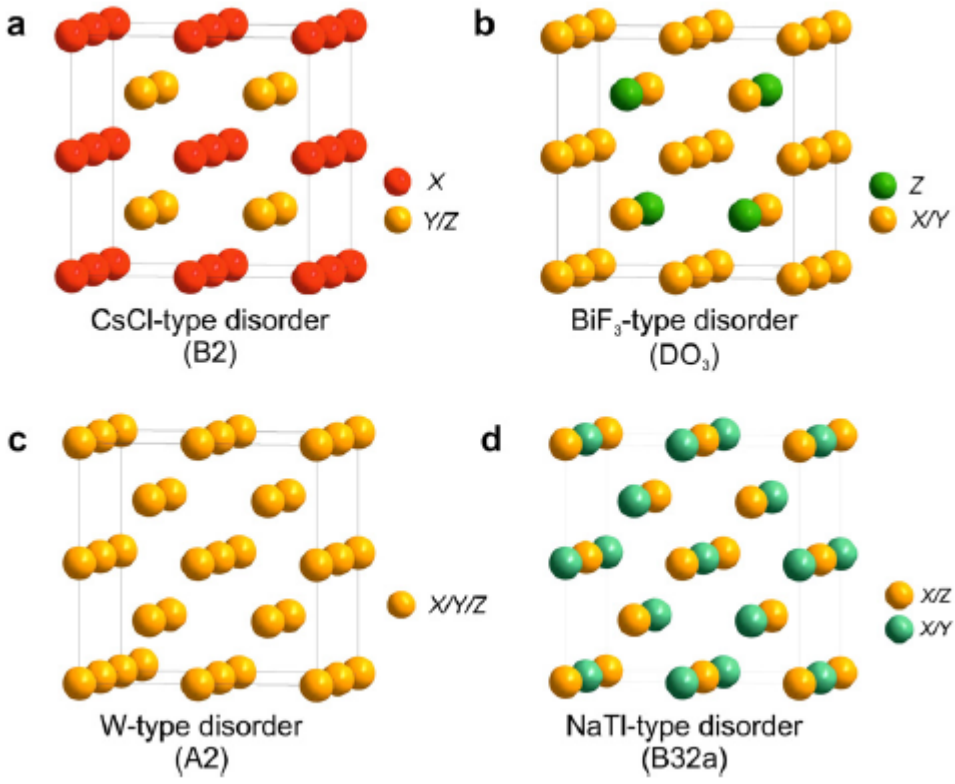

Figure B.3: Types of disorder along with prototypes for the respective lattice type. X_2YZ is the stoichiometry, with X and Y the transition metal atoms. Panel (d) can be ignored for the purposes of discussion. From Ref. [3].

B.3. The (001) peak is extinguished for a bcc crystal, which is shown in Ref. [123] and elsewhere. It is also shown in Ref. [123] that for bcc with a basis (CsCl here) the (001) peak is *not* extinguished. Therefore the presence or absence of the (002) peak can be used to measure the level of A2 disorder. The (002) peak is also extinguished for the $D0_3$ lattice.

B2 disorder, where the Heusler possesses the B2 CsCl-type crystal structure, is probed by the presence or absence of the (111) peak. The (111) peak is extinguished for A2 or B2 disorder. This relates to the fact that the $L2_1$ crystal structure is fcc-based (four interpenetrating fcc lattices), and the (111) peak is present for fcc but not bcc. In Ref. [123] it is shown that

$$F^{bcc}_{(hkl)} \sim 1 + (-1)^{h+k+l} \tag{B.1}$$

which indeed vanishes for $(hkl) = (111)$. From this expression, it can also be seen that the (220) peak will not be extinguished for A2 disorder and is thus insensitive to any of the above forms of disorder.

In Ref. [120], the structure factors, which predict relative peak intensities, are shown to be

$$\begin{aligned} F_{(111)} &= 4|f_Y - f_Z| \\ F_{(200)} &= 4|2f_X - (f_Y + f_Z)| \\ F_{(220)} &= 4|2f_Z + (f_Y + f_Z)| \end{aligned} \tag{B.2}$$

where the f_i are the atomic scattering factors at the incident x-ray wavelength. Atomic scattering factors for 10–30,000 eV can be found in a database managed by Lawrence Berkeley National Lab [1] , but in general the scattering factors will depend on scattering angle and this information is not provided there. See the International Tables for Crystallography, Volume C for more complete information [124]. In Table 6.1.1.1 of Ref. [124], the atomic scattering factors are listed for all atoms of interest as functions of $\sin\theta/\lambda$. We will use the conventions of Ref. [122] in order to describe the disorder present in the system: α is the number of Y(Z) atoms occupying Z(Y) sites per formula unit, β the number of X(Z) atoms on Z(X) sites per formula unit, and γ is the number of X(Y) atoms on Y(X) sites per formula unit. This is summarized in Table B.1. It is then

[1] URL: http://henke.lbl.gov/optical_constants/asf.html

	X sites	Y sites	Z sites
X	$2-\gamma-\beta$	γ	β
Y	γ	$1-\alpha-\gamma$	α
Z	β	α	$1-\alpha-\beta$

Table B.1: Table linking the disorder parameters to the fraction of sites occupied by different atoms.

shown in Ref. [122] that one can account for disorder by replacing the scattering factors in Eqns. B.2 (using Table B.1) via $f_X \rightarrow [(2-\gamma-\beta)f_X + \gamma f_Y + \beta f_Z]/2$, and similarly for f_Y and f_Z (the overall factor of 1/2 is only necessary for the f_X replacement). Eqns. B.2 become

$$\begin{aligned} F_{(111)} &= 4|(1-2\alpha-\beta)(f_Y-f_Z)+(\gamma-\beta)(f_X-f_Y)| \\ F_{(200)} &= 4|(1-2\beta)(f_X-f_Z)+(1-2\gamma)(f_X-f_Y)| \\ F_{(220)} &= 4|2f_Z+(f_Y+f_Z)| \ . \end{aligned} \tag{B.3}$$

The measurable quantity is scattering intensity, given by $I_{(hkl)} = I_0|F_{(hkl)}|^2$. The (220) peak needs to be measured only in order to establish the constant I_0. For Co_2YZ, the scattering factors f_{Co} and f_Y will be nearly equal for Cu $K\alpha$ radiation (1.54 Å). This makes it necessary to measure the relative intensities using both Cu $K\alpha$ radiation *and* Co $K\alpha$ (1.79 Å) radiation, which is the main point of Ref. [122].

The best way to measure peak intensities is by doing a rocking curve. Then the integrated peak intensity can be calculated. You have to integrate the peak rather than just take the amplitude to account for the (likely) possibility that the peak width (full-width-at-half-maximum) will vary among different peaks. An equivalent solution is to normalize the amplitude by the full-width-at-half-maximum (FWHM). To see why this works, consider the following Lorentzian function centered at x_0 with FWHM Γ:

$$f(x) = \frac{\Gamma/2}{(x-x_0)^2+(\Gamma/2)^2} \ . \tag{B.4}$$

The maximum value is $2/\Gamma$, and thus the amplitude scales inversely with the FWHM.

Lastly, it should be noted that the dual-source measurement is probably overkill for the Heusler films in Chapter 2. It has been calculated that even small amounts of $D0_3$ disorder will cause strong changes in quantities like the saturation magnetization and

Gilbert damping–much stronger than is expected for B2 disorder [125]. Our films show good agreement with literature values for $L2_1$-ordered films however—particularly in the case of the saturation magnetization—so we can conclude there is negligible $D0_3$ disorder.

Appendix C

Theory of Two-Magnon Scattering

In this appendix we will walk through part of the derivation of the results used in Chapters 2 and 3 to model the effects of TMS on damping and resonance frequency.

C.1 Introduction

The goal here is to establish the calculations and final working equations that are used to calculate both the two-magnon scattering (TMS) linewidths and line shifts, following Refs. [47, 59, 60]. We will not worry about the initial steps required to diagonalize the Hamiltonian, but more on how to get from the general results of Refs. [47, 59] (MM04, K07, respectively) to the working equations of Ref. [60] (K08; which only include linewidth, but we will generalize to include the line shift).

We ultimately want to reproduce the expression for the field-swept linewidth given in K08 (which we used in [52]), *viz.*,

$$\Delta H_{TMS} = \frac{\gamma^2 H'^2 \xi^2}{d\omega/dH|_{H_{FMR}}} \int d\mathbf{q}\ \Lambda_{0\mathbf{q}} C_{\mathbf{q}}(\xi) \frac{1}{\pi} \frac{\delta\omega/2}{(\omega_0 - \omega_{\mathbf{q}})^2 + (\delta\omega/2)^2}\ , \tag{C.1}$$

where $\delta\omega = (2\alpha\omega/\gamma)(d\omega/dH)$ is the Gilbert frequency linewidth, $C_{\mathbf{q}} = \left[1 + (q\xi)^2\right]^{-3/2}$ is the correlation function, and $\Lambda_{0\mathbf{q}}$ is the magnon coupling strength given by

$$\Lambda_{0\mathbf{q}} = c_1 e_0 e_{\mathbf{q}} + \frac{c_2}{e_0 e_{\mathbf{q}}} + c_3 \left(\frac{e_0}{e_{\mathbf{q}}} + \frac{e_{\mathbf{q}}}{e_0}\right) + c_4\ , \tag{C.2}$$

with $e_{\mathbf{q}}$ the magnon ellipticity:

$$\begin{aligned} e_{\mathbf{q}} &= \sqrt{\frac{H_{xx,\mathbf{q}}}{H_{yy,\mathbf{q}}}} \\ &= \sqrt{\frac{H + Dq^2 + 4\pi M_s N_q}{H + Dq^2 + 4\pi M_s (1 - N_q)\sin^2\theta_{\mathbf{q}}}} \ . \end{aligned} \tag{C.3}$$

Notice we have implicitly defined the x-direction as normal to the plane, and z as the direction of the static magnetization. N_q is the usual wavenumber-dependent demagnetization factor: $N_q = (1-e^{-qd})/qd$. The c_i's are constants and depend on the anisotropy of the individual grains, and for a cubic system are

$$\begin{aligned} c_1 &= \frac{29}{420} \\ c_2 &= \frac{29}{420} \\ c_3 &= \frac{3}{140} \\ c_4 &= \frac{1}{105} \end{aligned} \tag{C.4}$$

K07 primarily uses stiffness fields $H_{ij,\mathbf{q}}$ rather than ellipticities, so a major part of completing the connection between K07 and K08 is making these substitutions.

C.2 Expression for the Complex Scattering Rate

In K07, the following equation of motion is derived for the FMR ($\mathbf{q} = 0$) magnon allowing for interactions with $\mathbf{q} \neq 0$ magnons:

$$i\left(\frac{d}{dt} + \eta_0\right) c_0(t) = \omega_0 c_0(t) + \sum_{\mathbf{q}\neq 0}\left[\widetilde{G}_{0,\mathbf{q}} c_{\mathbf{q}}(t) + \widetilde{F}_{0,\mathbf{q}} c^*_{\mathbf{q}}(t)\right] \ . \tag{C.5}$$

Here $c_0(t)$ represents the amplitude of the FMR mode, ω_0 is the (noninteracting) resonance frequency, and η_0 is its Gilbert relaxation rate. The $\widetilde{G}$'s and $\widetilde{F}$'s come from the canonical transformations and will be defined shortly. The sum over nonzero $\mathbf{q}$, which represents interactions between magnons of different $\mathbf{q}$, is zero in the absence of inhomogeneity. We also need an equation for the nonuniform magnons:

$$i\left(\frac{d}{dt} + \eta_{\mathbf{q}}\right) c_{\mathbf{q}}(t) = \omega_{\mathbf{q}} c_{\mathbf{q}}(t) + \widetilde{G}^*_{0,\mathbf{q}} c_0(t) + \widetilde{F}_{0,\mathbf{q}} c^*_0(t) \ . \tag{C.6}$$

By writing $\bar{c}_0(t) = c_0(t)e^{i\omega_0 t}$, Eq. (C.5) can be combined with Eq. (C.6) to be expressed more clearly as

$$\frac{d\bar{c}_0(t)}{dt} \approx -(\eta_0 + \widetilde{\Gamma}_0)\bar{c}_0(t) \ , \tag{C.7}$$

where $\widetilde{\Gamma}_0$ is defined by

$$\begin{aligned}\widetilde{\Gamma}_0 &= i\sum_{\mathbf{q}\neq 0}\left\{\frac{|\widetilde{G}_{0,\mathbf{q}}|^2}{\omega_0 - \omega_{\mathbf{q}} + i\eta_{\mathbf{q}}} - \frac{|\widetilde{F}_{0,\mathbf{q}}|^2}{\omega_0 + \omega_{\mathbf{q}} + i\eta_{\mathbf{q}}}\right\} \\ &= i\widetilde{\omega}_0 + \widetilde{\eta}_0 \ .\end{aligned} \tag{C.8}$$

It is clear that $\widetilde{\Gamma}_0$ is the complex scattering rate due to TMS—$\widetilde{\omega}_0$ is the line shift and $\widetilde{\eta}_0$ is the TMS frequency linewidth. The goal now will be to show that $\widetilde{\eta}_0$ corresponds to the result in K08 [i.e. Eq. (C.1)].

C.3 Connecting Eq. (C.1) and Eq. (C.8)

First we note that in Eq. (C.8), the terms involving $\widetilde{F}$'s can be ignored since they are off-resonant. We now express $\widetilde{G}_{0,\mathbf{q}}$ in terms of both homogeneous stiffness fields ($H_{ij,\mathbf{q}}$) and inhomogeneous stiffness fields ($\widetilde{h}_{ij}$):

$$\begin{aligned}|\widetilde{G}_{0,\mathbf{q}}|^2 =& \frac{\gamma^4 C_{\mathbf{q}}}{4\omega_{\mathbf{q}}\omega_0}\{\langle\widetilde{h}_{xx}^2\rangle H_{yy,\mathbf{q}}H_{yy,0} + \langle\widetilde{h}_{yy}^2\rangle H_{xx,\mathbf{q}}H_{xx,0} \\ &+ 2\langle\widetilde{h}_{xx}\widetilde{h}_{yy}\rangle(\omega_{\mathbf{q}}\omega_0/\gamma^2) \\ &+ \langle\widetilde{h}_{xy}^2\rangle(H_{xx,\mathbf{q}}H_{yy,0} + H_{yy,\mathbf{q}}H_{xx,0} - 2\omega_{\mathbf{q}}\omega_0/\gamma^2)\} \ .\end{aligned} \tag{C.9}$$

Note that, as usual, $\omega_{\mathbf{q}} = \gamma\sqrt{H_{xx,\mathbf{q}}H_{yy,\mathbf{q}}}$. Then, write $\widetilde{G}_{0,\mathbf{q}}$ in terms of the ellipticities $e_{\mathbf{q}}$ given by Eq. C.3:

$$\begin{aligned}|\widetilde{G}_{0,\mathbf{q}}|^2 =& \frac{\gamma^2 C_{\mathbf{q}}}{4}[\langle\widetilde{h}_{xx}^2\rangle\frac{1}{e_0 e_{\mathbf{q}}} + \langle\widetilde{h}_{yy}^2\rangle e_0 e_{\mathbf{q}} \\ &+ 2\langle\widetilde{h}_{xx}\widetilde{h}_{yy}\rangle \\ &+ \langle\widetilde{h}_{xy}^2\rangle(\frac{e_{\mathbf{q}}}{e_0} + \frac{e_0}{e_{\mathbf{q}}} - 2)] \ .\end{aligned} \tag{C.10}$$

The averages of the inhomogeneity fields, for cubic anisotropy, are given in K07 (and in more detail in MM04) as

$$\begin{aligned}
\langle \widetilde{h}_{xx}^2 \rangle &= \frac{29}{105} H'^2 \\
\langle \widetilde{h}_{yy}^2 \rangle &= \frac{29}{105} H'^2 \\
\langle \widetilde{h}_{xx} \widetilde{h}_{yy} \rangle &= \frac{11}{105} H'^2 \\
\langle \widetilde{h}_{xy}^2 \rangle &= \frac{9}{105} H'^2
\end{aligned} \tag{C.11}$$

which can be substituted into Eq. (C.10), yielding

$$|\widetilde{G}_{0,\mathbf{q}}|^2 = \gamma^2 C_{\mathbf{q}} H'^2 \left[\frac{29}{420} \frac{1}{e_0 e_{\mathbf{q}}} + \frac{29}{420} e_0 e_{\mathbf{q}} + \frac{3}{140} \left(\frac{e_{\mathbf{q}}}{e_0} + \frac{e_0}{e_{\mathbf{q}}} \right) + \frac{1}{105} \right] . \tag{C.12}$$

This can then be written in terms of the c's given by Eq. (C.4):

$$\begin{aligned}
|\widetilde{G}_{0,\mathbf{q}}|^2 &= \gamma^2 C_{\mathbf{q}} H'^2 \left[\frac{c_1}{e_0 e_{\mathbf{q}}} + c_2 e_0 e_{\mathbf{q}} + c_3 \left(\frac{e_{\mathbf{q}}}{e_0} + \frac{e_0}{e_{\mathbf{q}}} \right) + c_4 \right] \\
&= \gamma^2 C_{\mathbf{q}} H'^2 \Lambda_{0\mathbf{q}} \, .
\end{aligned} \tag{C.13}$$

Substituting Eq. (C.12) into Eq. (C.8), we obtain an expression whose real part is identical to Eq. (C.1) [after including the factor of $(d\omega/dH|_{H_{FMR}})^{-1}$ to convert from frequency to field units] and whose imaginary part yields the corresponding frequency shift due to TMS.

Appendix D

Angular Dependence of Damping in Bismuth-Doped Yttrium Iron Garnet Films

Ferrimagnetic garnets have attracted a lot of attention in magnetism for the past half century—with $Y_3Fe_5O_{12}$ (YIG) being the foremost—due to their potential for ultralow damping. More recently, it has become popular to substitute yttrium ions with heavier rare-earth ions (Bi, Tm, Tb, etc.) [126] in order to get PMA due to magnetoelastic anisotropy and epitaxial strain. In this appendix we will focus on the case of Bi-doped YIG, where the exact composition here is $Bi_{0.7}Y_{2.3}Fe_5O_{12}$. The effect of doping YIG with Bi that is germane here is to tune the lattice constant and the magnetostriction simultaneously [127]. The magnetostriction of BiYIG is negative, which means that it must be compressed in the PP direction to have PMA [128]. To impose a compressive strain in the PP direction we grew the BiYIG films ($a \simeq 12.43$ Å) on nonmagnetic $Gd_3Sc_2Ga_3O_{12}(111)$ (GSGG) substrates ($a \simeq 12.55$ Å)[1] using pulsed laser deposition (PLD) at thicknesses below ∼100 nm so that the films experienced a uniform epitaxial strain. (The strain state was confirmed with high-resolution x-ray diffraction.)

The measurements of the FMR linewidths were conducted at room temperature

[1] These can be thought of as scandium-doped $Gd_3Ga_5O_{12}$ (GGG) substrates. The point of doping is to tune the lattice constant—GGG substrates have a smaller lattice constant ($a \simeq 12.37$ Å) than BiYIG and would therefore cause a tensile strain in the PP direction, eliminating the possibility of PMA.

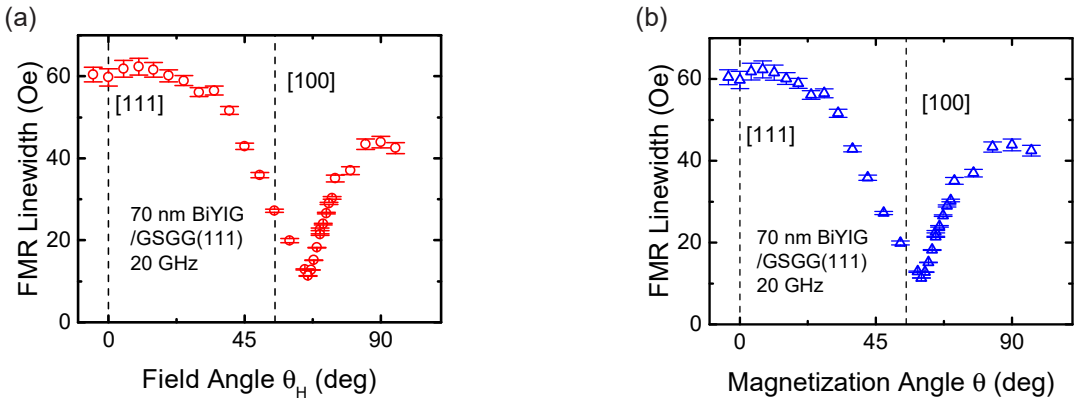

Figure D.1: (a) Ferromagnetic resonance linewidths as a function of the polar angle (angle relative to the film normal) of the applied field θ_H for the 70-nm BiYIG/GSGG(111) film. The [100] and [111] crystal axes corresponding to $\theta_H = 0$ and $\simeq$54.74 degrees, respectively, are indicated on the figure. (b) Ferromagnetic resonance linewidths as a function of magnetization angle. The [100] and [111] crystal axes corresponding to $\theta = 0$ and $\simeq$54.74 degrees, respectively, are indicated on the figure. The magnetization angle was calculated by minimizing the magnetic free energy for a given angle of the applied field.

and the angle of the applied field θ_H (defined in the same way as θ in Fig. 1.2) was varied from the PP orientation to the IP orientation. These data are shown for a 70 nm BiYIG/GSGG(111) film in Fig. D.1(a) at a frequency of 20 GHz. Figure D.1(b) shows the FMR linewidths as a function of magnetization angle θ, which was determined by minimizing the magnetic free energy,

$$F = -\mathbf{M} \cdot \mathbf{H} + K_{u,eff} \sin^2 \theta \ , \tag{D.1}$$

for a fixed applied field angle θ_H. The effective perpendicular anisotropy energy $K_{u,eff}$ was determined by measuring the FMR field as a function of frequency for PP applied fields and fitting to the Kittel formula.

There are two very unusual features in the data shown in Fig. D.1. The first is that the PP FMR linewidths are substantially larger than the IP linewidths. Usually the opposite is true due to the possibility of TMS for IP fields. The second, which will be the focus of this appendix, is the pronounced minimum in the FMR linewidth for $\theta \simeq 55$ to 60 degrees. Typically a maximum is observed at intermediate angles of the magnetization (the precise value being strongly dependent on $K_{u,eff}$) due to field

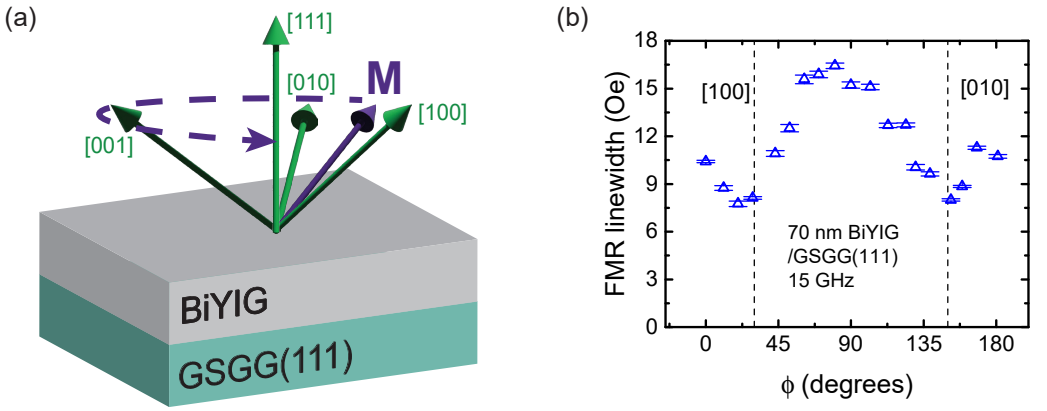

Figure D.2: (a) Schematic of the ϕ-rotation FMR measurement. $\mathbf{M}$ is rotated into the plane by $\sim$55 degrees relative to the film normal and rotated about the [111] axis. This cone of rotation contains three of the six $\langle 100 \rangle$-equivalent axes. (b) FMR linewidths as a function of ϕ corresponding to the configuration in panel (a). The angles $\phi = 30$ degrees and 150 degrees correspond to the [100] and [010] directions, respectively.

dragging (see, e.g., Fig. 8 in Ref. [49] for the case of Fe). This occurs where the FMR field changes most rapidly as a function of θ_H and is essentially inhomogeneous broadening. A minimum in the FMR linewidth—at nearly the same angle of the magnetization—was observed in several other BiYIG films with varying thickness. Another study observed essentially the same behavior in a BiYIG film with similar composition [128], although a satisfactory explanation was not given. The proximity of this minimum to the [100] axis ($\theta = \arccos 1/\sqrt{3} \simeq 54.74°$) suggests that a magnetocrystalline or magnetoelastic anisotropy, which both possess the symmetry of the lattice, play a role.

To test this hypothesis, we measured the FMR linewidth as a function of ϕ (as defined in Fig. 1.2) while keeping θ fixed at the value where the minimum linewidth was observed. Based on the symmetry of the lattice—which is cubic—we expect a threefold symmetry, as shown in Fig. D.2(a).[2] Figure D.2(b) confirms our hypothesis of a threefold symmetry, where two distinct minima are observed approximately 120° apart.

The last thing we will demonstrate in this appendix is the effect of changing the film's orientation on the position of the linewidth minimum. GSGG substrates are

[2] A sixfold symmetry would be observed if the magnetization were lying in the film plane, since there are six equivalent directions perpendicular to [111].

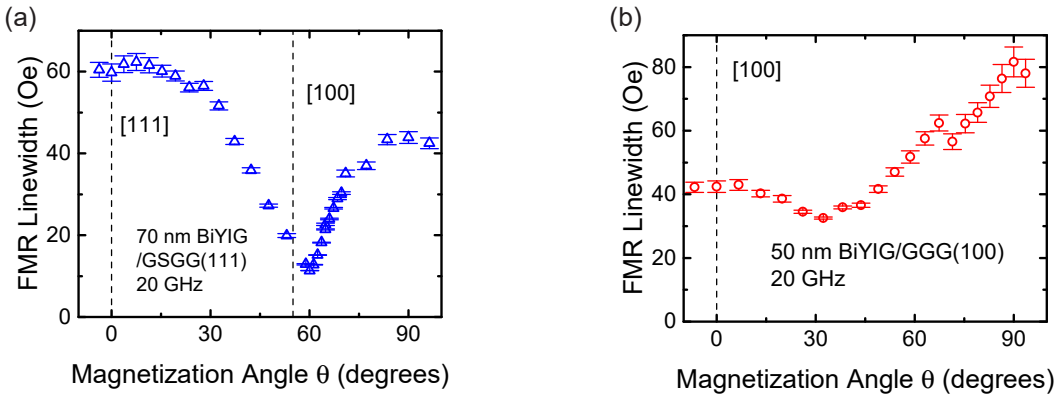

Figure D.3: Ferromagnetic resonance linewidths for both (a) (111) and (b) (100) BiYIG film orientations.

not commercially available in orientations other than (111), so we chose to grow a BiYIG film on a GGG(100) substrate. (This film, as a result, does not have PMA.) Figure D.3 shows a comparison between a (111)-oriented film (a) and a (100)-oriented film. The minimum clearly moves to lower magnetization angle ($\simeq 30^\circ$ and is much less pronounced. Furthermore, the IP linewidths are substantially larger than the PP linewidths.

The mystery of this linewidth minimum and the dependence on crystallographic orientation is the subject of ongoing work. There is a case to be made that this is related to the phonon pumping discussed in Chapter 5. The fact that the linewidths are larger for PP fields then IP fields is consistent with this. We would also expect the effect to be broadband due to the strong elastic coupling between the film and substrate, a result of their chemical similarity. It is a problem of technological importance, particularly for the case of spin wave devices. We would like to have PMA materials for spin wave devices that are low loss when the magnetization is perpendicular to the plane; narrow linewidths at oblique angles are not useful for applications.

Appendix E

Magnetization Dynamics in FePd-Based Synthetic Antiferromagnets

FePd alloys have attracted a lot of interest recently due to predictions of low damping and the existence of intrinsic or "bulk" PMA [129–133]. In this appendix we will look at what happens to the damping in synthetic antiferromagnets made from FePd films. Synthetic antiferromagnets (SAFs) are generally defined as systems consisting of two ferromagnetic layers separated by a normal metal spacer, through which there is an interlayer exchange coupling (IEC) that favors antiferromagnetic alignment between the ferromagnetic layers [4]. A SAF can, in principle, host two fundamental resonance modes: an acoustic mode where the magnetizations of the two ferromagnetic layers precess in phase, and an optical mode where they precess 180 degrees out of phase (see Fig. E.2 for a schematic of both modes and Fig. E.3 for raw data).

Figure E.4 shows acoustic mode linewidths as a function of frequency for FePd SAFs with Ir spacer thicknesses of 0.5 nm (higher IEC) and 1.3 nm (lower IEC). The Gilbert damping of the SAF with the 0.5 nm Ir spacer is 0.008, while the Gilbert damping of the SAF with the 1.3 nm Ir spacer is 0.02. The value of 0.008 obtained for the SAF with the thinner spacer is quite comparable to literature values for thin films of $L1_0$-ordered FePd [132]. It is not clear what causes the damping to be higher in the SAF with the

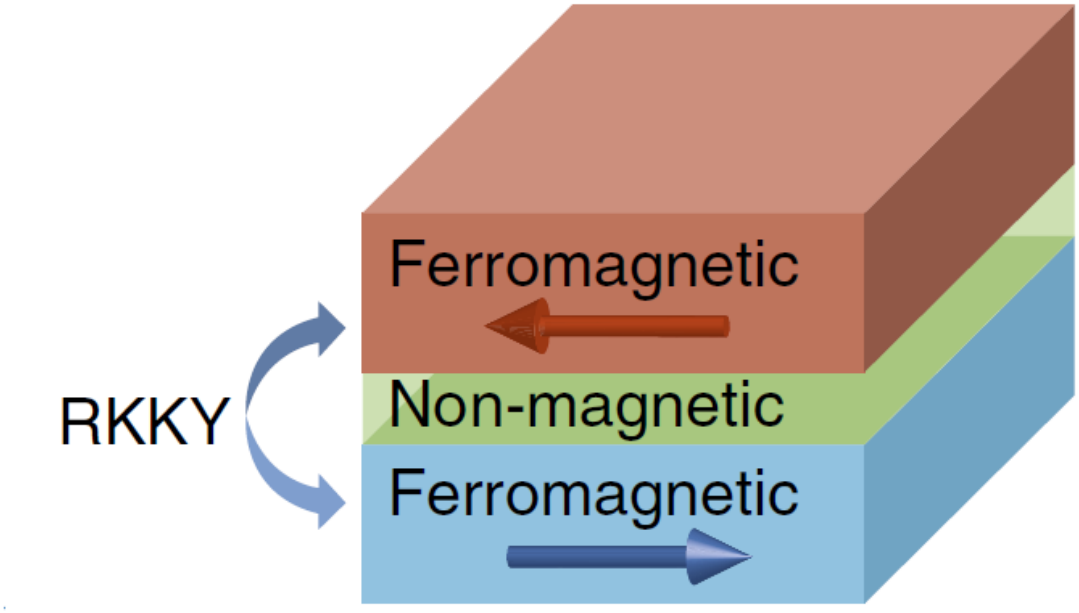

Figure E.1: The general configuration for a SAF. There is RKKY exchange coupling between the ferromagnetic layers mediated by the nonmagnetic spacer. Typically the ferromagnetic layers are chosen to have similar moments so that the total moment is approximately zero when the layers have antiparallel magnetizations. From Ref. [4].

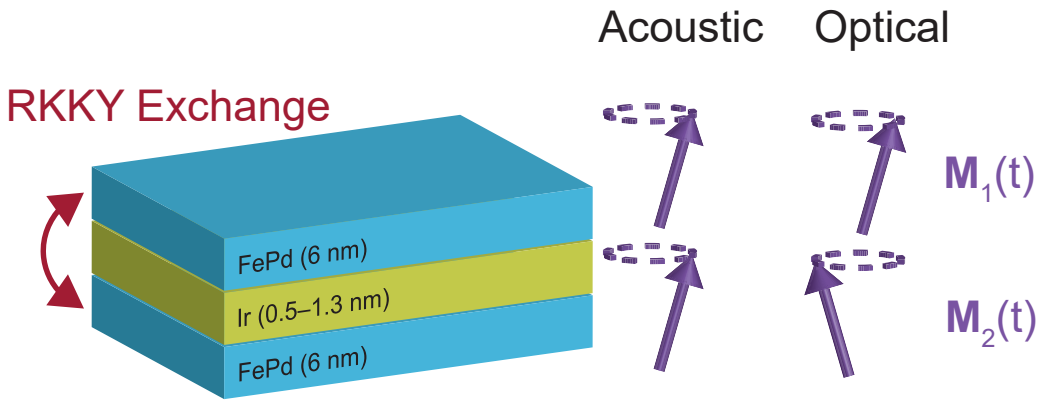

Figure E.2: The configuration for the FePd SAFs studied in this appendix. The applied field in this case is sufficiently strong to overcome the IEC and attain parallel alignment between the layers. The magnetizations of the two layers $\mathbf{M}_1(t)$ and $\mathbf{M}_2(t)$ can precess in phase (acoustic mode) or 180 degrees out of phase (optical mode).

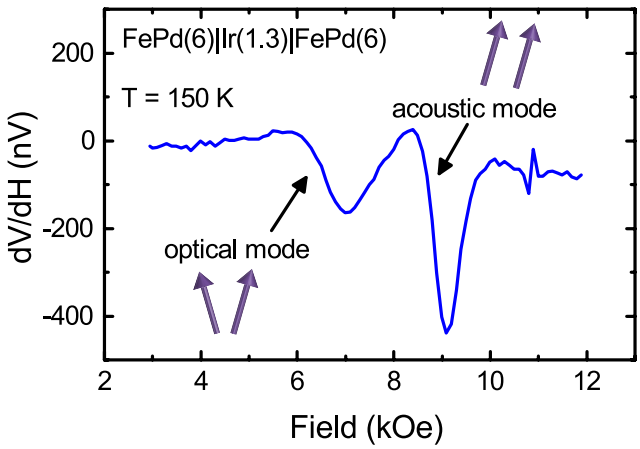

Figure E.3: Resonance spectrum with of the FePd SAF with acoustic and optical modes indicated. The applied field is perpendicular to the plane of the SAF and the sample temperature is 150 K.

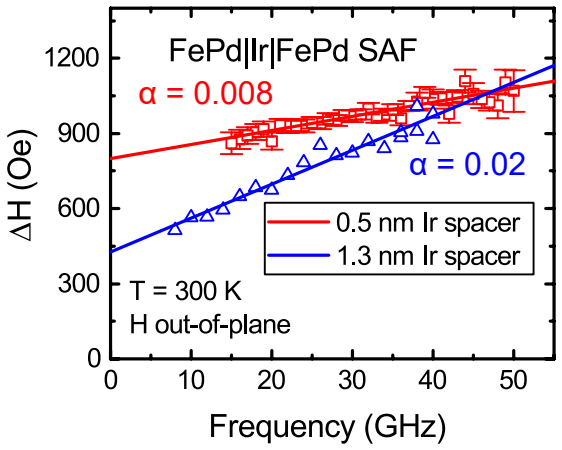

Figure E.4: Acoustic mode linewidths ΔH as a function of frequency for the SAFs having 0.5 nm (red points) and 1.3 nm (blue points) Ir spacers. The measurements are taken for applied field perpendicular to the plane of the SAF with a sample temperature of 300 K.

thicker spacer. One possible cause is that the thicker spacer leads to enhanced spin pumping, but proving this would require a more comprehensive study of the Gilbert damping as a function of spacer thickness.